Title
Advanced Modeling of the Performance of Structures Supported on Triple Friction Pendulum Bearings

Author
Becker, Tracy Celeste

Publication Date
2011

Peer reviewed|Thesis/dissertation

Advanced Modeling of the Performance of Structures Supported on Triple Friction Pendulum Bearings

By

Tracy Celeste Becker

A dissertation submitted in partial satisfaction of the

requirements for the degree of

Doctor of Philosophy

in

Engineering – Civil and Environmental Engineering

in the

Graduate Division

of the

University of California, Berkeley

Committee in charge:

Professor Stephen A. Mahin, Chair
Professor Bozidar Stojadinovic
Professor David Brillinger

Fall 2011

Advanced Modeling of the Performance of Structures Supported on Triple Friction Pendulum Bearings

Abstract

Advanced Modeling of the Performance of Structures Supported on
Triple Friction Pendulum Bearings

by

Tracy Celeste Becker

Doctor of Philosophy in Engineering - Civil and Environmental Engineering

University of California, Berkeley

Professor Stephen A. Mahin, Chair

Seismic isolators, and more specifically, triple friction pendulum (TFP) bearings are ideal earthquake protection technologies for use in performance-based design because they can be designed to achieve multiple performance objectives corresponding to different levels of ground shaking. TFP bearings can limit structure displacement during a design basis (or maximum considered) earthquake while the still effectively isolating the structure under the service level earthquake, reducing seismic demands on the structure and its non-structural components. Furthermore, TFP bearings allow for a gradual transfer of force to the superstructure at ultimate displacement.

This dissertation presents an advanced bidirectional model for the TFP bearing that is based on the kinematic and compatibility relationships of the components of the bearing. To validate the model, experimental characterization tests were conducted on the shake table at the University of California, Berkeley. Two distinct types of experiments were conducted: (a) displacement-controlled tests in which the bearings were cycled through specified orbits and (b) unrestrained tests in which the table replicated ground motions recorded during earthquakes. The bidirectional displacement-controlled tests, which are the first of their kind, generated new knowledge to aid in the development and validation of TFP numerical models. The experimental results provided valuable insight into TFP bearing response and showed that the developed bidirectional model accurately captured the observed behavior of the TFP bearing. The advanced model, which includes translational and rotational degrees of freedom in both horizontal directions, tracks all component displacements as well as the change in bearing height during lateral displacements. The model is general so that no *a priori* conditions regarding bearing properties are required for the validity of the model. These properties make the advanced TFP model a valuable tool to explore the use TFP technology in novel applications.

To further the use of seismic isolation in more standard applications, simplified methods are needed for design. This dissertation investigates the use of generalized modal response spectrum methods to approximate global responses of isolated buildings without the need for costly non-linear numerical simulations. The advanced nonlinear TFP model is used for evaluation of the simplified methods.

Advanced isolation models are important and necessary for understanding the complex nonlinear dynamic behavior exhibited by seismically isolated structures, and to have confidence that performance goals are achieved under a wide variety of seismic hazards. Such models can, as shown in this dissertation, also be used to assess and improve simplified analysis methods suitable for use in routine design.

Table of Contents

List of Figures

List of Tables

Acknowledgements

I am deeply indebted to my advisor Professor Stephen Mahin for his amazing guidance and, sometimes, exceptional patience throughout my studies and research at Berkeley. I truly appreciate both the knowledge and advice he has passed on to me. I would also like to thank Professors Bozidar Stojadinovic and David Brillinger for their contribution as members of my dissertation committee as well as Professors James Kelly and Masayoshi Tomizuka as members of my qualifying exam committee. These professors have greatly expanded my world of knowledge. I would also like to thank Professor Masayoshi Nakashima for his guidance during my stay in his research lab at Kyoto University.

I appreciate the lab staff at the Pacific Earthquake Engineering Research (PEER) labs for their assistance with my experiments and especially for teaching me how to use the crane; Earthquake Protection Systems for providing the bearings used in the experiments; and fellow student Vladimir for being much bigger and stronger than me, which comes in handy in the lab. I am grateful to Chuck and Christina in the PEER library for always magically finding what I was looking for. Also, many thanks to Jyothi for helping me get through the prelims and being an amazing friend.

I am so thankful for the people I've met working at the Richmond Field Station especially Dimitri, Andreas, Mike and Frank who have in turn been teachers and councilors but most of all friends – and partners in bbq. Also thanks to the rest of my field station family including Vesna, Andrea, Ken, Eric, Catherine, Troy, Jiun-Wei, Matt, Gerard, Hong and Chui-Hsin who made the field station feel like a second home.

And, of course, I would like to thank my family who has never wavered in their support of me.

This work was supported by the National Science Foundation under Grant No. CMMI-0724208. Any opinions, findings, and conclusions expressed here are those of the author and do not necessarily reflect the views of the National Science Foundation.

1 Introduction

Seismic isolation has the ability to improve the seismic performance of structures by protecting both structural and non-structural elements, effectively delivering safe buildings that also minimize economic losses due to downtime and repair costs. Although seismic isolation is a mature technology, first implemented in 1969, its proliferation has been limited in the United States, due to a number of reasons including complicated design codes and trepidation on the part of designers and design reviewers. There are a wide variety of bearings available for seismic isolation. Bearings fall into two main categories: elastomeric (rubber) bearings and frictional sliding bearings. Rubber bearing isolation systems are well researched and prolific worldwide. Books such as Naeim and Kelly (1999) and Kelly and Konstantinidis (2011) evidence a large body of research on rubber bearing systems. Among rubber bearings there are linear elastic bearings often used with external energy dissipation devices, lead core rubber bearings, crystallizing rubber bearings and high damping rubber bearings. To maintain stability under large lateral displacements, bearing diameters become large. Increase in bearing diameter results in stiffer bearings, making isolation of light structures difficult. Contrastingly, the behavior of frictional sliding bearings is nominally independent of axial loads.

There are two commonly used types of sliding bearings: flat sliding bearings, which are used in combination with elastomeric systems, and pendulum bearings. The single friction pendulum (SFP) bearing, shown in Figure 1.1, was first proposed by Zayas et al. (1987). The bearing consists of a frictional slider supported on a spherical concave surface. The term pendulum refers to the motion on the slider on the bearing under excitation. This bearing has a bilinear backbone curve that results form the linear stiffness associated with the pendulum motion and the constant frictional force. The hysteretic characteristics of the SFP bearing are similar to a lead plug rubber (LPR) bearing, or linear rubber bearing in combination with an external hysteretic devise, but the initial stiffness of the friction pendulum is often larger and the transition between initial and second stiffness is typically more sudden in the SFP bearing. A more detailed description of the friction pendulum bearing behavior will follow later.

In an effort to create a more adaptable bearing with smoother transitions, Earthquake Protective Systems developed the triple friction pendulum (TFP) bearing, shown in Figure 1.2. The bearing has four stacked spherical sliding surfaces, two of which are identical, leaving three distinct pendulum mechanisms. As motion occurs on all four sliding surfaces, the TFP bearing allows for the same displacement capacity with a bearing that is less than half as large in diameter as the SFP bearing. Additionally, sudden changes in behavior between sliding and non-sliding stages in the SFP bearing trigger transient dynamic responses at the frequency of the supported structure (Morgan and Mahin, 2010). By creating more measured transitions in stiffness, the TFP bearing reduces these responses. The backbone behavior of the TFP bearing is similar to the crystallizing rubber (CR) bearing with an initially stiff behavior, softening towards the design displacement and hardening at large displacements. Again, the transitions between

stiffness in the TFP are more sudden than in the CR bearing. The behavior of the TFP bearing is dependent on the friction coefficients and geometric properties of the bearing. A detailed description of the TFP bearing will follow later.

In order to limit displacements under maximum considered earthquakes, especially ones representative of near-fault ground motions, the yield strengths in SFP and LPR bearings are often to large. However, a large initial yield capacity limits the effectiveness of the isolation system in a service level earthquake. By selecting appropriate values for the friction coefficients and radii for each of the sliding surfaces for the TFP bearing, or designing an effective rubber compound for the CR, designers can achieve isolation under service level earthquakes, while limiting displacement in design and maximum considered earthquakes. TFP bearings have added advantages of being insensitive to structure weight and having arbitrary displacement limits. Additionally, friction pendulum systems are insensitive to mass eccentricities. For these reasons, Morgan and Mahin (2008a) have discussed the adaptability of TFP bearings for use in performance-based design.

Performance-based design (PBD) is an excellent tool in helping earthquake engineering move further toward the goal of increasing the safety of our society's built environment. A considerable amount of research has been done on PBD methodology including Yang et al. (2006) and Mitrani-Reiser (2007). PBD methodology provides a flexible framework for performance goals to be met over a range of seismic demands. Structures require different performance goals for each earthquake hazard level. This necessitates creating performance groups of both structural and nonstructural components, the damage to which is associated with specific engineering demand parameters. Monetary losses are associated with the damage of the performance groups, giving owners and designers tools for communicating structural design goals. Designs are carried out using appropriate earthquake hazard levels and associated performance acceptance criteria as opposed to using code-specified demands and limits.

The structural system has its own performance group, the damage of which is generally associated with story drifts. To keep a structural immediately occupiable, drifts must be kept below yield displacement. Structural cladding or other architectural features such as windows each comprise their own performance group and are also drift dependent. Damage to drift sensitive nonstructural components can begin before the yield drift of the structure is reached, depending on the type of structural system used. Building contents such as computers or servers, HVAC or sprinkler system or other industrial equipment are examples of performance groups whose damage is dependent on floor acceleration. Losses from earthquakes extends past the value of the damage to the structural systems to the loss of building contents, which can account for up to approximately 80% of total building cost (Mayes, 2002). Often more importantly, economic losses come from businesses downtime. Further indirect losses occur when unaffected businesses rely on a damaged business to supply goods or services, creating a ripple effect (Brookshire et al., 1997). Thus, isolation bearings that reduce floor accelerations and drifts for all level of earthquakes are ideal for PDB.

The effectiveness of PDB methodology and the numerical confidence that can be places in the resulting designs depends on the quality of the numerical simulations used to predict seismic response in future events. As such, a key aspect of PBD is to develop and validate numerical models for key components. In view of the potential benefit of

TFP bearings for isolating a wide variety of structural systems, under various earthquake hazard levels, realistic and robust models of TFP bearings are required.

This dissertation develops and experimentally validates an advanced nonlinear model of the TFP bearing. The advanced model will aid in fully understanding detailed behavior of TFP bearings and the intricate local responses of the surrounding structural elements, reassuring designers, code writers and building stakeholders. In addition, detailed models are necessary for proof of concept for novel implementation of seismic technologies, such as mid-story isolation or the use of isolation layers without rigid diaphragms. These techniques may reduce the initial cost of seismic isolation by removing the need for either a seismic moat or an additional floor diaphragm, further promoting the technology.

Realistic models can also be used to conduct parametric and other analyses that, in turn, are used to develop and validate simplified design and analysis methods. It is not reasonable to expect that detailed nonlinear dynamic analyses based on complex models are required for standard structures under typical ground excitations. Thus, the advanced TFP numerical model developed is used to identify and validate a simplified analysis approach for estimating the drift and acceleration characteristics of seismically isolated buildings supported on bearings exhibiting bilinear or TFP hysteric characteristics.

First, a background on friction pendulum bearing systems will be given.

1.1 Friction Pendulum Bearings

The friction pendulum isolator (Figure 1.1), proposed by Zayas et al. (1987), consists of a frictional slider on a spherical concave surface. The radius of the pendulum motion is equal to the radius of the spherical surface, *R*. As the isolated structure moves under excitation, the slider moves up the concave surface, increasing the potential energy. Thus, the bearing has a restoring force, as the building wants to return to its stable equilibrium point. The frictional coefficient, μ, between the slider and the concave surface controls when motion will occur on the isolator, limiting the displacement in larger earthquakes or preventing displacement under wind or traffic loads. The sliding surface has a restraining rim around the edge to limit the ultimate displacement.

When displaced in one dimension, the equations for equilibrium of the friction pendulum bearing are

$$\begin{aligned} F &= f_N \sin\theta + f_T \cos\theta \\ W &= f_N \cos\theta - f_T \sin\theta \end{aligned} \tag{1.1}$$

where F and W are the shear and axial forces on the bearing, and f_T and f_N are the normal and tangential forces on the slider, shown in Figure 1.1. The tangential force on the slider is directly related to the normal force by

$$f_T = \mu f_N \tag{1.2}$$

which reduces Eq. 1.1 to

$$F = W \frac{\sin\theta + \mu\cos\theta}{\cos\theta - \mu\sin\theta} \tag{1.3}$$

From geometry

$$\sin\theta = \frac{u}{R} \tag{1.4}$$

where u is the horizontal displacement of the slider. In general, the term u/R is less than 0.3, and the coefficient of friction is kept below 0.15; as a result, it can be assumed that $\mu\sin\theta$ is negligible and that $\cos\theta = 1$ and Eq. 1.3 then reduces to

$$F = u\frac{W}{R} + \mu W \tag{1.5}$$

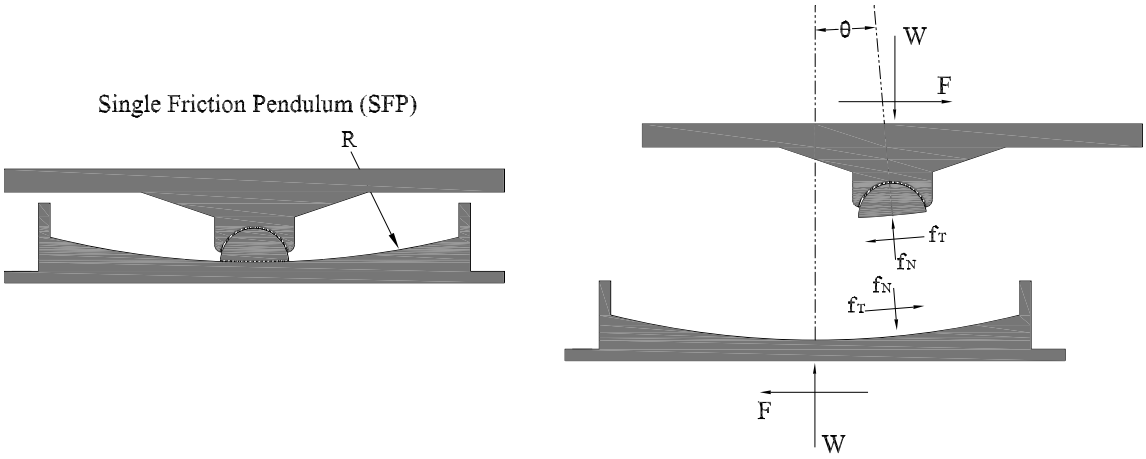

Figure 1.1 Single friction pendulum bearing

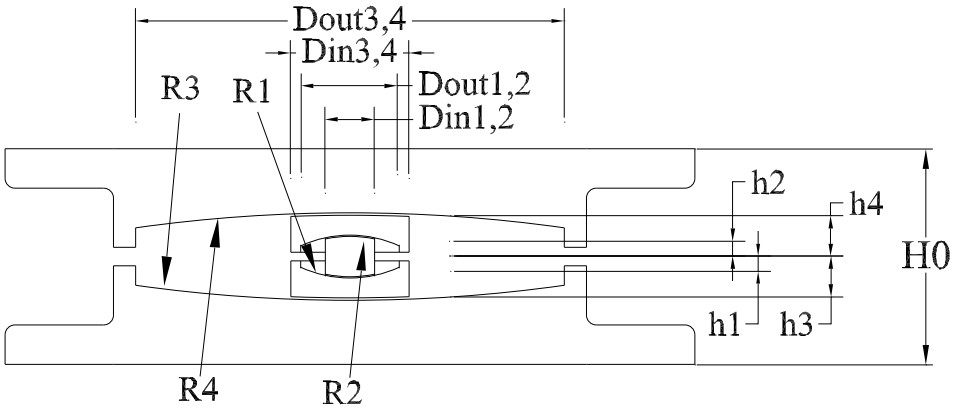

Figure 1.2 Geometry of triple friction pendulum bearings

1.2 Triple Friction Pendulum Bearings

A triple friction pendulum (TFP) bearing consists of a series of stacked sliding surfaces, as shown in Figure 1.2. There are four sliding surfaces with restraining rims to limit displacements. In a typical bearing, the two inner sliding surfaces have the same friction coefficient and radius. The outer surfaces have larger values for these properties and may or may not be distinct from each other. In a typical TFP bearing, as the bearing displacement increases, the surfaces on which sliding occurs change, resulting in incremental softening behavior. As the bearing travels further, the displacement restraints of the sliders are reached and the bearing again changes the surfaces on which it slides. For the typical bearing, this causes incremental hardening behavior until the bearing reaches its ultimate displacement capacity.

1.2.1 Geometry

A cross-sectional diagram of a TFP bearing is shown in Figure 1.2. The bearing is axisymmetric about the vertical axis. The TFP bearing has four sliding surfaces. The sliding surfaces are numbered in the following order from 1 to 4:

1: The bottom surface of the inner sliding component,
2: The top surface of the inner sliding component,
3: The bottom-most surface, and
4: The top-most surface.

The nth surface has its own friction coefficient μ_n, radius R_n and inner and outer diameter, D_{outn} and D_{inn}. The surface has yield force $F_{yn} = \mu_n W$, where W is the normal force on the bearing. The effective pendulum length, L_n, for each surface is taken as the radius subtracted by the distance from the sliding surface to the mid-height of the bearing, h_n, so that

$$L_n = R_n - h_n \tag{1.6}$$

This modification is made so that the displacements due to travel on each sliding surface are measured at the center of the bearing rather than at the sliding surface. This allows the slider displacements to be added directly to determine the displacement of the bearing. From geometry, h_n, for the outer sliding surfaces changes with the displacement of the inner sliders. However, this change is small and can be ignored. The displacement capacity of each sliding surface is circular with a radius of $\left(D_{outn} - D_{inn}\right)/2$. However, because the displacements are measured at the center of the bearing and not at the sliding surface the maximum displacement for each surface, referred to as u_{maxn}, is

$$u_{\max n} = \frac{\left(D_{outn} - D_{inn}\right)}{2}\frac{L_n}{R_n} \tag{1.7}$$

In typical applications, the properties of the two inner sliding surfaces are identical, $L_1 = L_2$, $\mu_1 = \mu_2$. Additionally, the friction coefficient of the inner surfaces μ_1 and μ_2 are normally smaller than the coefficients of the outer sliders. The coefficient of the bottom outer slider μ_3 is less than or equal to the coefficient of the outer top slider μ_4.

The same is true for the effective pendulum lengths. However, these typical restrictions to the bearing properties are not necessary for the functionality of the model developed in the research.

1.2.2 1D behavior

The one-dimensional behavior of the TFP bearing has been previously described by Fenz and Constantinou (2007a) and Morgan and Mahin (2008a). The behavior is derived using an event-based approach in which the equilibrium equations after each event are used to describe the motion. In this approach the outermost components of the TFP bearing are assumed to remain parallel during horizontal motion. Tsai et al. (2010) have extended this approach for an *N*-number slider system. For pressure-independent friction properties and small angle approximations, the result is piecewise linear behavior when the friction coefficient is assumed constant. Transitions in behavior occur when either the friction resistance of a slider is reached or the displacement capacity of a slider is reached, resulting in different sliding stages. For the TFP bearing described above, there are five distinct sliding stages. The equation of motion for each sliding stage is found from the bearing equilibrium equations at that stage using an approach identical to that followed for the single friction pendulum bearing. A detailed discussion is offered in Fenz and Constantinou (2007a) and Morgan and Mahin (2008a) and is summarized below for the convenience of the reader.

Stage 1

Sliding begins when the lowest friction coefficient, that of the inner surfaces, is reached, $F > \mu_1 W$. The bearing then slides on the two inner surfaces. The relationship between displacement u and shear V is

$$F = u\frac{W}{L_1 + L_2} + \frac{\mu_1 L_1 + \mu_2 L_2}{L_1 + L_2} W \tag{1.8}$$

where W is the axial load. Because the inner two sliding surfaces, 1 and 2 are assumed to have identical properties this equation reduces to

$$F = u\frac{W}{2L_1} + \mu_1 W \tag{1.9}$$

Transition to the second sliding stage occurs when the external shear force reaches the friction force on the outer-bottom sliding surface 3. The displacement at which this transition occurs is

$$u^* = 2L_1(\mu_3 - \mu_1) \tag{1.10}$$

Stage 2

Once u^* is reached, motion initiates on sliding surface 3. Due to geometric constraints, motion then halts on the bottom inner sliding surface 2. Thus, in this stage of motion the bearing sliding occurs on the top inner sliding surface 1 and on the bottom outer sliding surface 3. The resulting horizontal force-displacement relation is

$$F = u\frac{W}{L_2 + L_3} + \frac{\mu_2 L_2 + \mu_3 L_3 - (\mu_3 - \mu_1)L_1}{L_2 + L_3}W \tag{1.11}$$

Because $L_3 > L_1$, the slope of the force-displacement curve in Stage 2 is lower than the slope in Stage 1; thus, the bearing exhibits a softening behavior. Transition to the third sliding stage occurs when the coefficient of friction of the top outer slider is reached. The corresponding displacement for this transition is

$$u^{**} = u^{*} + (\mu_4 - \mu_3)(L_2 + L_3) \tag{1.12}$$

Stage 3

Once u^{**} is reached, motion initiates on the top outer surface 4. Due to geometric constraints, motion stops on the top inner sliding surface 2; however, it continues on the bottom outer surface 3. Hence, sliding in this stage occurs on the two outer surfaces. The motion characteristics are below.

$$F = u\frac{W}{L_3 + L_4} + \frac{\mu_3 L_3 + \mu_4 L_4 - (\mu_3 - \mu_1)L_1 - (\mu_4 - \mu_2)L_2}{L_3 + L_4}W \tag{1.13}$$

Again, the tangent stiffness in Stage 3 is lower than the slope in Stage 2, and the behavior is softening further when it reaches this stage. The third sliding stage of the bearing continues until the restrainer of the bottom outer surface 3 is contacted. The total bearing displacement at which the bottom outer slider contacts its restrainer is

$$u^{*3} = u^{**} + u_{\max 3}\left(1 + \frac{L_4}{L_3}\right) - (\mu_4 - \mu_3)(L_3 + L_4) \tag{1.14}$$

Stage 4

Once the bottom outer sliding concave contacts its restrainer, motion continues on the top outer surface 4. Due to the geometric assumptions, motion re-initiates on the bottom inner surface 2. As a result the bearing force increases with a slope of $1/(L_1+L_3)$. If the effective radii of the outer surfaces are equal, then this is the same slope as in Stage 2. Either way, the bearing force-displacement slope in Stage 4 is greater than that in Stage 3 and the bearing exhibits a hardening behavior when it reaches this stage. The fourth sliding stage continues until the top outer slider contacts its restrainer. The total displacement at contact is

$$u^{*4} = u^{*3} + \left[\left(\frac{u_{\max 4}}{L_4} + \mu_4\right) - \left(\frac{u_{\max 3}}{L_3} + \mu_3\right)\right](L_2 + L_4) \tag{1.15}$$

Stage 5

When both outer sliding concaves have contacted their restrainers, motion can continue only on the inner sliding surfaces. Now, the bearing force increases with a slope of $1/(L_1+L_2)$, which is the same as in Stage 1. Again, this slope is greater than in Stage 4, and the bearing has further hardened. The ultimate displacement of the bearing U_{max} occurs when the restrainers of all four sliders are engaged

$$U_{\max} = \sum_{n=1}^{4} u_{\max n} \tag{1.16}$$

The implementation of the 1D piece-wise linear behavior model for a typically designed bearing results in Figure 1.3.

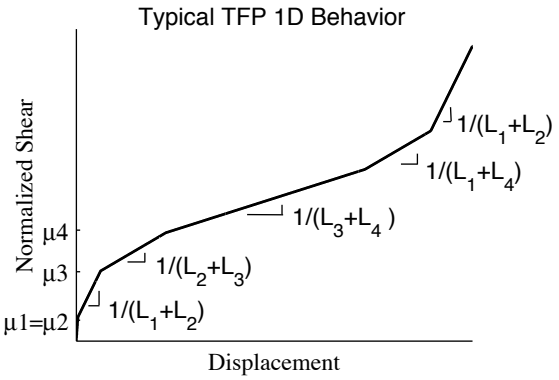

Figure 1.3 1D piecewise behavior of the TFP bearing for the typical condition $\mu_1=\mu_2$ and $L_1=L_2$

The assumption that the top and bottom of the isolator remain parallel means that, at any given time, motion occurs on only two sliding surfaces. The slope of the backbone curve during any stage is the inverse of the sum of the effective pendulum lengths of the two sliders in motion (as shown in Figure 1.3). It is evident that the sliding surface parameters shown in Figure 1.2 directly affect the hysteretic behavior of the isolator.

To ensure this behavior, a few additional conditions on the bearing properties must be made. First, the inner sliders must not contact their respective restraining surfaces before motion begins on the outer sliders. Once motion starts on sliding surface 3, it stops on sliding surface 1; and once sliding starts on surface 4, it stops on surface 2. To ensure that surface 1 does not reach its displacement capacity before Stage 2 begins, the following condition is necessary

$$\mu_3 \le \mu_1 + \frac{u_{\max 1}}{L_1} \tag{1.17}$$

and similarly, to ensure that sliding on surface 2 does not reach its capacity before Stage 3, the following condition must be met

$$\mu_4 \le \mu_2 + \frac{u_{\max 2}}{L_2} \tag{1.18}$$

If

$$\mu_3 > \mu_1 + \frac{u_{\max 1}}{L_1}$$

then there will be a jump in force between Stage 1 and Stage 2, and if

$$\mu_4 > \mu_2 + \frac{u_{\max 2}}{L_2}$$

then there will be a jump in force between Stage 2 and Stage 3. If

$$\mu_3 = \mu_1 + \frac{u_{\max 1}}{L_1} \text{ or } \mu_4 = \mu_2 + \frac{u_{\max 2}}{L_2}$$

then the respective inner sliding surface will have reached its displacement capacity when Stage 2 (or Stage 3) initiates and there will be no travel left for Stage 4 and 5 (or just Stage 5), resulting in loss of the incremental hardening behavior provided by Stages 4 and 5. Additionally, to ensure that the two inner sliders reach their maximum displacements at the same time, L and u_{max} of the outer sliders must be the same. If the outer sliding surfaces also share the same friction coefficient, then motion initiates on them at the same time and Stages 2 and 4 are suppressed. A limitation of even-based models is that the required constraints on the combinations of mechanical and geometric properties of the individual sliding surfaces must all be met. Although these constraints are generally valid in current TFP bearing designs, a numerical model that does not depend *a priori* on satisfying these constraints is desirable.

1.2.3 Numerical models

Implementing the piecewise linear behavior exhibited by TFP bearings requires numerous rules for loading and unloading, which makes modeling with this approach cumbersome. To implement the 1D piecewise behavior model for analysis, a method utilizing a series of gap-hook and spring elements was developed independently by Fenz and Constantinou (2008a) and Morgan (2008b). This allows the bearing to be modeled using existing elements in commercial software. Although the series-spring bidirectional model does not exhibit true circular slider-restraining surfaces due to the lack of circular gap-hook elements in the commercial structural analysis software, Fenz and Constantinou (2008b) show that the bidirectional series-spring model compares well to experimental tests, making it a useful numerical model for typically designed TFP bearings.

A drawback to modeling with the series-spring method is that the model does not explicitly track displacements of individual bearing components or component-restrainer interactions. The properties of frictional surfaces are affected by velocity, temperature and pressure as described by Constantinou et al. (1999) and Konstantinidis et al. (2008). The series-spring model cannot directly track instantaneous velocities to model velocity effects on the frictional coefficients of the four sliding surfaces.

In order to simulate an arbitrary pattern of bidirectional motion without constraints on the friction coefficient and radius of each sliding surface, this dissertation presents a kinematic model based on the constitutive and compatibility relationships of individual sliding surfaces of the bearing. Due to the nonlinearity of the bearing behavior, the governing relationships are updated at each displacement increment. Coupled plasticity with circular yield surfaces as well as circular restraining surfaces are used to realistically simulate the bearing motion. Unlike all previous models, no limitations on bearing geometry are imposed. Since the model tracks motion on each sliding surface, it is possible to extend its capabilities to account for and investigate the effects of rate,

temperature and pressure. No analytical model, prior to the one presented herein, exists that directly tracks individual slider displacements or slider-restrainer interactions with bidirectional motion.

1.3 Outline of this Dissertation

The advanced bidirectional model for the triple friction pendulum bearing based on the kinematic and compatibility relationships of the five components of the bearing is described in Chapter 2. To validate the model, experimental characterizations tests were conducted using the shake table at the University of California, Berkeley. Two distinct types of experiments were conducted: (a) displacement-controlled tests in which the bearings were cycled through specified orbits, and (b) unrestrained tests in which the dynamic behavior of the bearing under simulated earthquake loading was observed. The bidirectional tests with the controlled-displacement tests, which are the first of their kind, generated new knowledge to aid in the development and validation of TFP bearing models. Chapter 3 presents comparisons between the bidirectional model and the controlled-displacement tests as well as observations from the controlled-displacement test. Chapter 4 presents the similar comparisons for the unrestrained tests.

The behavior of the TFP bearing in Chapter 2 assumes that the outermost components of the bearing remain parallel, as does the 1D model derived from equilibrium equations discussed above in Section 1.2.2. Chapter 5 investigates the effect of relaxing this constraint, thereby allowing rotation of the outermost components. The advanced kinematic bidirectional model is modified to accommodate rotation about two horizontal axes. Special note is made of how placement of a TFP bearing on top of a flexible column can affect the bearing behavior.

By using realistic hysteretic models of isolation bearings, it is possible to evaluate and improve simplified methods of analysis that can be used in design of seismically isolated buildings. As noted previously, PBD typically focuses on engineering design parameters related to story drift and floor level accelerations. Thus, Chapter 6 examines the ability of several modal response spectrum methods to estimate global behavior of isolated structures. In this case, attention is placed on the ability of modal analysis methods to estimate roof and isolator displacement, story drifts and shears, and floor level pseudo-acceleration spectra. The advanced TFP model is used to simulate the nonlinear dynamic response of three different height structures. A generalized modal analysis model was demonstrated to provide quite realistic estimates of responses predicted using nonlinear time history analyses. While this generalized modal analysis model differs from methods commonly used in practice, its accuracy and simplicity provides a convenient way for designers to examine and optimize the local and global behavior of conventional isolated structures without having to carry out complex nonlinear dynamic analyses.

2 Bidirectional Kinematic TFP Bearing Model

The kinematic bearing model proposed in this chapter describes the bidirectional translational shear behavior of the TFP bearing shown in Figure 1.2. The bearing's top and bottom surfaces are permitted to translate along the global *X, Y,* and *Z* axes, but they are assumed to remain parallel, the same assumption made in the 1D behavior model described in Section 1.2. Thus, rotation of the outermost concave components about the global *X* and *Y* horizontal axes is not permitted in the model. The addition of rotation will be addressed in Chapter 5. In addition, global and local torsion resistance about the vertical axis, discussed later in more detail, is disregarded. The force resultants of any friction or bearing stresses acting on a sliding surface are idealized as concentrated forces acting at the center of that sliding surface. The internal slider and concave slider components are allowed to translate and rotate arbitrarily in order to maintain equilibrium and compatibility considering the applied axial load, individual component behaviors and the geometric relationships of the bearing components.

The model presented here does not assume any *a priori* sequence of events. Transitions between sliding modes occur when either the friction resistance or the displacement capacity of a slider is reached. As the model does not place any conditions on sequence of events, the input properties of the bearing can be manipulated to model single friction pendulum bearings in addition to the TFP bearing.

The internal components of the bearing are each modeled as being axially rigid. As a result, the bearing is assumed to remain elastic, and the bearing's vertical stiffness term is set to an arbitrary large value. The vertical deformation of the bearing is calculated from the displacements of the bearing sliders based on their geometry and is computed at the end of each step. The axial load is assumed to be in compression and remain constant within each time step. The model does not track the behavior of the sliders, and thus the TFP bearing, when uplift occurs.

The behavior of the TFP bearing is path dependent, so the force-deformation relationship must be updated in the model at every displacement increment. At each displacement increment, the tangent stiffness of each sliding surface is calculated, and the transformation matrix from local slider displacements $\mathbf{u}_i$ to the global *X* and *Y* displacements is updated. While other formulations are possible, the model presented herein is developed within the Cartesian coordinate systems for both global and local displacements. The local tangent stiffness and transformation matrices are used to find the global tangent stiffness matrix. The change in force in the global *X* and *Y* directions is found by multiplying the global tangent stiffness vector by the displacement increment.

In this chapter, a detailed description of the geometric compatibility relations used to capture the kinematics of the TFP bearing is provided along with a description of the constitutive relations for each sliding surface, considering elastic, hysteretic and

restrainer resultant forces. These are then used to develop the tangent stiffens matrix for the global model. A simple one-dimensional example is provided to illustrate the capabilities of the model, including the ability to track the displacements of the internal sliding components.

2.1 Geometric Compatibility Relationship

This model assumes an installation situation where essentially rigid floor slabs or other structural elements are provided both above and below the isolation level to resist bending and rotational deformations. For such a situation, the assumption that global rotational of the bearing about the *X* and *Y* axes is zero is appropriate. As noted above, the rotation of the bearing about the global *Z* axis is unrestrained and disregarded in this formulation.

The remaining global degrees of freedom are translation of each outer concave component in the *X* and *Y* direction (U_{iX} U_{jX} U_{iY} U_{jY}). From geometry and the assumption the rotations are constrained about the global *X* and *Y* axes, the relative displacement between the top node of the bearing, *j*, and the bottom node the bearing, *i*, in the *X* and *Y* directions of the bearing are equal to the summation of the local transverse displacements on each slider *n*.

$$\begin{aligned} U_{jX} - U_{iX} &= \sum_{n=1}^{4} u_{nX} \\ U_{jY} - U_{iY} &= \sum_{n=1}^{4} u_{nY} \end{aligned} \tag{2.1}$$

The local slider rotations θ, shown in Figure 2.1, are defined as the angle made from the axes of symmetry that extend from two bearing components that share the same sliding interfaces. Thus, θ_1 refers to the relative rotation between the axes of symmetry of the lower concave slider and the central slider, θ_2 refers to the relative rotation between the axes of symmetry of the upper concave slider and the central slider, θ_3 refers to the relative rotation between the axes of symmetry of the lowermost concave and the lower concave slider, and θ_4 refers to the relative rotation between the axes of symmetry of the uppermost concave and the upper concave slider. With these definitions and sign conventions and the from the constraint that the global rotations of the outermost components are zero, the sum of the relative rotations in the upper portion of the bearing must equal the sum of the relative rotations in the lower portion of the bearing in both the *X* and *Y* directions.

$$\begin{aligned} \theta_{1X} - \theta_{2X} + \theta_{3X} - \theta_{4X} &= 0 \\ \theta_{1Y} - \theta_{2Y} + \theta_{3Y} - \theta_{4Y} &= 0 \end{aligned} \tag{2.2}$$

The local rotation is directly related to the local displacement by the effective pendulum length *L* of each sliding surface.

$$u_n = L_n \sin\theta_n \tag{2.3}$$

The small angle approximation reduces this to

$$u_n = L_n \theta_n \tag{2.4}$$

The use of a Cartesian coordinate system complicates the computation of L_n due to change in displacement in the perpendicular direction. At each step *t*, the effective pendulum length of the sliding surface in both the *X* and *Y* direction must be recalculated using the following equations

$$\begin{aligned} L_{nXt} &= \sqrt{L_{n0}^2 - u_{nYt}^2} \\ L_{nYt} &= \sqrt{L_{n0}^2 - u_{nXt}^2} \end{aligned} \tag{2.5}$$

where u_X and u_Y are the local slider displacements in the *X* and *Y* directions.

The local displacement vector **u** is defined as $[u_{1X}\ u_{2X}\ u_{3X}\ u_{4X}\ u_{1Y}\ u_{2Y}\ u_{3Y}\ u_{4Y}]^T$ and the local slider rotation vector **θ** is defined as $\boldsymbol{\theta} = [\theta_{1X}\ \theta_{2X}\ \theta_{3X}\ \theta_{4X}\ \theta_{1Y}\ \theta_{2Y}\ \theta_{3Y}\ \theta_{4Y}]^T$. From Eq 2.4, the relationship, $\mathbf{T_{local}}$, between the local slider rotations and the local slider displacements becomes

$$\mathbf{u} = \begin{bmatrix} L_{1X} & 0 & 0 & 0 & 0 & 0 & 0 & 0 \\ 0 & L_{2X} & 0 & 0 & 0 & 0 & 0 & 0 \\ 0 & 0 & L_{3X} & 0 & 0 & 0 & 0 & 0 \\ 0 & 0 & 0 & L_{4X} & 0 & 0 & 0 & 0 \\ 0 & 0 & 0 & 0 & L_{1Y} & 0 & 0 & 0 \\ 0 & 0 & 0 & 0 & 0 & L_{2Y} & 0 & 0 \\ 0 & 0 & 0 & 0 & 0 & 0 & L_{3Y} & 0 \\ 0 & 0 & 0 & 0 & 0 & 0 & 0 & L_{4Y} \end{bmatrix} \boldsymbol{\theta} = \mathbf{T_{local}}\boldsymbol{\theta} \tag{2.6}$$

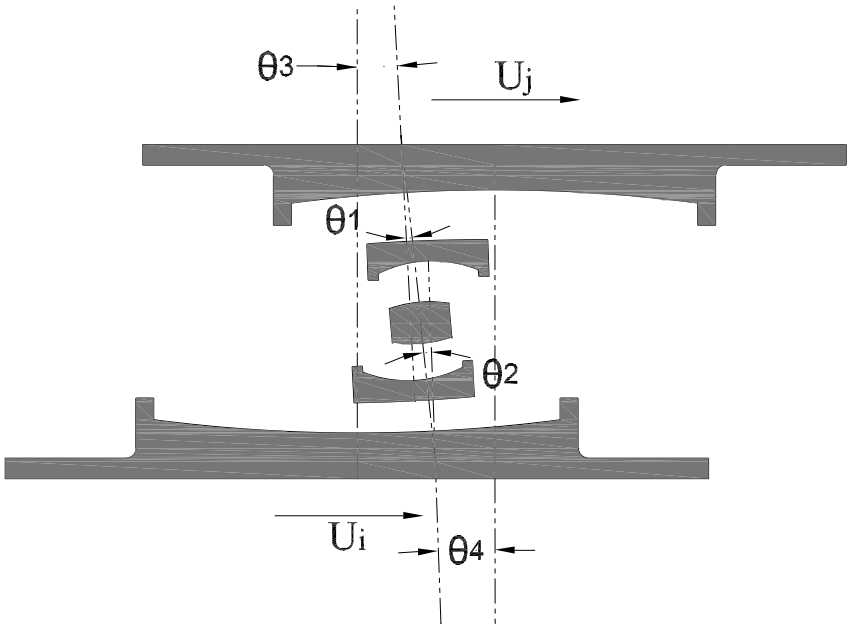

Figure 2.1 Local slider rotations (1D exploded view)

For each direction of motion (*X* or *Y*), there are four independent global degrees of freedom in the system. These include the displacements of the top and bottom nodes of the bearings and two other degrees of freedom chosen to simplify subsequent calculations. For this model those degrees of freedom were chosen as θ_1 and θ_2. Thus, the global displacement matrix $\boldsymbol{U}$ is 8x1 with **U** defined as $[U_{iX}\ U_{jX}\ U_{iY}\ U_{jY}\ \theta_{1X}\ \theta_{2X}\ \theta_{1Y}\ \theta_{2Y}]^T$. Equations 2.1 and 2.2 are then used to develop a transformation matrix **T** between the global displacements **U** and local slider rotations **θ**.

$$\mathbf{T} = \begin{bmatrix} 0 & 0 & 0 & 0 & 1 & 0 & 0 & 0 \\ 0 & 0 & 0 & 0 & 0 & 1 & 0 & 0 \\ -\frac{1}{L_{3X}+L_{4X}} & \frac{1}{L_{3X}+L_{4X}} & 0 & 0 & -\frac{L_{1X}+L_{4X}}{L_{3X}+L_{4X}} & \frac{-L_{2X}+L_{4X}}{L_{3X}+L_{4X}} & 0 & 0 \\ -\frac{1}{L_{3X}+L_{4X}} & \frac{1}{L_{3X}+L_{4X}} & 0 & 0 & \frac{-L_{1X}+L_{3X}}{L_{3X}+L_{4X}} & -\frac{L_{2X}+L_{3X}}{L_{3X}+L_{4X}} & 0 & 0 \\ 0 & 0 & 0 & 0 & 0 & 0 & 1 & 0 \\ 0 & 0 & 0 & 0 & 0 & 0 & 0 & 1 \\ 0 & 0 & -\frac{1}{L_{3Y}+L_{4Y}} & \frac{1}{L_{3Y}+L_{4Y}} & 0 & 0 & -\frac{L_{1Y}+L_{4Y}}{L_{3Y}+L_{4Y}} & \frac{-L_{2Y}+L_{4Y}}{L_{3Y}+L_{4Y}} \\ 0 & 0 & -\frac{1}{L_{3Y}+L_{4Y}} & \frac{1}{L_{3Y}+L_{4Y}} & 0 & 0 & \frac{-L_{1X}+L_{3Y}}{L_{3Y}+L_{4Y}} & -\frac{L_{2Y}+L_{3Y}}{L_{3Y}+L_{4Y}} \end{bmatrix} \tag{2.7}$$

The relationship between the global and local displacements then becomes $\mathbf{u} = \mathbf{T}_{\mathbf{local}}\mathbf{T}\mathbf{U}$.

2.2 Sliding Surface Constitutive Relationship

Each of the four sliding surfaces of the TFP bearing has the generic backbone behavior shown in Figure 2.2 for 1D behavior. Motion on a sliding surface is initiated when the slider's yield force is reached. Theoretically, motion on a friction surface initiates at an infinitesimally small displacement. However, in actuality sliding initiates at a finite displacement. Scheller and Constantinou (1999) suggest a yield displacement u_y at the onset of sliding of 0.01 in. This value may vary depending on the type and thickness of the composite liner used. Thus, a large but finite initial stiffness is expected, denoted herein as k_0. After sliding commences, the stiffness is inversely proportional to the surface's effective pendulum length, *L*. Sliding continues until the slider reaches its displacement limit u_{max}. Once the slider contacts the restrainer, the stiffness of the sliding surface is often assumed to be infinite. For the model developed in this chapter, this stiffness is arbitrarily given the same numerical value, k_0, as the initial stiffness. The restrainer is assumed to be infinitely strong.

To compute the forces acting on the sliding surfaces, each sliding surface is modeled as a parallel system consisting of a linear elastic element, a rate-independent bidirectional hysteretic element and a gap-spring element. These model the elastic, hysteretic and restrainer contact components of the behavior respectively.

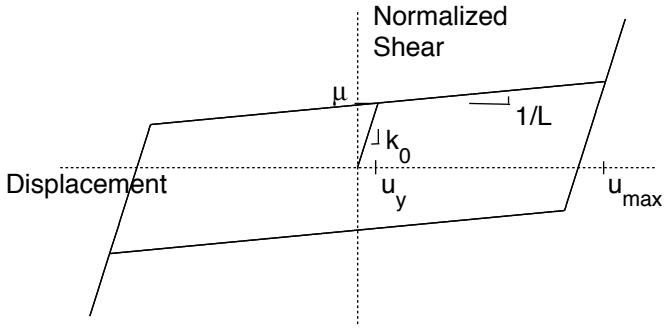

Figure 2.2 Individual slider 1D behavior

2.2.1 Elastic restoring force

The elastic stiffness of an individual sliding surface is due to the radius of the surface and is proportional to the axial load *W* on the surface. The elastic restoring forces are equal to the inverse of the radii, corrected for the change in radius due to the perpendicular displacement, which is described in Eq 2.5.

$$\mathbf{k}_{elastic} = \begin{bmatrix} \dfrac{W}{L_X} & 0 \\ 0 & \dfrac{W}{L_Y} \end{bmatrix} \tag{2.8}$$

2.2.2 Hysteretic friction force

Mosqueda et al. (2004a) described the use of bidirectional plasticity to model the hysteretic behavior of the single friction pendulum bearing. For the TFP bearing, the same method is implemented independently for each sliding surface. A brief review of the plasticity model is given here for an individual sliding surface.

The elastic force-displacement relationship for the sliding surface is given by

$$\mathbf{F} = \left(k_0 - \frac{W}{L} \right)(\mathbf{u} - \mathbf{u}^p) \tag{2.9}$$

Where $\mathbf{u}^p$ is the plastic displacement and **F** is the force on the sliding surface. The frictional behavior of the sliders results in a circular yield condition. When within the restrainer limit, the normalized yield condition *Y* is given as

$$Y(\mathbf{F}) = \|\mathbf{F}\| - W\mu \le 0 \tag{2.10}$$

When the yield surface $Y = 0$ is reached, plastic flow occurs with slip rate $\gamma > 0$. When $Y < 0$ there can be no change in the plastic displacement; thus, the slip rate becomes $\gamma = 0$ and $\dot{\mathbf{u}}^p = 0$. This results in the flow rule

$$\dot{\mathbf{u}}^p = \gamma \text{sign}(\mathbf{F}) \tag{2.11}$$

Loading and unloading are described by the Kuhn-Tucker complimentary conditions

$$\gamma \geq 0\,,\; Y(\mathbf{F}) \geq 0\,,\; \gamma Y(\mathbf{F}) \geq 0 \tag{2.12}$$

and the consistency condition

$$\gamma \dot{Y}(\mathbf{F})=0 \;\; (\text{if } Y(\mathbf{F}) = 0\,) \tag{2.13}$$

Equations 2.9 through 2.13 describe the conditions for the bidirectional plasticity model. They are implemented equating yielding with sliding on the considered surface, using a return-mapping algorithm described in Simo and Hughes (2000). In this way, the hysteretic behavior of each sliding surface is described by a 2x2 tangent stiffness matrix.

2.2.3 Restrainer force

The model presented in Mosqueda et al. (2004) for the single friction pendulum bearing does not consider the effect of slider contact with a restraining surface. Inclusion of this effect is necessary for the TFP bearing to fully account for the interaction between the four sliding surfaces. In the ideal formulation considered here, the friction between the slider and the restrainer in the tangential direction of motion (and the possible resulting rotation of the slider with respect to the Z axis) is disregarded. This type of behavior of the restrainer is best described in polar coordinates, where the stiffness in the radial direction $k_{rr}=k_0$, while the stiffness in the tangential direction $k_{\theta\theta}= k_{r\theta}= k_{\theta r}=0$. In expressing the stiffness matrix in Cartesian coordinates, the contact force, $\mathbf{F}_{cont}$, must always be in the radial direction. The relationship between the Cartesian contact forces, F_{Xcont} and F_{Ycont}, and the radial contact force, F_{Rcont}, is

$$\mathbf{F}_{cont} = \begin{bmatrix} F_{Xcont} \\ F_{Ycont} \end{bmatrix} = \begin{bmatrix} \dfrac{u_X}{\sqrt{u_X{}^2 + u_Y{}^2}} \\ \dfrac{u_Y}{\sqrt{u_X{}^2 + u_Y{}^2}} \end{bmatrix} F_{Rcont} = \begin{bmatrix} \dfrac{u_X}{\sqrt{u_X{}^2 + u_Y{}^2}} \\ \dfrac{u_Y}{\sqrt{u_X{}^2 + u_Y{}^2}} \end{bmatrix} \left\| \mathbf{F}_{cont} \right\| \tag{2.14}$$

A rotation matrix, $\mathbf{k}_{rotation}$, is used to transform the contact forces to the radial direction at each step. It is formed by finite difference on Eq. 2.14. The complete restrainer contact stiffness matrix is then

$$\mathbf{k}_{contact} = k_0 \begin{bmatrix} \dfrac{u_X{}^2}{u_X{}^2 + u_Y{}^2} & \dfrac{u_X u_Y}{u_X{}^2 + u_Y{}^2} \\ \dfrac{u_X u_Y}{u_X{}^2 + u_Y{}^2} & \dfrac{u_Y{}^2}{u_X{}^2 + u_Y{}^2} \end{bmatrix} \mathbf{k}_{rotation} \tag{2.15}$$

Of course, when the slider has not contacted the restraining surface, $\mathbf{k}_{contact}$ is a zero matrix. Representing the restraining surface in this way is a simplification of a complex behavior. It does not take into account any yielding or energy dissipation due to impact when the bearing's ultimate displacement is reached or due to frictional forces when the slider moves along the restraining surface.

The stiffness for each sliding surface is obtained by adding the elastic, hysteretic and contact stiffness matrices. The 8x8 local stiffness matrix, $\mathbf{k}_S$, for the TFP bearing is then assembled from these 2x2 matrices.

2.2.4 Correction for surface rotations

When a sliding surface is rotated about a horizontal axes, the static equilibrium point for the slider is shifted from the center of the slider. The effect of rotation on a single friction pendulum bearing behavior from either installation error or a flexible column is discussed by Mosqueda et. al (2004b). Similar conditions occur on the contact surfaces of the inner slider with the two concave sliders during the translation of the TFP bearing, even if the outermost components do not rotate about the global *X* and *Y* axes. This requires the addition of a geometric correction to the tangent stiffness previously derived.

For a single friction pendulum bearing, the equations of static equilibrium, for the unrotated bearing (previously described in Chapter 1) are

$$\begin{aligned} F &= f_N \sin\theta + f_T \cos\theta \\ W &= f_N \cos\theta - f_T \sin\theta \end{aligned} \tag{2.16}$$

Which reduces for small angles to the force-displacement relationship

$$F = \frac{W}{R}u + \mu W \tag{2.17}$$

Considering the single friction pendulum isolator configuration in Figure 2.3, when the concave sliding surface is rotated counterclockwise by an angle α the equations of static equilibrium become

$$\begin{aligned} F &= f_N \sin(\theta+\alpha) + f_T \cos(\theta+\alpha) \\ W &= f_N \cos(\theta+\alpha) - f_T \sin(\theta+\alpha) \end{aligned} \tag{2.18}$$

Using the same small angle approximations from Chapter 1, the force-displacement relationship becomes

$$F = W\left(\frac{1}{R}u + \alpha\right) + \mu W \tag{2.19}$$

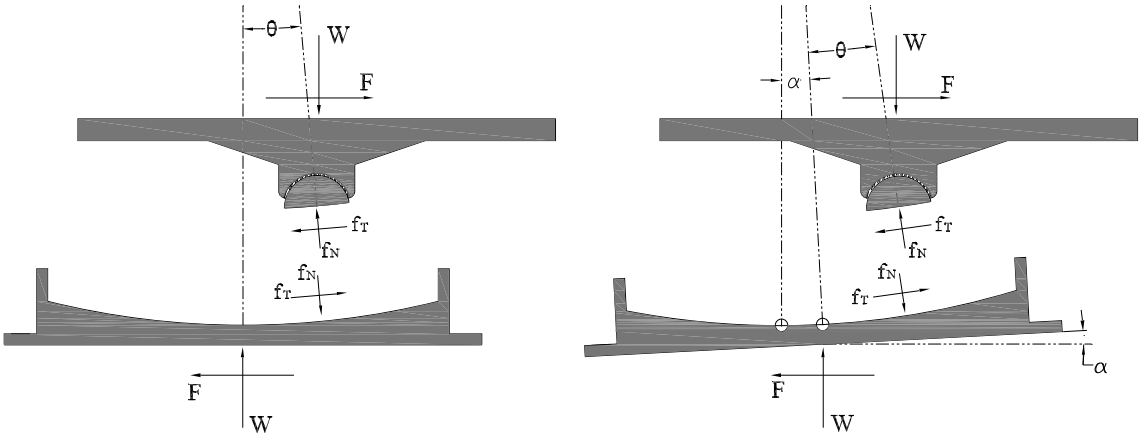

Figure 2.3 Single friction pendulum bearing with unrotated and rotated bottom surfaces (exploded 1D view)

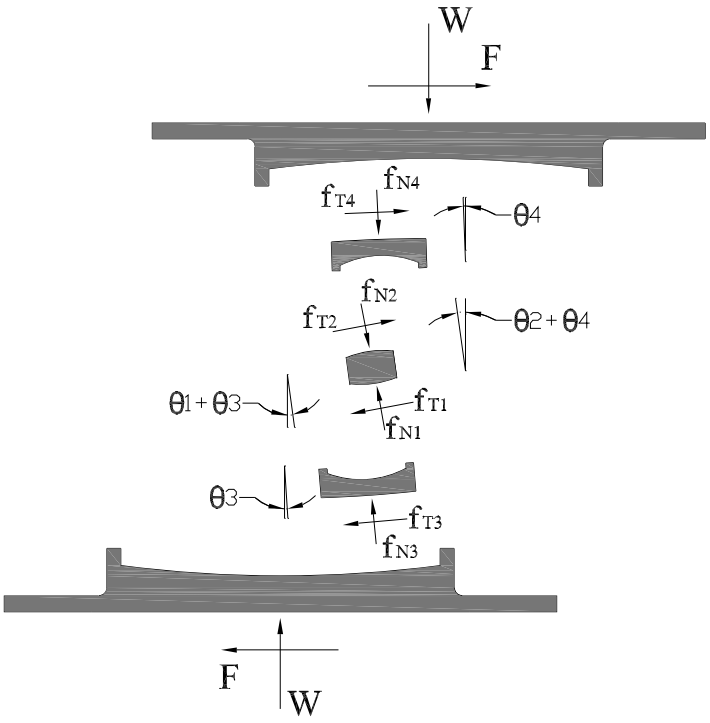

Figure 2.4 Forces in an offset triple friction pendulum bearing (exploded 1D view)

This Eq. 2.19 indicates that a counterclockwise rotation results in a positive shift in the overall force-displacement curve.

The same approach will now be used to assess the effect that rotation (tilting) of the individual sliders during their transverse movement would have on the overall behavior of the bearing. A free body diagram of the TFP bearing with displacement on all four sliders is shown in Figure 2.4. The resulting force-displacement relations are as follows:

Surface 1:

$$\begin{aligned} F &= f_{N1}\sin\left(\theta_1+\theta_3\right)+f_{T1}\cos\left(\theta_1+\theta_3\right) \\ W &= f_{N1}\cos\left(\theta_1+\theta_3\right)-f_{T1}\sin\left(\theta_1+\theta_3\right) \end{aligned} \tag{2.20}$$

$$F = W\left(\frac{1}{L_1}u_1+\theta_3\right)+\mu_1 W = W\left(\frac{1}{L_1}u_1+\frac{1}{L_3}u_3\right)+\mu_1 W \tag{2.21}$$

Surface 2:

$$\begin{aligned} F &= f_{N2}\sin\left(\theta_2+\theta_4\right)+f_{T2}\cos\left(\theta_2+\theta_4\right) \\ W &= f_{N2}\cos\left(\theta_2+\theta_4\right)-f_{T2}\sin\left(\theta_2+\theta_4\right) \end{aligned} \tag{2.22}$$

$$F = W\left(\frac{1}{L_2}u_2 + \theta_4\right) + \mu_2 W = W\left(\frac{1}{L_2}u_2 + \frac{1}{L_4}u_4\right) + \mu_2 W \tag{2.23}$$

Surface 3:

$$\begin{aligned} F &= f_{N3}\sin(\theta_3) + f_{T3}\cos(\theta_3) \\ W &= f_{N3}\cos(\theta_3) - f_{T3}\sin(\theta_3) \end{aligned} \tag{2.24}$$

$$F = \frac{W}{L_3}u_3 + \mu_3 W \tag{2.25}$$

Surface 4:

$$\begin{aligned} F &= f_{N4}\sin(\theta_4) + f_{T4}\cos(\theta_4) \\ W &= f_{N4}\cos(\theta_4) - f_{T4}\sin(\theta_4) \end{aligned} \tag{2.26}$$

$$F = \frac{W}{L_4}u_4 + \mu_4 W \tag{2.27}$$

It is only the inner sliding surfaces, 1 and 2, that experience rotation. The rotations of the inner sliding surfaces are due to travel on the outer sliding surfaces. The force of the inner top sliding surface, surface 1, is increased by positive local displacement of the outer top slider, u_3, and the force on the inner bottom sliding surface, surface 2, is increased by the positive local displacement of the bottom outer slider, u_4. To represent these changes in forces on the inner sliding surfaces due to the displacements on the outer sliding surfaces, a geometric stiffness matrix is added. Based on Eqs. 2.21 through 2.27, the 8x8 local geometric stiffness matrix, $\mathbf{k}_g$, is

$$\mathbf{k}_g = \begin{bmatrix} 0 & 0 & \frac{W}{L_{3X}} & 0 & 0 & 0 & 0 & 0 \\ 0 & 0 & 0 & \frac{W}{L_{4X}} & 0 & 0 & 0 & 0 \\ 0 & 0 & 0 & 0 & 0 & 0 & 0 & 0 \\ 0 & 0 & 0 & 0 & 0 & 0 & 0 & 0 \\ 0 & 0 & 0 & 0 & 0 & 0 & \frac{W}{L_{3Y}} & 0 \\ 0 & 0 & 0 & 0 & 0 & 0 & 0 & \frac{W}{L_{4Y}} \\ 0 & 0 & 0 & 0 & 0 & 0 & 0 & 0 \\ 0 & 0 & 0 & 0 & 0 & 0 & 0 & 0 \end{bmatrix} \tag{2.28}$$

The local geometric stiffness matrix is added to the local stiffness matrix, $\mathbf{k}_s$.

2.3 Tangent Stiffness Matrix

Once the local tangent stiffness matrix $\mathbf{k}_s$, the geometric stiffness matrix $\mathbf{k}_g$, and

transformation matrix **T** are assembled, the global tangent stiffness matrix **K** is obtained by

$$\mathbf{K} = (\mathbf{T}_{\mathbf{local}}\mathbf{T})^{\mathrm{T}}(\mathbf{k}_{\mathbf{s}} + \mathbf{k}_{\mathbf{g}})(\mathbf{T}_{\mathbf{local}}\mathbf{T}) \tag{2.29}$$

The stiffness matrix is statically condensed to a 4x4 matrix, which includes the stiffness in the *X* and *Y* directions at nodes *i* and *j* of the bearing and their coupling terms.

$$\widehat{\mathbf{K}} = \begin{bmatrix} k_{XXii} & k_{XXij} & k_{XYii} & k_{XYij} \\ k_{XXji} & k_{XXjj} & k_{XYji} & k_{XYjj} \\ k_{YXii} & k_{YXij} & k_{YYii} & k_{YYij} \\ k_{YXji} & k_{YXjj} & k_{YYji} & k_{YYjj} \end{bmatrix} \tag{2.30}$$

At each displacement increment, both the local and global forces and the tangent stiffness matrix are updated.

The same general approach can be used to model bearings with greater than four sliding surfaces. In such cases, only the transformation matrix and the geometric stiffness matrices need to be changed; the constitutive behavior of the sliding surfaces would be derived for each surface in the same manner. Eq 2.2 would be re-written for the proposed system, and the transformation matrix would be re-derived. With top and bottom and displacement as separate degrees of freedom, the bearing has *n*-degrees of freedom in each direction where *n* is the number of sliding surfaces. Thus, the transformation matrix for an *n*-slider friction pendulum bearing would be *2n*x*2n*. The geometric stiffness matrix would be found by the same method shown in Section 2.2.4.

2.4 Example: One-Dimensional TFP Behavior

To validate the ability of this model to simulate bidirectional behavior of the TFP bearings, test results will be presented in Chapters 3 and 4. However, simpler 1D behavior can be checked against the 1D equilibrium model presented in Section 1.2. To do this, the properties for the TFP used must be within ranges of parameters permitted by the equilibrium model.

An example bearing with acceptable properties is described by the parameters in Table 2.1. The TFP bearing model is then displaced in one direction to its displacement capacity. The computed bearing force-displacement behavior is given in Figure 2.5. Below the plot of the force-displacement hysteresis, the displacements of the individual sliding surfaces are plotted against the total displacement of the bearing. As expected, there are transitions in behavior as the friction forces of the sliders are reached and again as the displacement capacities of each slider are reached. Initially, sliding occurs on the inner sliding surfaces, 1 and 2, then transitions to 2 and 3, and then, once both outer frictional forces have been reached sliding continues on the outer surfaces, 3 and 4. This motion continues until surface 3 reaches its displacement capacity and then sliding occurs on 1 and 4, until surface 4 also reaches its displacement capacity and sliding occurs again on the inner surfaces, 1 and 2. When 1 and 2 reach their displacement capacity the bearing stiffens and motion in the bearing stops. This behavior is in exact agreement with the equilibrium model described before.

Table 2.1 Example TFP bearing properties

	Surface 1	*Surface 2*	*Surface 3*	*Surface 4*
R	11.5in	11.5in	73in	73in
μ	0.02	0.02	0.06	0.09
D_{out}	6.5in	6.5in	27in	27in
D_{in}	3.5in	3.5in	7in	7in
h	1.5 in	1.5in	3in	3in

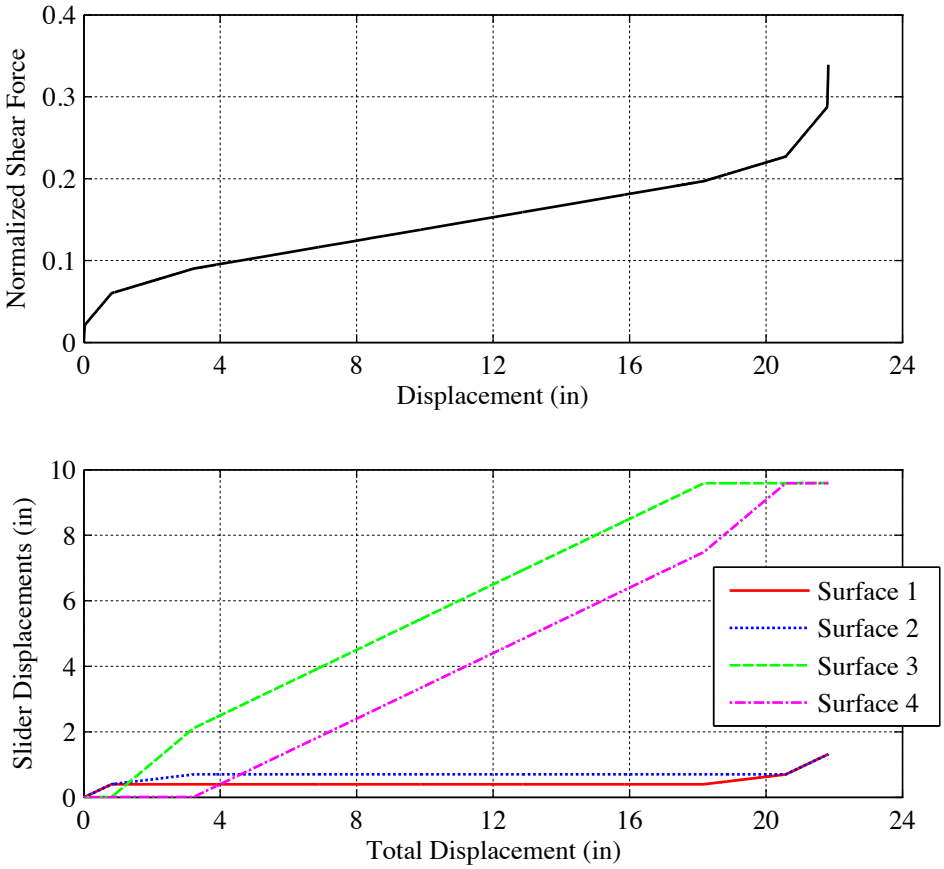

Figure 2.5 1D displacement behavior of kinematic TFP model with individual slider displacements

3 Controlled-Displacement Experiments for Characterizing the Bidirectional Behavior of TFP Bearings

This chapter describes experiments run in order to help understand the bidirectional behavior of triple friction pendulum (TFP) bearings, and to validate the accuracy of the numerical model presented in Chapter 2. Since the tests were needed to characterize the basic hysteretic characteristics of the TP bearings, a simple rigid block model supported on four identical, symmetrically placed bearings was employed. The specimen was placed on the University of California, Berkeley shake table, and restraints were provided to prevent lateral displacement at the bearing plane, while various pre-determined, horizontal displacement histories were imposed to the bottom of the bearings by moving the shake table. In Chapter 4, multi-component ground motions were imposed by the shake table on the same specimen, but with the lateral restraints removed.

3.1 Experimental Setup

3.1.1 Testing facilities

The characterization tests were run utilizing the earthquake simulation table at the Pacific Earthquake Engineering Research Center at UC Berkeley. In these tests, the shake table was used as a bidirectional bearing-test machine. The platform of the shake table has 6 degrees-of-freedom with maximum displacement of ±5 in, maximum velocity of about ±25 in/s and maximum acceleration of ±4 g in both orthogonal horizontal directions. In the vertical direction the maximum displacement is ±2 in and the maximum acceleration is ±1.5 g. The maximum payload is about 165 kips. Because of the limited displacements and velocity capacity of the simulator, reduced scale bearings were used in the tests.

3.1.2 Test specimen

Since the test program focused only on TFP bearing behavior, a simple rigid superstructure was desired. The test set-up was modeled after a similar test one used for single friction pendulum bearings by Mosqueda et al. (2004a). The normal operating pressures on the bearing surfaces in friction pendulum bearings are significant. These are

needed in order to obtain stable friction properties. The axial load needed to achieve these pressures was achieved by placing a rigid mass block on top of the bearings. The weight of the mass block was selected to achieve the desired axial load on the bearings. For simplicity in testing, the mass block was supported by four identical TFP bearings. The resulting degrees of freedom of the test specimen were limited to: the horizontal translation, rotation about the vertical axis of the rigid block and a small amount of vertical translation. This chapter will only investigate horizontal and vertical translation; discussion on torsional behavior will be discussed in Chapter 4.

The geometry of the reduced-scale TFP bearings selected for this study is given in Table 3.1. These bearings, typical of TFP bearings currently in use, have the same geometry for the two inner sliding surfaces and the same geometry for the two outer sliding surfaces. The effective radii of the inner sliders and outer sliders were 2.5 in and 38 in, respectively. The ultimate displacement capacity of the bearings was ±7.73 in. Photos of the bearings used are shown in Figure 3.4. The effective periods at each stage of behavior for these model bearings corresponding to different length scale factors are presented in Chapter 4.

The same composite liner material was used on both surfaces of the inner slider. Different composite materials were used on each of the outer concave sliders. The use of three distinct liners were intended to produce the full range of sliding modes shown in Figure 1.3. However, the actual friction coefficients of TFP bearing linears cannot be determined without experimental testing.

Plan and elevation drawings are shown in Figure 3.2 and Figure 3.1. A photograph of the rigid block set-up is shown in Figure 3.3. A 68 kip rigid block mass assembly was supported by four symmetrically positioned TFP bearings. The bearings were spaced at a distance of 9 ft in the East-West direction and 6 ft in the North-South direction. The rigid block assembly consisted of a steel frame loaded with four concrete bocks. The concrete blocks were post-tensioned to the frame to ensure that they behaved as a single unit. The steel frame facilitated attachment of the isolators to the mass block. In this manner, each bearing supported one quarter of the load, resulting in nominal pressure on the inner sliding surfaces of 3.5 ksi and 2.4 ksi on the outer sliding surfaces.

Bidirectional, controlled-displacement tests were performed by bracing the rigid block assembly to four stiff reaction frames located off of the shake table platform. Pin ended struts, fabricated from square HSS steel sections, were used as bracing members as shown in Figure 3.1. The struts kept the rigid block fixed horizontally, while the shake table was moved through a variety of bidirectional horizontal displacement patterns. The struts were installed with clevises at each end that permitted a limited amount of vertical motion of the specimen. This was important as friction pendulum bearings increase in height when they are displaced laterally.

Table 3.1 Geometry of the TFP bearings used in the experimental characterization

	Inner sliding surfaces	*Outer sliding surfaces*
Dish radius (in)	3.0	39.0
Height (in)	0.5	1.0
Outer diameter (in)	2.5	10.2
Inner diameter (in)	1.5	3.0

3.1.3 Controlled-displacement motions

To achieve the objectives of these tests, a series of controlled-displacement motions were developed to investigate the hysteretic properties of the TFP bearing under a variety of complex unidirectional and bidirectional displacement excursions. The specified displacement orbits included unidirectional sine waves and bidirectional circles, squares and figure eights.

To investigate the behavior resulting from having multiple sliding surfaces, the signals were run with incrementally increasing amplitudes from 0.2 in to 5.0 in. The orbits and displacement time-histories of these tests can be seen in Figure 3.6. The 1D sine wave orbit was used to validate the basic behavior of the bearing and to characterize the friction coefficients for use in the numerical model. The circular orbit was used to verify the effects of 2D plasticity on the bearing sliding surfaces. The square motion was used the see the effect of initial offset on the bearing 1D behavior. Lastly, the figure eight motion was to investigate the behavior in a more complex 2D plasticity problem. All of these orbits tests were conducted with peak velocity of each cycle at approximately 6 in/s.

The maximum displacement capacity of the bearings being characterized was computed to be 7.73 in, while the displacement capacity of the shake table is 5 in. The final hardening stages (when the outer sliders contact their respective restrainers) do not occur until a displacement of greater than 5 in is reached for the model TFP bearings used. To observe the bidirectional behavior of the isolators during the higher stages of the isolators, the rigid block was offset -2.5 in by extending the reaction struts. With the rigid block offset, additional sine and circle displacement orbits were run. A full list of specified shake table motions is given in Appendix A.

3.1.4 Instrumentation

Ninety-two channels were used to measure the response of the rigid block and bearings during the controlled-displacement tests. A channel list is provided in Appendix B. A Pacific Data Acquisition System was used to record the responses of each channel. Sampling was done at 500 Hz.

Five-component load cells were located under each bearing to measure and record axial, shear and moment response. All five of the reactions were recorded from below each bearing; together, the load cells used twenty channels.

Twenty-two transducers were used to monitor the table behavior, including eight displacement transducers and fourteen accelerometers. The remainder of the transducers was used for detailed monitoring of the behavior of the bearings and the rigid block above. Wire potentiometers from stiff instrumentation frames located off of the table were used to measure absolute displacement of the steel frame and the top of the rigid concrete block. Direct current displacement transducers (DCDT) were used to measure the horizontal displacement of the bottom of the isolators relative to the table in case of possible deformations in the load cells and base slip. A photo showing detailed instrumentation surrounding the bearing is given in Figure 3.5. DCDT's were also used to measure slop in the strut clevises. Four wire pots were used at each corner of the frame to measure the vertical displacement relative to the table. Accelerometers were used to

measure *X*, *Y* and *Z* acceleration at plates between the bearings and the load cells and at the frame level. *X* and *Y* acceleration was measured at the top center the rigid block. As there was redundancy in the instrumentation, the averages from multiple measurements were used.

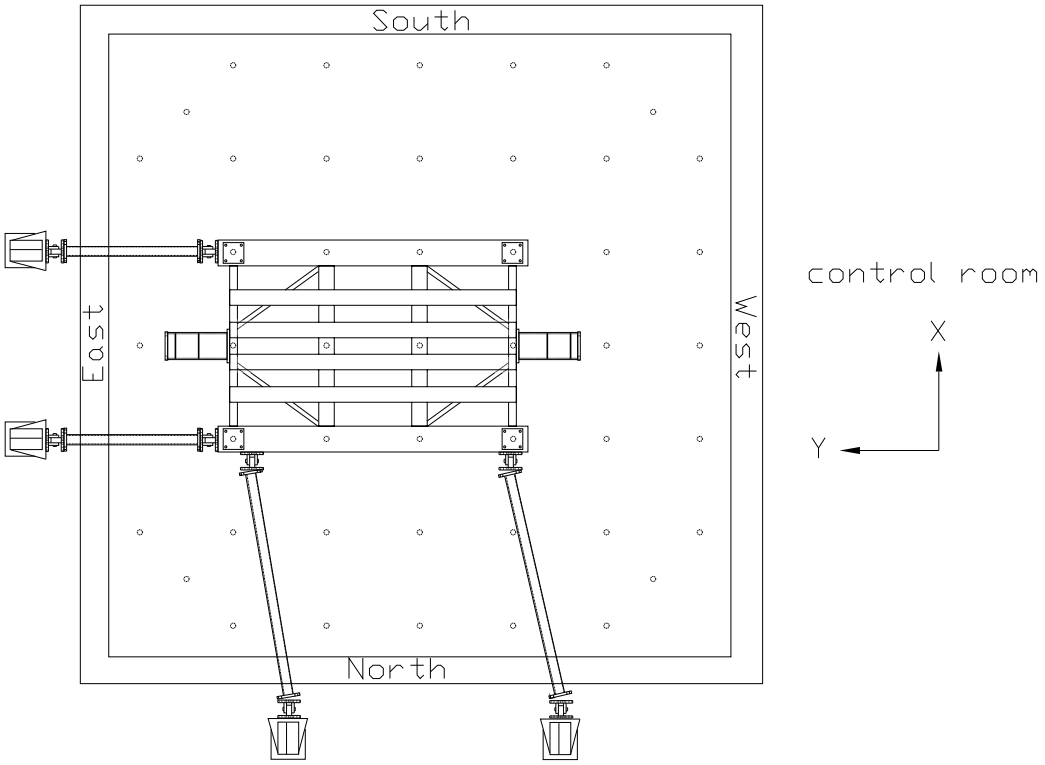

Figure 3.1 Plan view of the rigid block model with struts attached

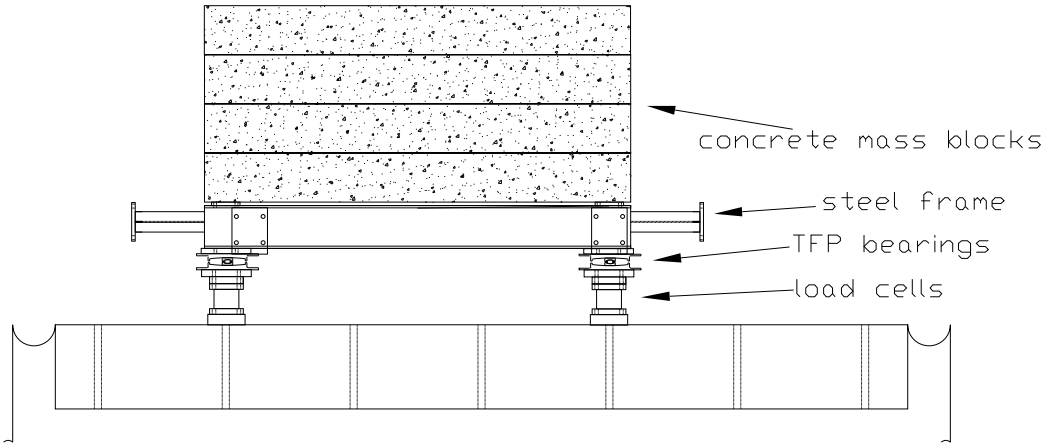

Figure 3.2 Elevation view of the rigid block model

Figure 3.3 Rigid block experimental setup at the UC Berkeley PEER Earthquake Simulator Laboratory

Figure 3.4 Components of the TFP bearing

Figure 3.5 View of instrumentation surrounding the TFP bearing

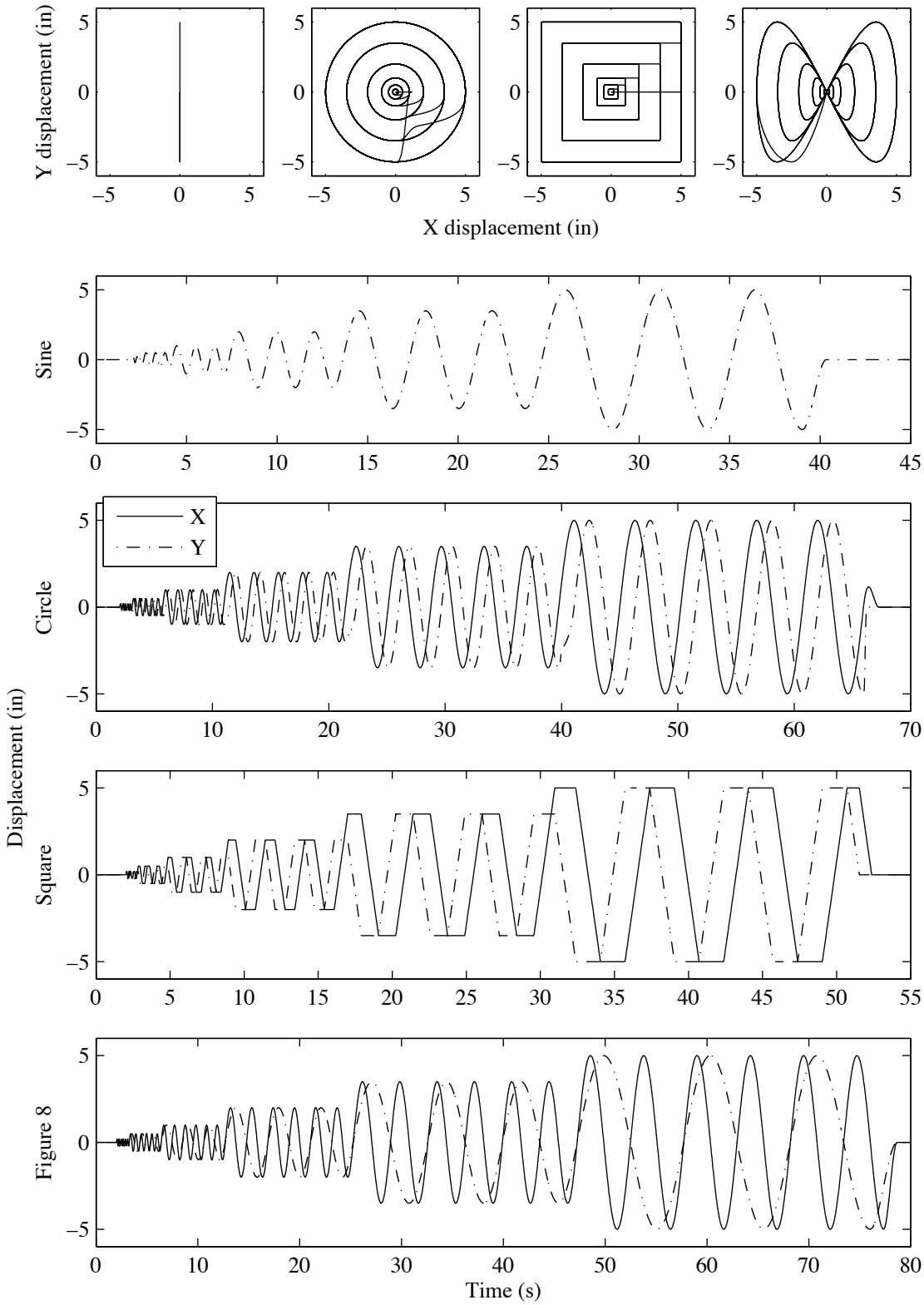

Figure 3.6 Controlled-displacement orbits used for bearing characterization including sine waves, circles, squares and figure eights

3.2 Comparison of Experimental and Numerical Results

The test results for all four displacement orbits are presented, including plots of (1) displacement orbits in the *X*-*Y* plane, (2) normalized base shear paths in the *X*-*Y* plane, and (3) normalized base shear-bearing deformation hysteretic loops for the *X* and *Y* directions. The specimen base shear is normalized by the weight of the specimen, to give the average effective friction coefficient exhibited by for the bearings. As the axial load continually changes on the bearings, the shear must be normalized by the axial load measured at each data sample. The experimental results presented show the average behavior of the four bearings in the setup.

The behavior exhibited under the 1D sine wave displacement history (Figure 3.7) is similar to what is expected in general based on the theoretical considerations presented in Chapters 1 and 2. The hysteretic loops at the initial movement on the outer sliding surfaces is a slightly higher than in subsequent cycles. This may reflect a misalignment of the sliders at the start of testing, or temperature sensitivity of the bearing material (see Section 3.3.3). Hysteretic loops projected onto the *X* and *Y* planes are more complex as would be expected for the cases of bidirectional displacement response (see Figure 3.8 through Figure 3.10). This complexity provides the impetus for developing the kinematic model presented in Chapter 2.

In the remainder of this chapter, test results are examined in terms of the theoretical concepts described in Chapter 1 and 2 or compared with predictions based on the numerical model developed in Chapter 2. Results are interpreted to identify the friction coefficient for each of the sliding surfaces, characterize the sensitivity of hysteretic response to velocity, pressure and temperature, and assess various other behavioral characteristics of the TFP bearings under bidirectional loading.

3.2.1 Friction coefficients

The friction coefficient for the sliding surfaces of a friction pendulum must in general be determined from test results. In practice, design engineers specify a range of acceptable friction coefficients for individual bearings, as well as group means.

Typically, friction coefficients are interpreted using the procedure described by Morgan (2008) or similar method. Lateral force - lateral deformation hysteresis loops are obtained for the bearing in question by applying a series of symmetric, unidirectional displacement cycles. To measure the three friction coefficients in TFP bearings, cycles with different amplitudes are imposed to activate only the first, the first and second, and the first, second and third stages of motion. The shear force in the bearing is normalized by applied axial load, and the heights of the resulting normalized hysteretic loops, denoted as H_1, H_2 and H_3, are measured at zero lateral displacement. In this test program, a series of sine wave displacement histories was devised to initiate sliding on the three pendulums (inner, outer bottom and outer top) incrementally.

The smallest coefficients of friction μ_1 and μ_2 are those of the inner sliders (as shown in Figure 1.2). Since the composite liners on these surfaces are the same, it is assumed that $\mu_1=\mu_2$ and that the coefficient of friction is simply H_1 divided by two. The

third coefficient of friction, for the bottom surface of the lower concave sliders, is found by

$$\mu_3 = \frac{\frac{H_2}{2}(L_1 + L_3) - 2\mu_1 L_1}{L_3 - L_1} \tag{3.1}$$

The fourth coefficient of friction, for the top outer surface, is found as

$$\mu_4 = \frac{\frac{H_3}{2}(L_3 + L_4) - \mu_3(L_3 - L_1) - 2\mu_1 L_1}{L_4 - L_1} \tag{3.2}$$

This method assumes that the third and fourth friction coefficients are distinct. If they are not distinct, which is sometimes the case in practice, then the second stage of motion is skipped and motion is initiated on both outer sliders simultaneously as discussed in Chapter 1. The second and third friction coefficients in this case are equal and found as

$$\mu_3 = \mu_4 = \frac{\frac{H_2}{2}(L_3 + L_4) - 2\mu_1 L_1}{L_3 + L_4 - 2L_1} \tag{3.3}$$

This method was used to find the friction coefficients of the bearings used. The hystereses loops from unidirectional sine wave displacement history imposed at 6 in/s peak velocity were used to compute the friction coefficients. This peak velocity is the same value as used in the circular, square and figure eight orbit tests.

The friction coefficients determined from the sine wave tests were found as 0.036, 0.118 and 0.128. The latter two values were closer than anticipated, but representative of practical applications and deemed adequate for the purposes of this study.

3.2.2 Hysteretic loops

The measured displacement histories imposed on the test specimens were applied to a numerical model of the test set up. The numerical model, described in Chapter 2, was developed in Matlab based on the geometric properties of the bearings presented in Table 3.1, and the friction coefficients identified in Section 3.2.1.

The results of the numerical model are now compared to the experimental results to evaluate its ability to accurately capture the behavior of the TFP bearing under controlled-displacement motions. In this section, focus is on realistic hysteretic loop characteristics; other aspects of behavior are examined in later sections. In general, comparison of the experimental and numerical results, presented in Figure 3.7 through Figure 3.10, indicates that the numerical model is able to track the hysteretic behavior of the bearings very well, even where the experimental loops exhibit highly complex characteristics under bidirectional motion.

One major difference between the experimental and numerical hysteretic loops is that the transition between stiffnesses is smoother in the experimental model due to velocity effects discussed later in Section 3.3.1. This is best seen in the hystereses loops

for the unidirectional sine wave motion (Figure 3.7). This observation is particularly acute for the bearings tested herein due to the nearly equal friction coefficients for the outer two sliding surfaces of the concave sliders. However, this behavior was also noted generally in dynamic tests done by Fenz and Constantinou (2007b) and Morgan (2008).

Due to the complexity of the hysteretic behavior under bidirectional displacement excursions, three marks (red circle, yellow square and green triangle) are added in the response plots for the numerical model results in Figure 3.8 through Figure 3.10. These show the progression of the bearing behavior during one loop, in red-yellow-green chronological order. The hysteretic loops for the square orbit test (Figure 3.9) shows how when the bearing changes direction by 90 degrees from the *Y*- to the *X*-direction, the hysteretic friction force changes direction during a small displacement increment. Then, while the bearing moves in the *X*-direction, the force remains constant in the *Y*-direction. However, the force in the *Y*-direction is non-zero as the bearing is still displaced in this direction.

Since the TFP bearing exhibits hysteresis, the global displacement of the bearing will nearly always be non-zero at the end of a loading history. However, in the controlled-displacement tests employed here, the bearings were returned to zero displacement at the end of each test. Because of this, the bearings retained a residual force at the end of each controlled-displacement tests. The residual forces are best shown in the force paths for the circular and square orbits in Figure 3.8 and Figure 3.9, respectively. The numerical model accurately predicts the residual force.

As will be described in more detail below, the inner slider and concave sliders did not return to zero displacement at the end of a test, even though the global displacements were zero. Because of the practical difficulty of recentering the internal sliders, subsequent tests were generally started with the internal sliders in the offset position that remained at the end of the prior test. However, subsequent experimental results did not show significant changes in hysteretic behavior due to the initial forces and the offset of the internal sliders.

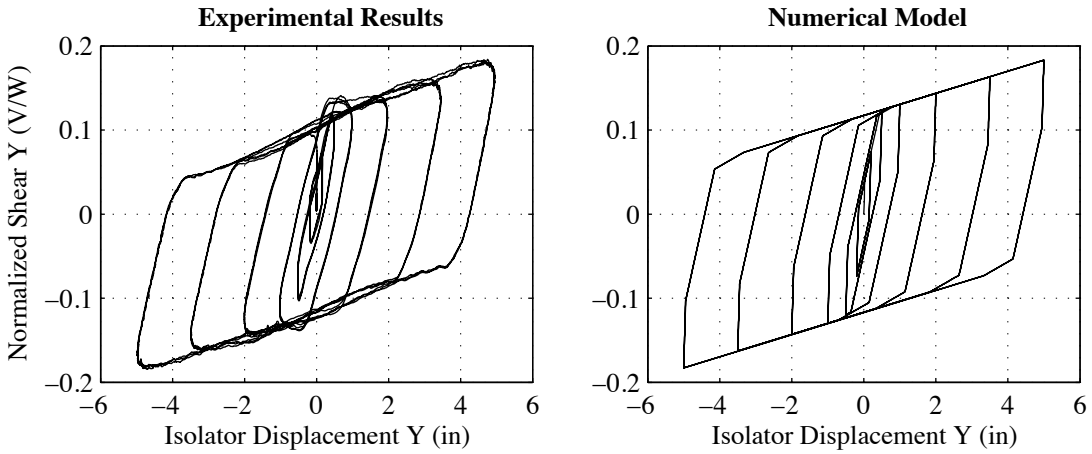

Figure 3.7 Experimental and numerical hystereses for the sine wave displacement orbit

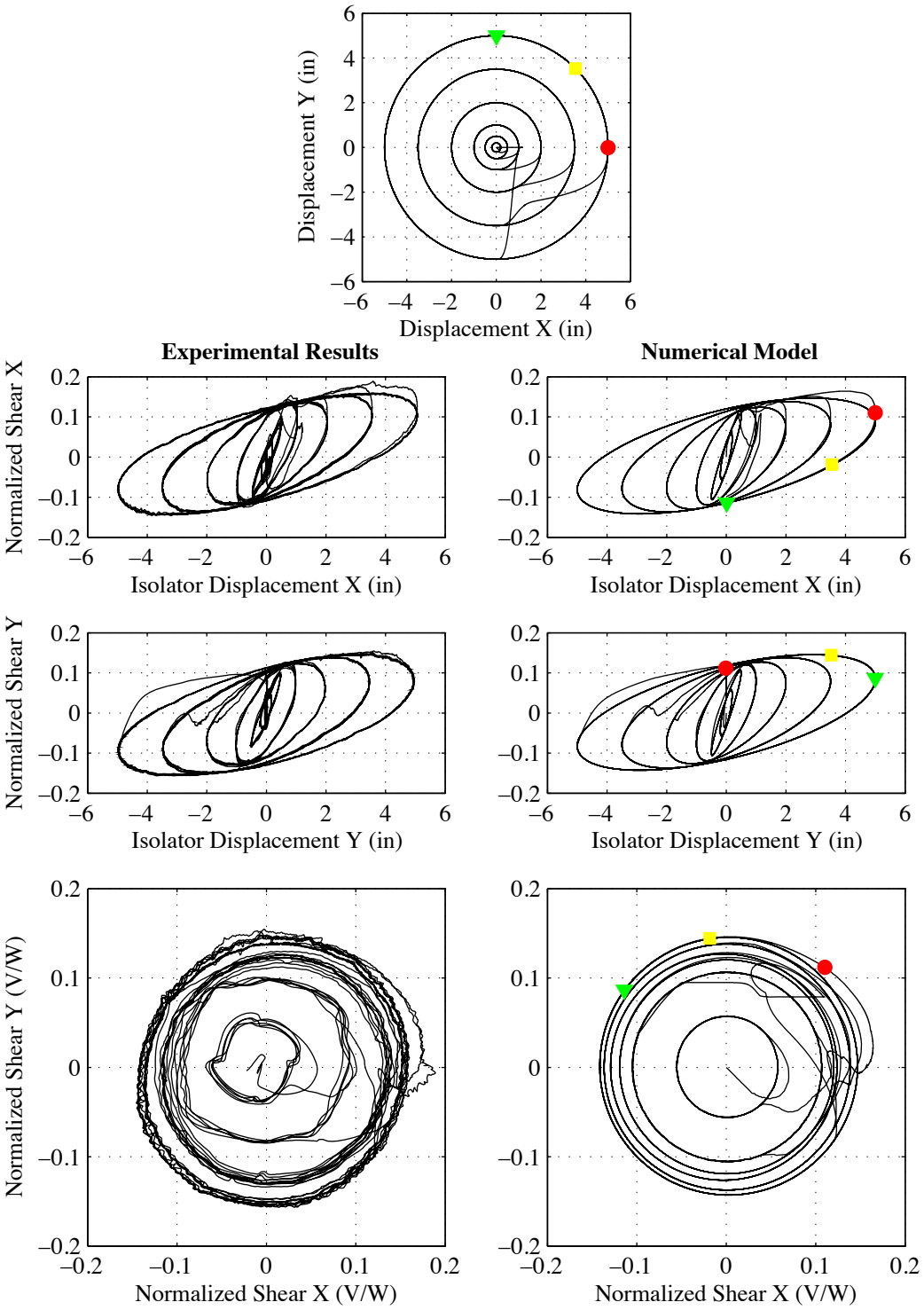

Figure 3.8 Experimental and numerical hystereses and normalized force paths for the circular displacement orbit

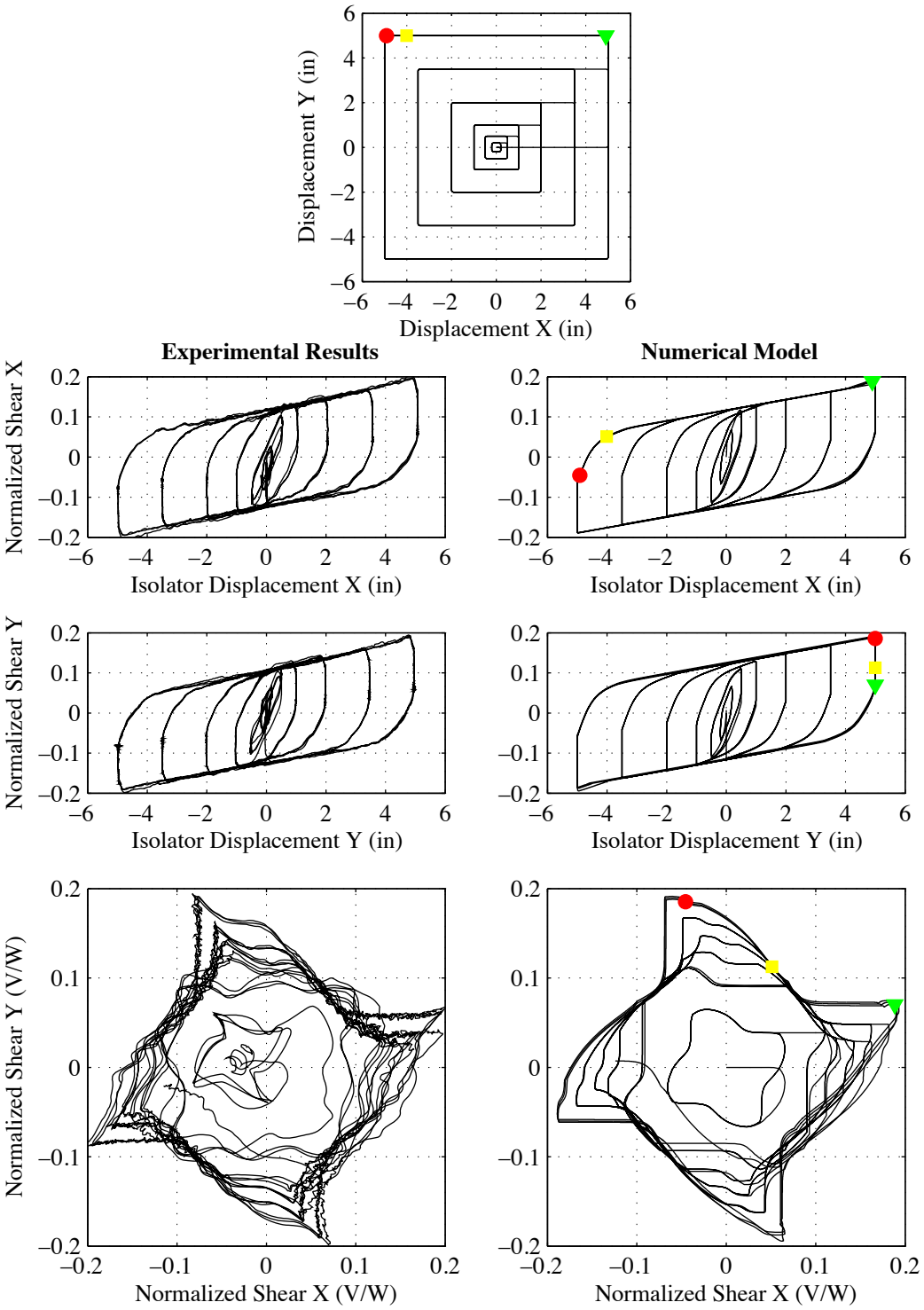

Figure 3.9 Experimental and numerical hystereses and normalized force paths for the square displacement orbit

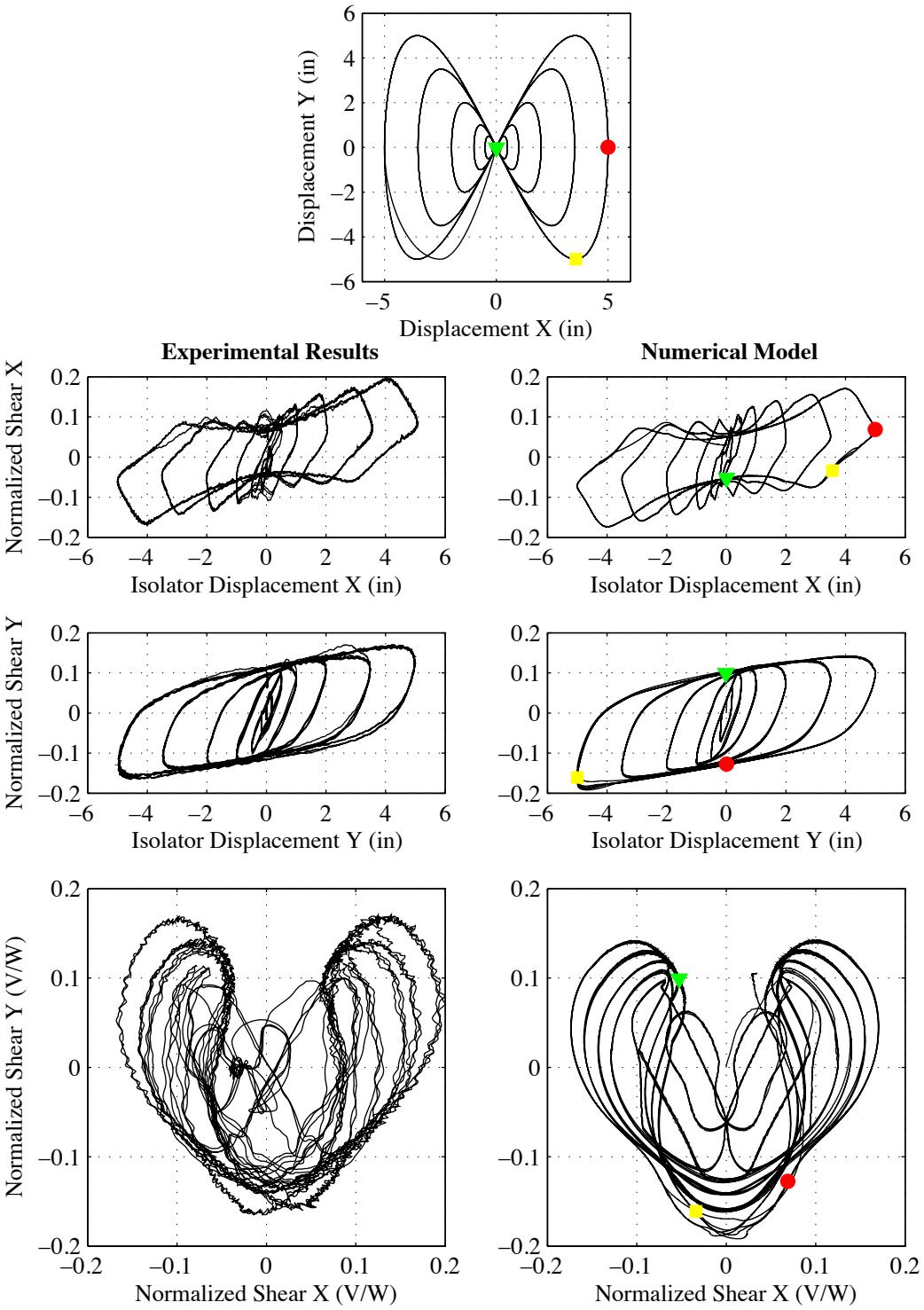

Figure 3.10 Experimental and numerical hystereses and normalized force paths for the figure eight displacement orbit

3.2.3 Tracking slider displacements

The numerical model presented in Chapter 2 tracks the motion of the inner and concave sliders in order to accurately model the bidirectional plasticity and restrainer interaction. This ability to track the movement of the sliders provides an excellent opportunity to visualize what is happening in the TFP bearing when it is in motion. The computed slider displacements for the controlled-displacement motions are shown in Figure 3.11 through Figure 3.14. Unfortunately, during the experiments, slider components relative displacements could not be measured to compare with the analysis results.

The slider displacements are marked with the red circle, yellow square and green triangle at the same times as in the hysteretic behavior plots discussed in Section 3.2.2. It is interesting to note that for the circle and square orbits that at large displacements the outer sliders move in the direction of predominant motion while the inner sliders travel at a direction roughly 45 degrees to the direction of predominant motion.

All bidirectional orbits, to some degree, show the outer bottom bearing exhibiting displacements shifted in the opposite direction from the outer top bearing. This is because friction coefficient of the bottom slider is slightly smaller than that of the top slider. If the friction coefficients were the same, both outer concave sliders would have the same displacements. Additionally, both inner sliders would have the same displacements. With different friction coefficients for the outer sliders, the motion initiates on the bottom slider before the top slider. Thus, on the return motions, the top slider already is offset from the bottom slider.

Even when the global displacement of the bearing is zero this does not imply that the inner sliders have zero displacements. For example, for the slider displacement loops for the unidirectional sine wave loading in Figure 3.11, the sliders are offset at the end of the motion even though the global controlled-displacement returns to zero at the end of the test.

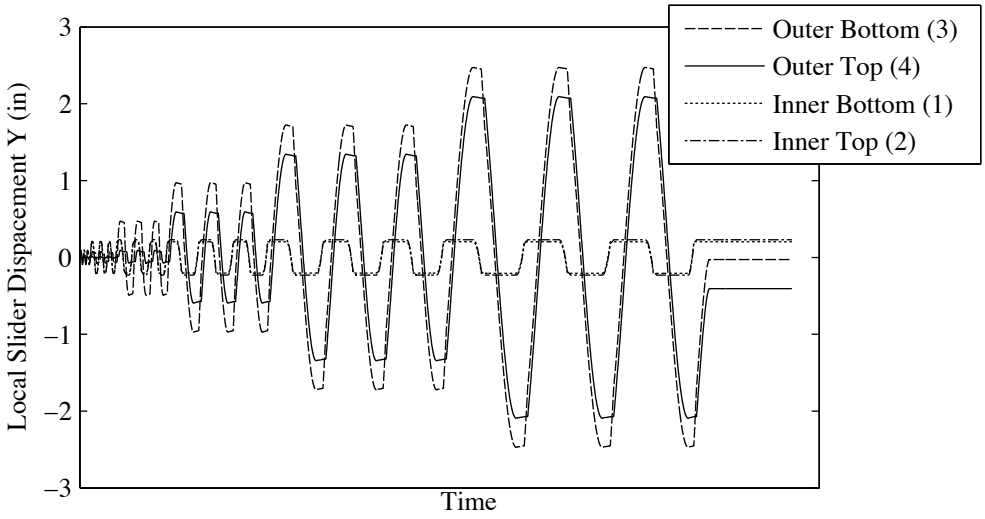

Figure 3.11 Slider relative displacements in the *Y*-direction over time from the numerical model for the sine wave displacement orbit

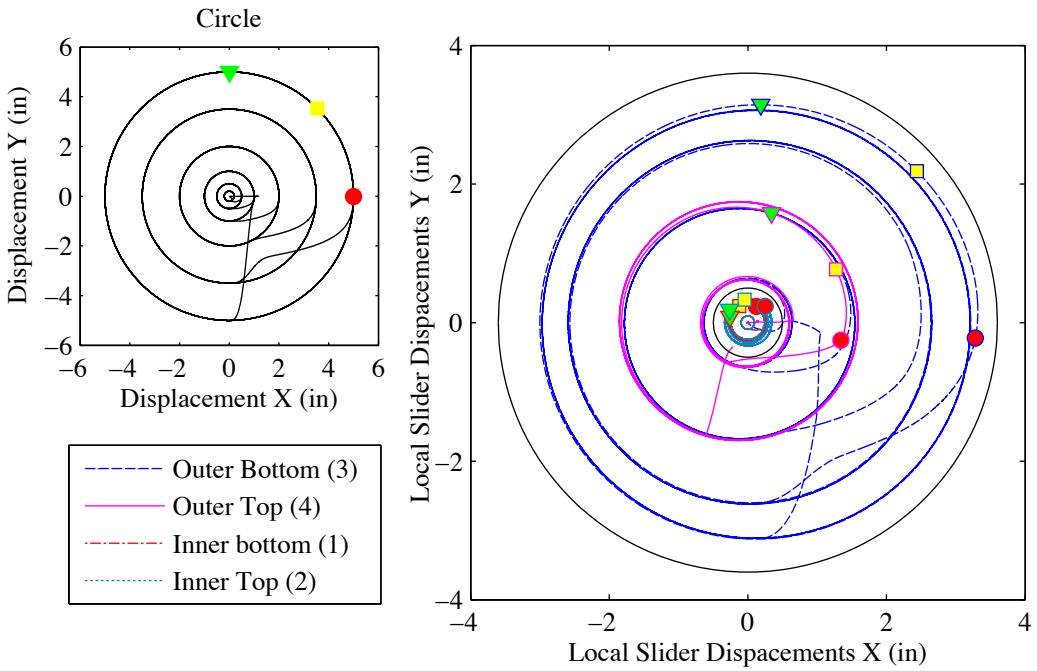

Figure 3.12 Slider relative displacements in the *X*- and *Y*-directions from the numerical model for the circular displacement orbit

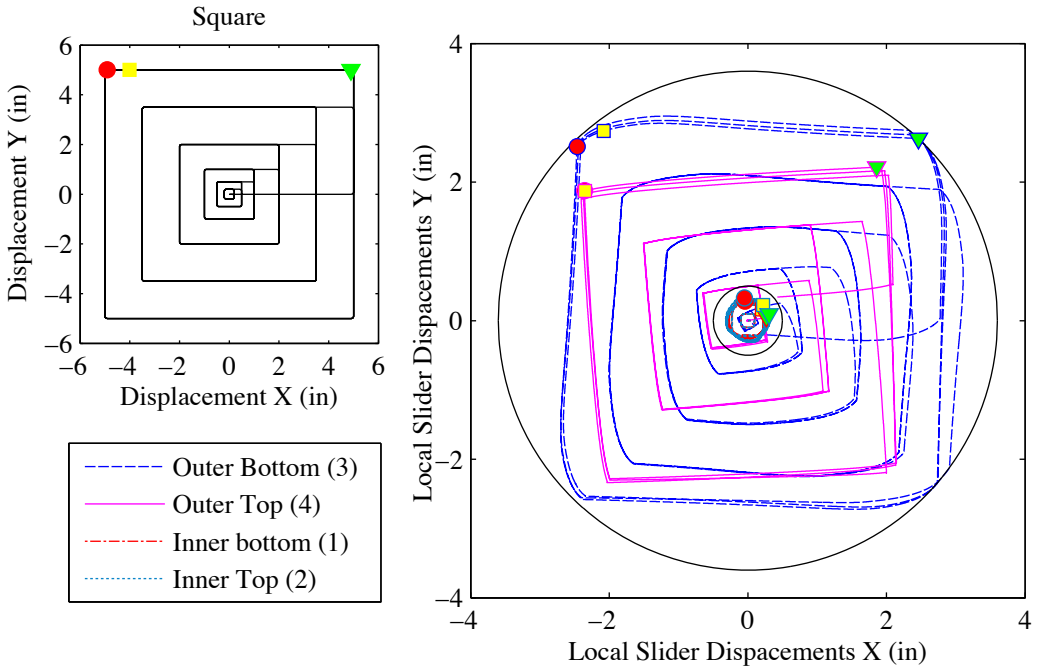

Figure 3.13 Slider relative displacements in the *X*- and *Y*-directions from the numerical model for the square displacement orbit

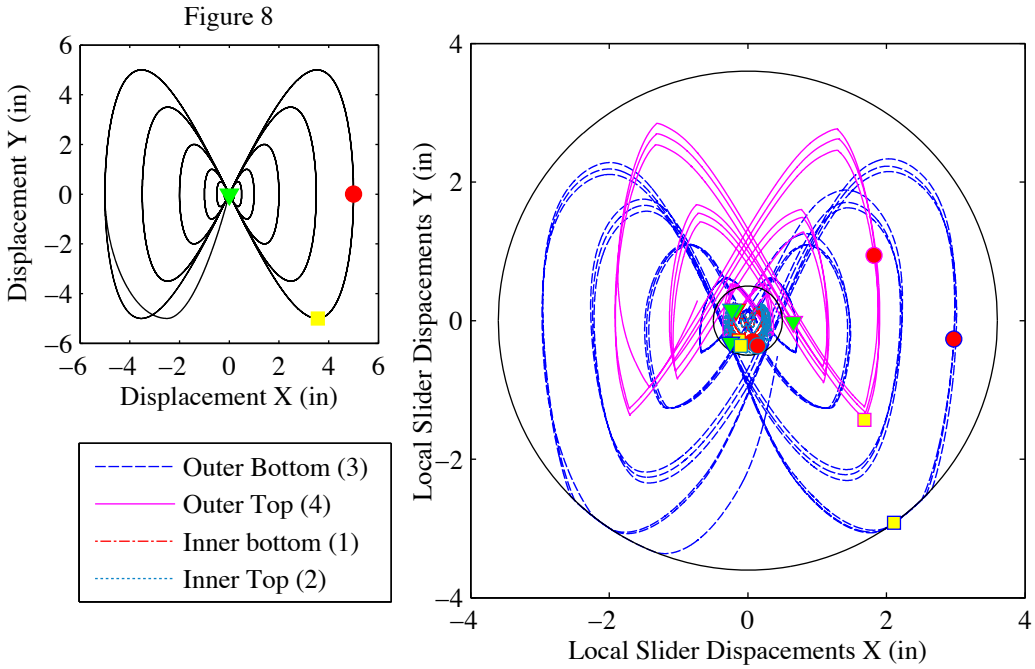

Figure 3.14 Slider relative displacements in the *X*- and *Y*-directions from the numerical model for the figure eight displacement orbit

3.2.4 Change in bearing height

As the slider displacements are known, the change in bearing height during the course of a motion can be computed. Change in height in the isolation layer is important to know for detailing of the interstitial layer, particularly for architectural detailing that may be affected. To measure the change in height, the absolute displacement on each sliding layer (not measured at the center of the bearing as described in Chapter 1) must be known. The displacement on the sliding layer, u_n', is greater that that measured at the center of the bearing and is found as

$$u_n' = \sqrt{u_{nX}^2 + u_{nY}^2}\,\frac{R_n}{L_n} \tag{3.4}$$

Each of the five separate components of the bearing have an original thickness, t_0, measured at zero displacement. Each component will be lettered from *a* through *e*, from the bottom to the top of the bearing. To find the change in height, the change in the thicknesses of the bearing components at the displaced configuration must be calculated. Each sliding surface is spherical with radius R_n. When a point is displaced by u_n' from the bottommost position on a sphere, the change in height is $R_n - \sqrt{R_n^2 - u_n'^2}$. Thus, the change in thickness in component *b* when there is displacement on surface 1 but zero displacement in surface 3 is $R_1 - \sqrt{R_1^2 - u_1'^2} - R_3 + \sqrt{R_3^2 - u_1'^2}$; this is illustrated in Figure 3.15. Once there is displacement on surface 3, component *b* is rotated and the vertical thickness is the thickness perpendicular to the component multiplied by the cosine of the

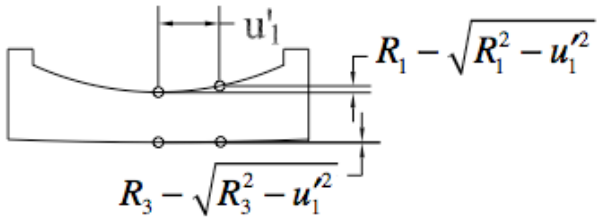

Figure 3.15 Change in height of component *b* when there is displacement on surface 1 and no displacement on surface 3

component's rotation. The thicknesses for all components with any offset configuration are found as

$$
\begin{aligned}
t_a &= R_3 - \sqrt{R_3^2 - \left(u_3' + u_1' \tan\theta_3\right)^2} \\
t_b &= \left[t_{b0} + R_1 - \sqrt{R_1^2 - u_1'^2} - R_3 + \sqrt{R_3^2 - u_1'^2} \right] \cos\theta_3 \\
t_c &= t_{c0} \cos\left(\theta_1 + \theta_3\right) \\
t_d &= \left[t_{d0} + R_2 - \sqrt{R_2^2 - u_2'^2} - R_4 + \sqrt{R_4^2 - u_2'^2} \right] \cos\theta_4 \\
t_e &= R_4 - \sqrt{R_4^2 - \left(u_4' + u_2' \tan\theta_4\right)^2}
\end{aligned}
\tag{3.5}
$$

The change in bearing height is then found as

$$
dt = \sum_{i=a}^{e} t_i - \sum_{i=a}^{e} t_{i0} \tag{3.6}
$$

The time-histories for the changes in height found from the experimental results and from the numerical model for all controlled-displacement orbits are given in Figure 3.16. The experimental measurements for change in height, measured from the top of the shake table platform to the bottom of the steel frame, were corrected for horizontal displacements of the bearings.

The changes in height for the different orbits calculated from the local slider displacements have the correct shape patterns and magnitudes. However, there are some major variances. For example, for the sine and square orbits, the peak heights from the experimental data vary over the path for specific displacement amplitudes. The sine wave exhibits a larger change in height for a positive lateral displacement than a negative one. The square has different peaks in height at each corner of the square. This is not seen in the numerical model, likely because the numerical model was run with no initial offsets in the internal sliders. Although initial offsets did not appear to change bearing global hysteretic behavior in the horizontal directions, as discussed in Section 3.2.2, they do affect the local slider displacements and thus change the bearing thickness.

The experimental results for the circular orbits show significantly more fluctuation in height over the paths than the numerical model. During a circular motion all sliders move in circular paths, minimizing change in height. If outer sliders have different friction coefficients displacements are shifted as discussed in Section 3.2.3, resulting in small fluctuations in height seen in the numerical model. However, initial

offsets of internal components would result in larger changes in heights as the center of the circular paths for the sliders are offset from each other.

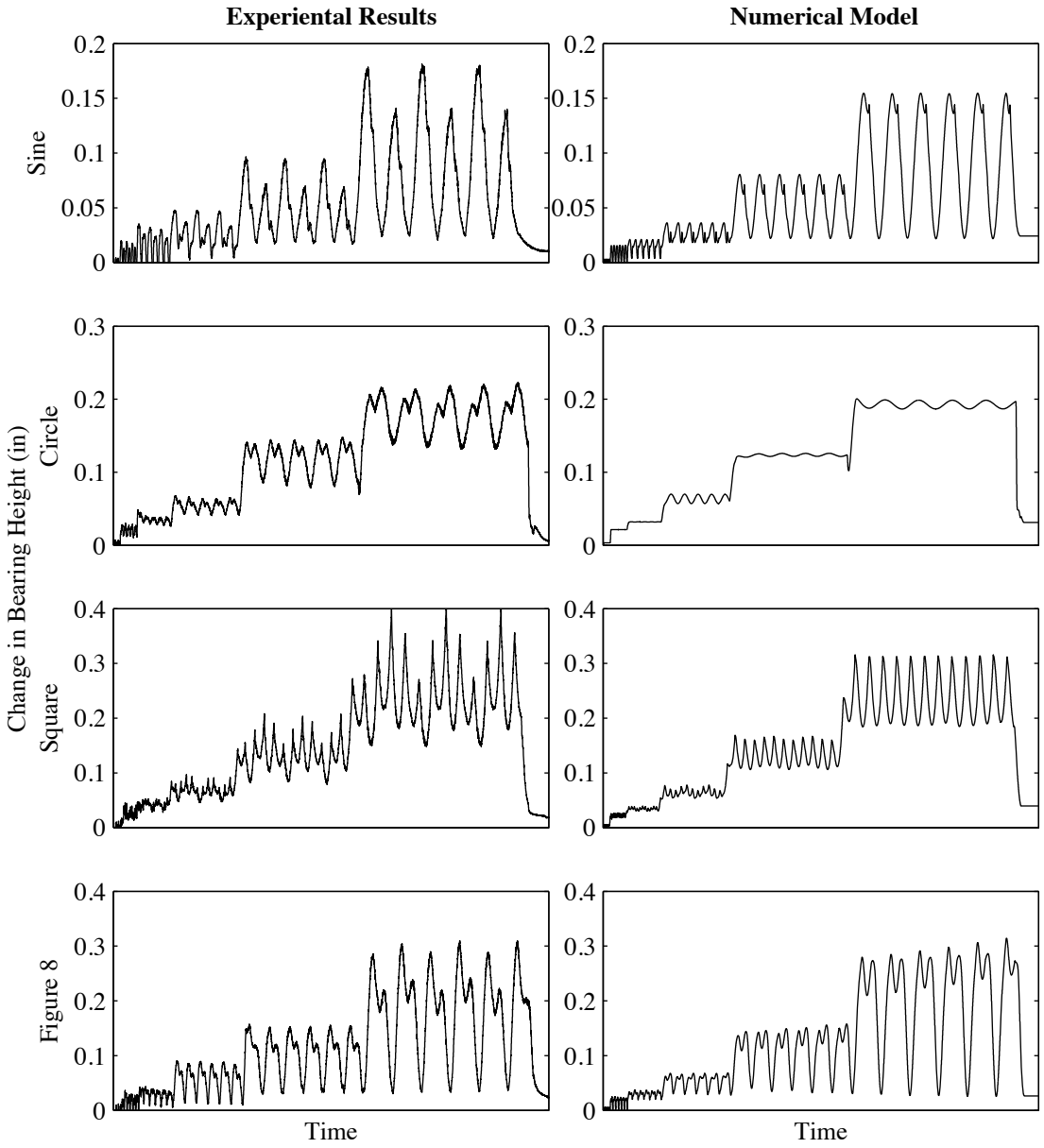

Figure 3.16 Change in bearing height over course of motions for sine, circle, square and figure eight orbits

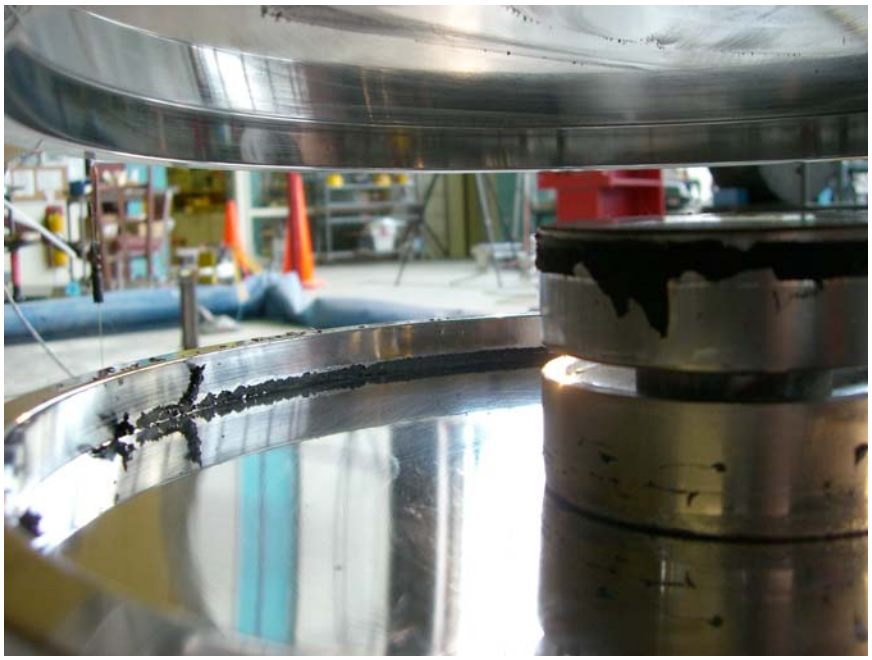

Figure 3.17 Rubber gasket wear along the restraining surface.

3.2.5 Rotation of sliders about a vertical axis

The inner sliders were observed to rotate around a vertical axis during the bidirectional tests. This results from a number of factors associated with the finite size of the sliding surface, including the likely non-uniform pressure distributions on the internal sliding components and difference in work over the sliding surface during bidirectional motion. Furthermore, when the a sliding component comes in contact with a restraining rim, rotation occurs due to the contact friction between the restraining rim and the vertical surface of the slider. The friction force between the slider and the restrainer wall is not likely negligible. Twisting of the rubber gasket connecting the concave sliders during unrestrained sliding, and the wear and failure of the rubber gasket due to contact with the restraining rim was observed in the controlled-displacement bidirectional motions. This is shown in Figure 3.17. Any effect on the travel of the slider by the friction force from interaction with the restraining rim, or from torsional behavior in general, increases the energy dissipated by the bearing. However, the rotational of the sliding surfaces and the tangential friction on the restrainers is not incorporated into the model presented in Chapter 2 and remains a topic of continuing investigation.

3.2.6 Offset motion

To test the bearing past the 5 in capacity of the controlled-displacement shake table setup, the rigid block was displaced -2.5 in by lengthening the reaction struts in the *Y* direction, and re-centering the table. Once displaced, run-in motions were done followed by the same unidirectional sine wave and bidirectional circle orbits used before.

One complication in trying to compare the experimental and numerical results for the offset motion, especially after running previous motions, is that the inner sliders of the bearings have initial unknown offsets. The same is true for non-offset motions; however, the earlier motions had smaller peak lateral displacements, thus there was less interaction with restraining rims. To numerically model the offset sine wave motion, the bearing was first displaced -2.5 in in the negative *Y* direction as done in the offset experiments. Prior displacement histories in the *Y* direction were selected to achieve this displacement with a residual normalized force of approximately -0.04 to match the initial force seen in the experimental data. After the displacement history was run to offset the specimen properly and initialize the force appropriately, the sine orbit was then run.

Two different prior displacement histories were used, resulting in two different initial offsets. The first prior displacement history was -2.75 in, -2.5 in, resulting in initial slider offsets $\begin{bmatrix} u_1 & u_2 & u_3 & u_4 \end{bmatrix} = \begin{bmatrix} -0.089 & -0.115 & -1.338 & -0.958 \end{bmatrix} \text{in}$. The second prior displacement history was -7.0 in, -2.2 in, -2.5 in, resulting in initial offsets $\begin{bmatrix} 0.066 & 0.091 & -1.139 & -1.518 \end{bmatrix} \text{in}$. The experimental and numerical hystereses for the unidirectional sine wave are shown in Figure 3.18.

The first set of initial offsets results in stiffening to Stage 4 behavior at larger negative global displacements, also seen in the experimental test. The second prior displacement history resulted in greater initial offset of the top outer slider than the bottom outer slider. Thus, the hysteresis varies from that with the first set of initial offsets. Instead of gradual stiffening to Stage 4, the bearing behavior goes directly from Stage 3 behavior to Stage 5 with a much sharper transition in stiffness. This would occur when the displacement capacities of the outer sliding surfaces were reached at the same time. The bearing behavior differs between the two cases only within an inch of the maximum bearing displacement capacity. The experimental hysteresis exhibits some pinching, which is not captured in the numerical runs. Additionally, the experimental data shows a slightly larger range of force than the numerical model. These effects may likely be attributed to the experimental setup. During the larger lateral displacements of the bearing, the vertical bearing displacements increases, so that the inclination of the struts used to the restrain the rigid block affected the axial load on the bearings during the motion.

To model the offset circular motion, a prior displacement history in the *Y* direction of -5 in, -2 in, -2.5 in was run before the circular orbit resulting in a normalized force offset of -0.07 to match the experimental initial force offset. Experimental and numerical hystereses are shown in Figure 3.19. The comparison between the experimental and numerical results shows the same variations seen in the offset sine comparison: pinching in the experimental results and a slightly larger range of force.

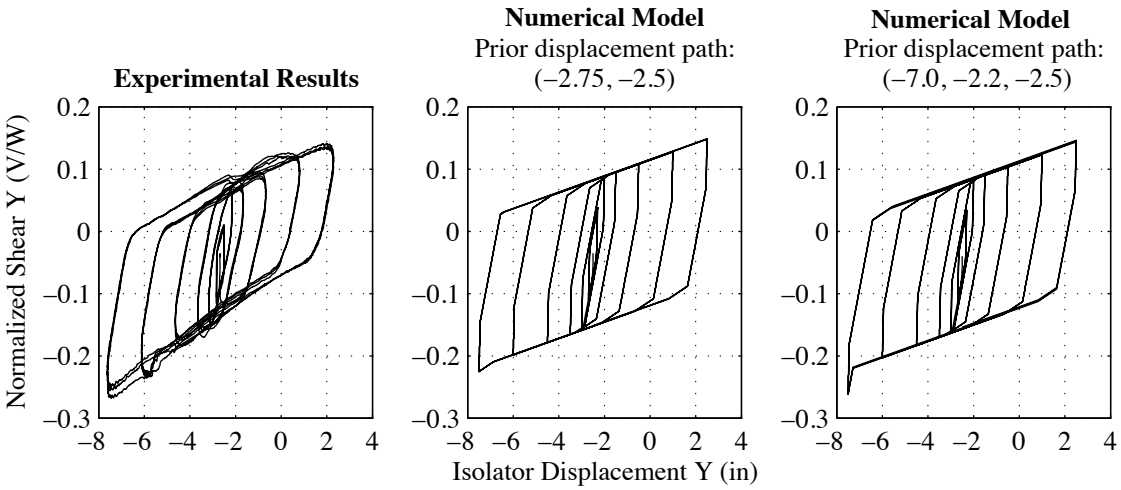

Figure 3.18 Experimental and numerical hystereses for the offset sine wave displacement orbit

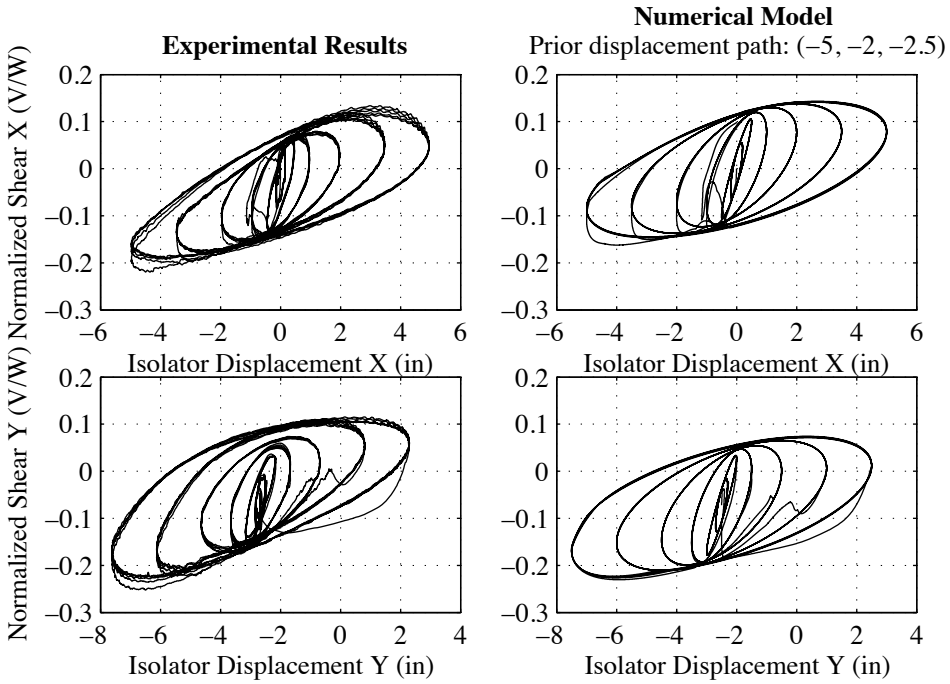

Figure 3.19 Experimental and numerical hystereses for the offset circle displacement orbit

3.3 Friction Coefficient Dependencies

Velocity, pressure and temperature all affect the friction coefficients of the four sliding layers of a TFP bearing. In general, the friction coefficient on each surface must be modeled independently since the velocity, temperature and pressure on each surface are different. The TFP model developed permits the velocity to be tracked on each of the sliding surfaces. However, as discussed below, characterization of velocity dependencies

in situ are difficult with TFP bearings. Temperature effects on friction pendulum bearings can be observed, but not easily measured experimentally or modeled numerically. As noted previously, the pressure on a bearing surface is likely non-uniform due to various factors, including bending moments resisted by the sliders (and typically ignored in numerical models) and stress concentration effects due to the deformability of various components and the liner material itself. The effect of pressure, temperature and velocity variations depend on the properties of the proprietary composite liner materials used. These values are not easily available. In this section, experimental results will be re-examined. In this case, focus will be on assessing the significance of velocity, pressure and temperature effects.

3.3.1 Velocity

The liners in a friction pendulum bearing are made from a wide variety of composite materials, often from Teflon, carbon or a combination of such materials. Due to the proprietary nature of these liners, is it difficult to fully characterize their properties for general numerical use.

Constantinou et al. (1999) showed that the friction coefficient for one type of liner material increases with velocity from μ_{min} before plateauing at a maximum of μ_{max} following the relation

$$\mu = \mu_{\max} - (\mu_{\max} - \mu_{\min})e^{-a|v|} \tag{3.7}$$

where *a* is a constant that describes the rate of the transition from low to high velocities. Some liner materials exhibit a relatively high initial breakaway friction coefficient. Mokah et. al (1991) showed that Teflon experience an initial breakaway stiffness, but only when they have not been relative motion on the bearing for a long period of time. No breakaway friction effects were noted in the tests described in this chapter.

While such models may be needed in numerical simulation of rate-dependent bearing behavior, different velocities are expected at any point in time on the four sliding surfaces in a TFP bearing. Figure 2.5 shows the individual slider displacements for monotonically increasing global displacement of a bearing. Even if the global bearing velocity remains constant, this figure suggests that the relative velocity on each sliding surface changes at every transition in behavior. In any real seismic event, where global displacement rates change amplitude and sign, the variation of relative velocities on the bearing surfaces would likely change in very complex ways.

While the proposed numerical model is able to predict these relative velocities, the absence of data on the friction dependence on velocity poses a practical challenge. Characterization tests could be done as described at different global velocities to impose the desired relative velocity on the surfaces of interest. Because of the different velocities on each surface during these tests, this procedure is approximate. Individual composite liners could be characterized. However, this type of testing would not retain the sensitivity of the actual bearing surface to temperature or pressure.

The unidirectional sine wave history was experimentally re-run with three peak velocity values, 6 in/s as discussed previously, as well as 3 in/s and 9 in/s. Because the radii of the inner sliding surfaces are the same, if motion is occurring on both surfaces during a 1D excitation (Stage 1 motion), the velocity is the same on both sliders. The

same is true for the outer sliders. However, when Stage 2 sliding occurs, (sliding on the inner top slider and the outer bottom) the velocities on the two sliders are different. During Stage 2 the velocity on sliding surface 3 (the outer bottom surface) is $v_{total}\, L_3 / \left(L_2 + L_3 \right)$. The calculated friction coefficients and the corresponding velocities from the three sine wave histories are given in Table 3.2. Ideally, more data would be available to characterize velocity dependence. From these results, it appears that, except for surfaces 1 and 2, substantial changes in velocity have modest effects on the friction characteristics of the various sliding surfaces. This is illustrated by the good agreement of the numerical model with test results over a wide range of excursions.

Multiple researchers including Fenz and Constantinou (2008b) and Politopoulos (2008) have shown that inclusion of velocity effects in TFP bearing modeling, smoothes transitions between sliding stages, which was a difference between experimental and numerical results discussed in Section 3.2.2.

Table 3.2 Friction coefficients found from sine wave tests with increasing peak velocity

Sine Peak Velocity:	3in/s		6in/s		9in/s	
	μ	$\dot{u}$	μ	$\dot{u}$	μ	$\dot{u}$
Surface 1,2	0.034	1.5in/s	0.036	3in/s	0.040	4.5in/s
Surface 3	0.117	2.81in/s	0.118	5.63in/s	0.119	8.44in/s
Surface 4	0.127	1.5in/s	0.128	3in/s	0.128	4.5in/s

3.3.2 Temperature

The effect of temperature on a frictional surface is discussed in Rabinowicz (1995); in general, the friction coefficient decreases with increased temperatures. Mosqueda et al. (2004b) showed that the friction coefficients decrease with large velocities rather than maintain a plateau at μ_{max}. This was attributed to the higher temperatures at higher velocities. The tests were run so that peak cyclic velocity increased with the number of prior cycles, so these cycles would be expected to also have a higher temperature. The relationship of the shear strength to temperature is material specific and would need to be characterized for the bearing liner in order to fully understand the effect of temperature increase.

As with velocity dependence, the temperature dependence of the TFP bearing is surface specific. Based on the laws of thermodynamics, it would be expected that the temperature of the bearing liner would depend on the thermal properties of the liner material, the displacement path of the bearing surface, the load history on the bearing, and the geometry of the surrounding concave surfaces, liners and sliders. Because of this, it is expected to be very difficult to scale the results of reduced scale bearings to full sized prototypes, where the composite liners are very temperature sensitive.

Two controlled-displacement tests, using unidirectional sine wave motions with constant amplitude of 3.5 in and 0.5 in respectively with continuously increasing velocity, were carried out to see velocity effects on the bearings. The displacement and velocity for the sine wave of 3.5 in amplitude is shown in Figure 3.20. For the 3.5 in displacement motion, the value of H_3 can be measured, and for the 0.5 in displacements the value of H_1 can be measured. Instead of seeing an increase and plateau in the friction

coefficient with the increasing velocity as discussed above, a decrease in normalized hysteretic force was observed with increasing velocities (and increasing number of cycles prior to a measurement), as seen in Figure 3.21. This relationship is most likely due to the temperature increase in the bearing as the velocity and number of prior cycles increase. This is in agreement with the findings from Mosqueda et al. (2004b).

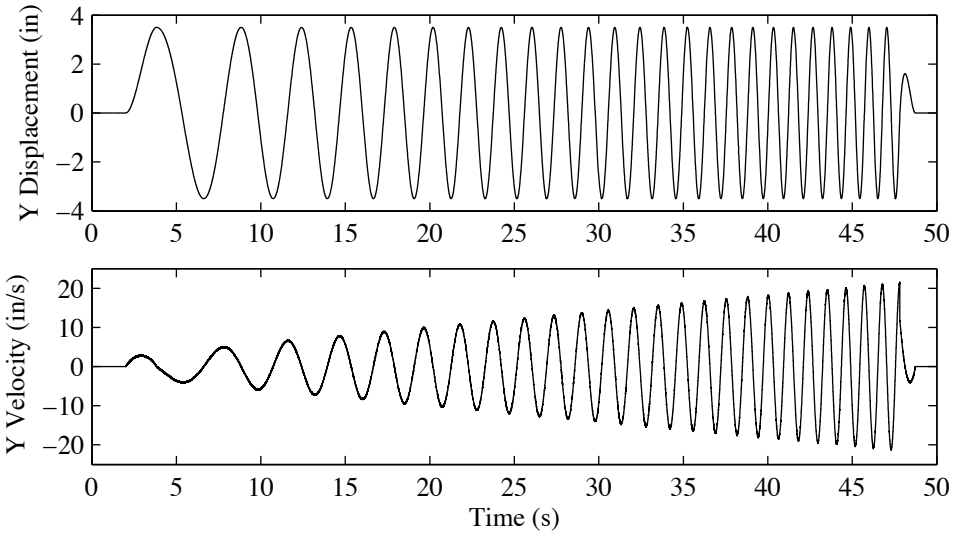

Figure 3.20 Displacement and velocity time history for the sine wave of amplitude 3.5 in with continually increasing velocity

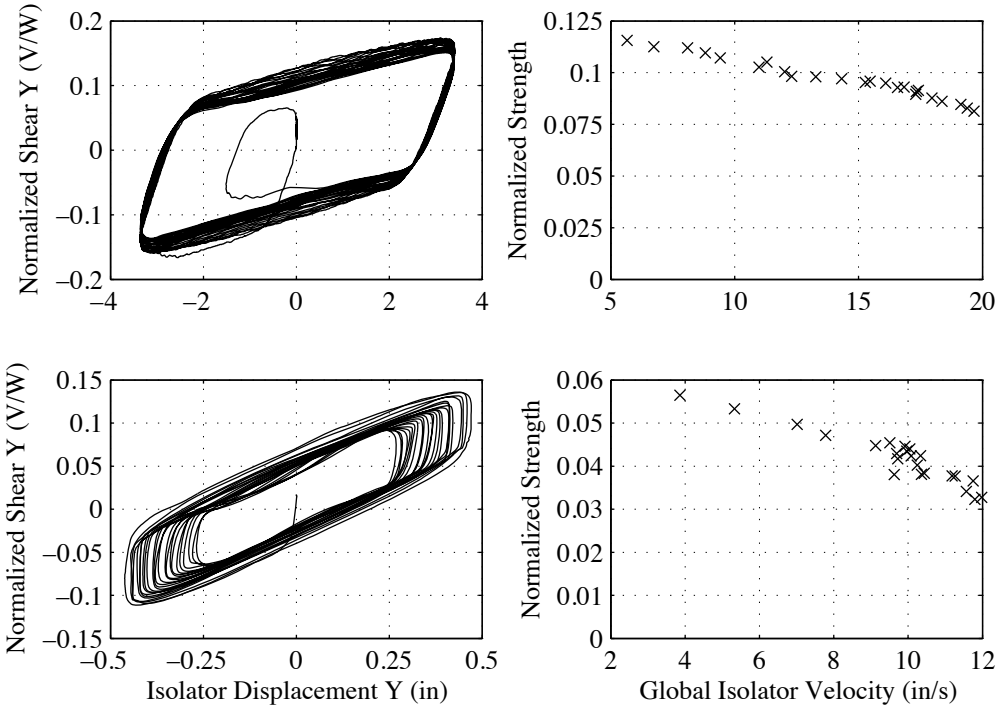

Figure 3.21 Normalized hysteretic force measured from sine waves of amplitude 3.5 in and 0.5 in with increasing velocity

Additional issues necessary for understanding the temperature effect on friction pendulum bearing behavior include calculating the change in temperature over the sliding surface with time. This issue is path dependent, as noted above. For example, a unidirectional excitation where cycles continually get bigger with each cycle will have the slider move over a cooler portion of the concave surface, whereas similar history where the displacements decrease in size will run the bearing over concave surfaces that already had been heated. Bidirectional movement of the bearing may thus exhibit different temperature characteristics than a bearing with unidirectional motion but with a similar amount of input energy. This will likely affect the shape of the hysteretic loops.

3.3.3 Pressure

During earthquake motions, overturning forces and vertical ground motion effects cause continual change in normal forces on each bearing. In TFP bearings the pressures on each sliding surface are different based on the contact surface area of the slider and the properties of the liner used on that slider. Additionally, pressures are not likely uniform due to external moments applied to the bearing. The effects of pressure are described in Constantinou et al. (1999). In general, friction coefficients decrease with an increase in pressure. The experimental setup used did not allow for the measurement or characterization of friction coefficient with respect to pressure. However, the pressures on all the surfaces can be easily calculated if uniform pressures on each surface are assumed. If pressure dependencies of the liners are known, they can easily be included in the TFP model.

4 Unrestrained Shake Table Experiments for Characterizing the Bidirectional Behavior of TFP Bearings

This chapter describes tests run to investigate the unrestrained dynamic response of a simple system isolated with TFP bearings to sine wave motions and a variety of earthquake excitations and to further validate the numerical model presented in Chapter 2. For these unrestrained tests, the struts between the rigid mass block and the reaction frames were removed from the earthquake simulator test setup described in Chapter 3. In addition, results are shown for cases where the mass blocks are offset to introduce a significant eccentricity between the static center of mass and geometric center of the supporting bearings.

Previous testing by Fenz and Constantinou (2008b) and Morgan (2008) has show stable behavior of the triple friction bearing (TFP) bearing under such dynamic loading. Further comments on the behavior and stability of the bearing under earthquake excitations are made in this chapter.

4.1 Earthquake and Other Excitations

A series of unidirectional sine wave motions were used during the tests to monitor possible change in of the bearing properties throughout the test program. Sine waves of ten cycles were varied in terms of their displacement amplitude and harmonic period, as shown in Appendix A. The lead and end tails of the sine wave motion were tailored so that the input motion began and ended with zero velocity.

Ground motion time histories were selected to match those used in bidirectional characterization testing done previously by Mosqueda et al. (2004a) for the single friction pendulum bearing. The ground motions used were selected from those developed in the SAC Steel Project to represent sever earthquake shaking in the western United States. The motions used are shown in Table 4.1.

The motions were modified for use on the shake table. The frequency characteristics of the motions were modified by filtering with a trapezoidal filter. The filter parameters are given in Table 4.2. The filter parameters were selected to limit high frequency command signals to a range that can be reliably reproduced by the shake table and to limit the peak ground velocities and displacements to ones within the shake table's capacity.

In addition, the length scale assumed to be associated with the reduced scale

isolators used in the tests was varied in the test program. Well-known similitude relations (Harris and Sabnis, 1999) indicate that for a length reduction scale factor of *SL*, to maintain the proper dynamic and inertial force characteristics for the model, it is necessary to scale time by $\sqrt{SL}$. In this manner, for the test set up used, accelerations and stresses in the model are the same as would be experienced in the full-scale structure, but in the model displacements are reduced by S*L* and velocities and periods are reduced by $\sqrt{SL}$.

Thus, by changing the assumed length scale, the model can represent TFP bearings having different dynamic properties. The tangent periods for the first three sliding phases of a typically designed TFP bearing are given by Morgan (2008). Considering the model bearings, used in this study with a length scale of 1, they become

$$T_1 = 2\pi\sqrt{\left(L_{1_0} + L_{2_0}\right)/g} = 0.72s$$

$$T_2 = 2\pi\sqrt{(L_{2_0} + L_{3_0})/g} = 2.03s \qquad (4.1)$$

$$T_3 = 2\pi\sqrt{(L_{3_0} + L_{4_0})/g} = 2.79s$$

These are smaller than typically used in building practice, as is the maximum bearing displacement. More realistic values can be simulated in the tests by assuming length scales varying from 2 to 5. Based on the discussion above, a length scale factor of 4 would necessitate scaling time by 2 and result in a prototype bearing with effective tangent periods twice those in Eq. 4.2 and a displacement capacity four times that of the model bearing. Since stress is preserved between the prototype and model, the measured bearing shear forces normalized by the applied axial load are similarly preserved, but measured displacements in the model correspond to values *SL* times larger in the full-scale prototype. The prototype bearing effective periods and displacement capacities are shown in Table 4.3 for length scales varying from 2 to 5.

Table 4.3 shows the effective displacement, velocity and acceleration capacity of the shake able for different length scale factors, as well as the time scale used for the command signal to achieve the specific length scale. Due to the dynamic characteristics of the ground motions selected, the records could not be run at full acceleration amplitude for smaller length scale factors without exceeding the displacement capacity of the bearings. Thus, the records were also scaled in amplitude, with smaller amplitudes used for cases with smaller length scale factors. The combinations of length and amplitude scale factors used for each ground motion were determined by simplified pre-test analyses, and are shown in Table 4.1. Table command signals used maintained the number of data points in the original command signal, however the time step was decreased by the appropriate time scale. The acceleration time histories and the pseudo acceleration response spectra of the input motions are shown in Figure 4.1 through Figure 4.4 with length scale 2 and the corresponding amplitude factor. A full list of tests is given in Appendix A.

Table 4.1 Selected earthquake ground motions

SAC ID	*Source Record*	*Length Scale, Amplitude Factor Combinations*
LA13/LA14	Newhall, 1994 Northridge	(2, 100%)
LA21/LA22	JMA, 1995 Kobe	(2, 65%), (3,100%), (4, 120%)
LS17C/LS18C	Sylmar, 1994 Northridge	(2, 44%), (3,70%), (4, 90%), (5, 115%)
NF01/NF02/NF0102v	1978 Tabas	(2, 50%), (3,65%), (4, 80%)

Table 4.2 Trapezoidal filter properties

Source Record	*Low Cut (Hz)*	*Low Corner (Hz)*	*High Cut (Hz)*	*High Corner (Hz)*
Newhall, 1994 Northridge	0.2	0.25	12	15
JMA, 1995 Kobe	0.05	0.1	12	15
Sylmar, 1994 Northridge	0.05	0.1	12	15
1978 Tabas	0.05	0.1	12	15

Table 4.3 Prototype values for multiple length scales

Length Scale	*Time Scale*	T_1 *(s)*	T_2 *(s)*	T_3 *(s)*	*Bearing Disp Capacity (in)*	*Max Table Disp (in)*	*Max Table Vel (in/s)*	*Max Table Accel (g)*
2	1.41	1.01	2.88	3.94	15.5	10	35.4	4
3	1.73	1.24	3.52	4.83	23.2	15	43.3	4
4	2	1.43	4.07	5.57	30.9	20	50.1	4
5	2.24	1.61	4.54	6.24	38.7	25	56.0	4

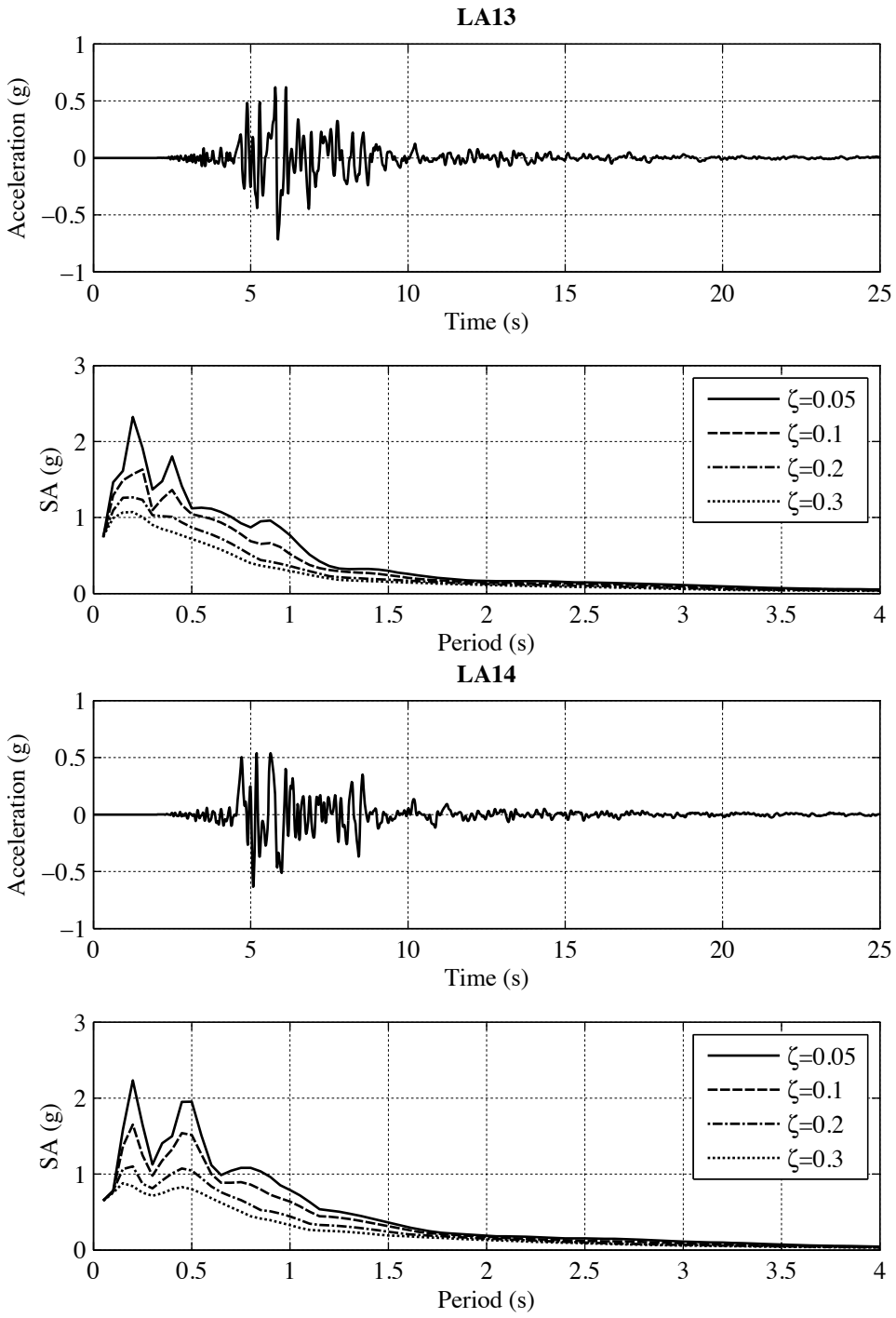

Figure 4.1 Northridge, Newhall input acceleration and response spectra, length scale 2 and amplitude factor 100%

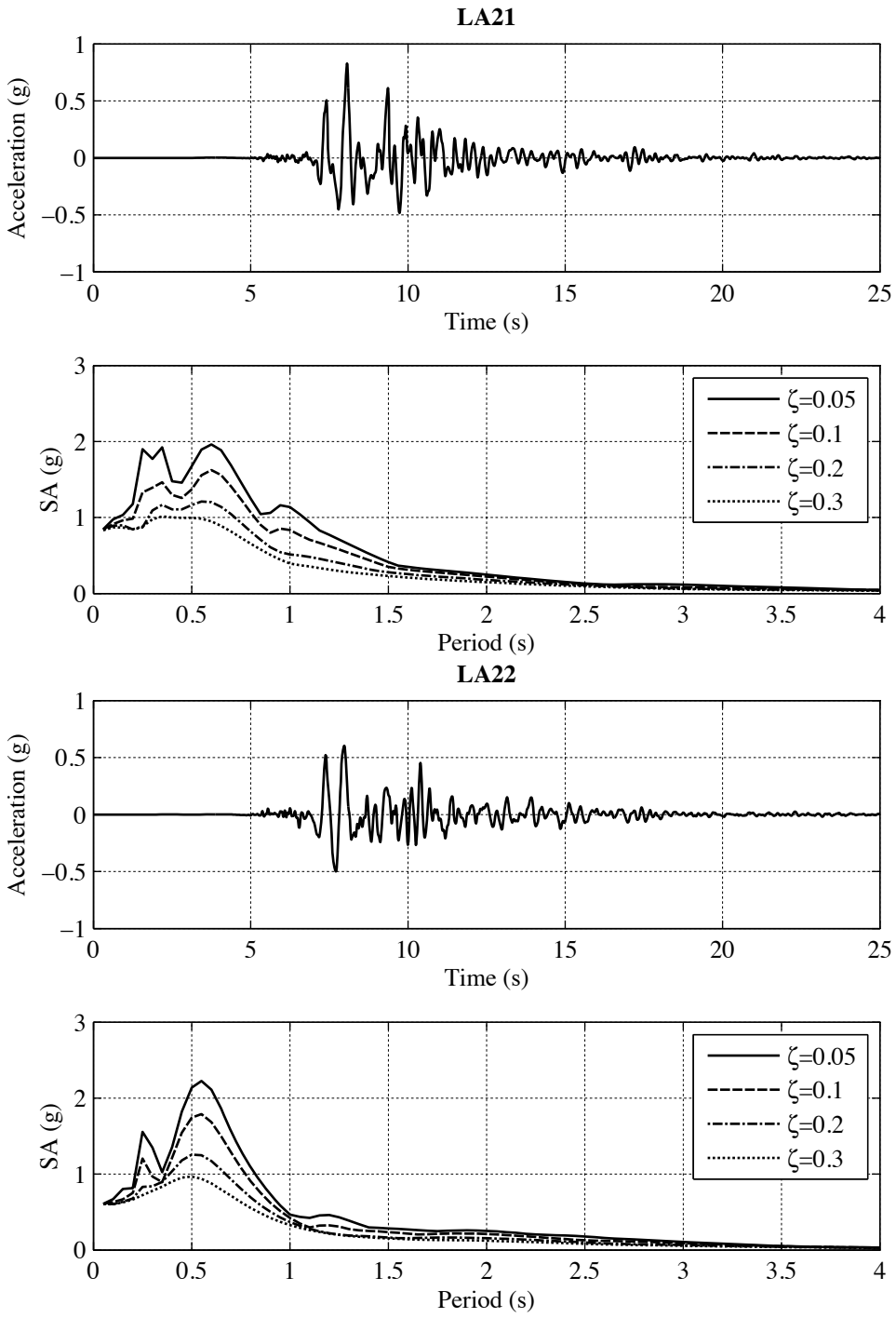

Figure 4.2 Kobe, JMA input acceleration and response spectra, length scale 2 and amplitude factor 65%

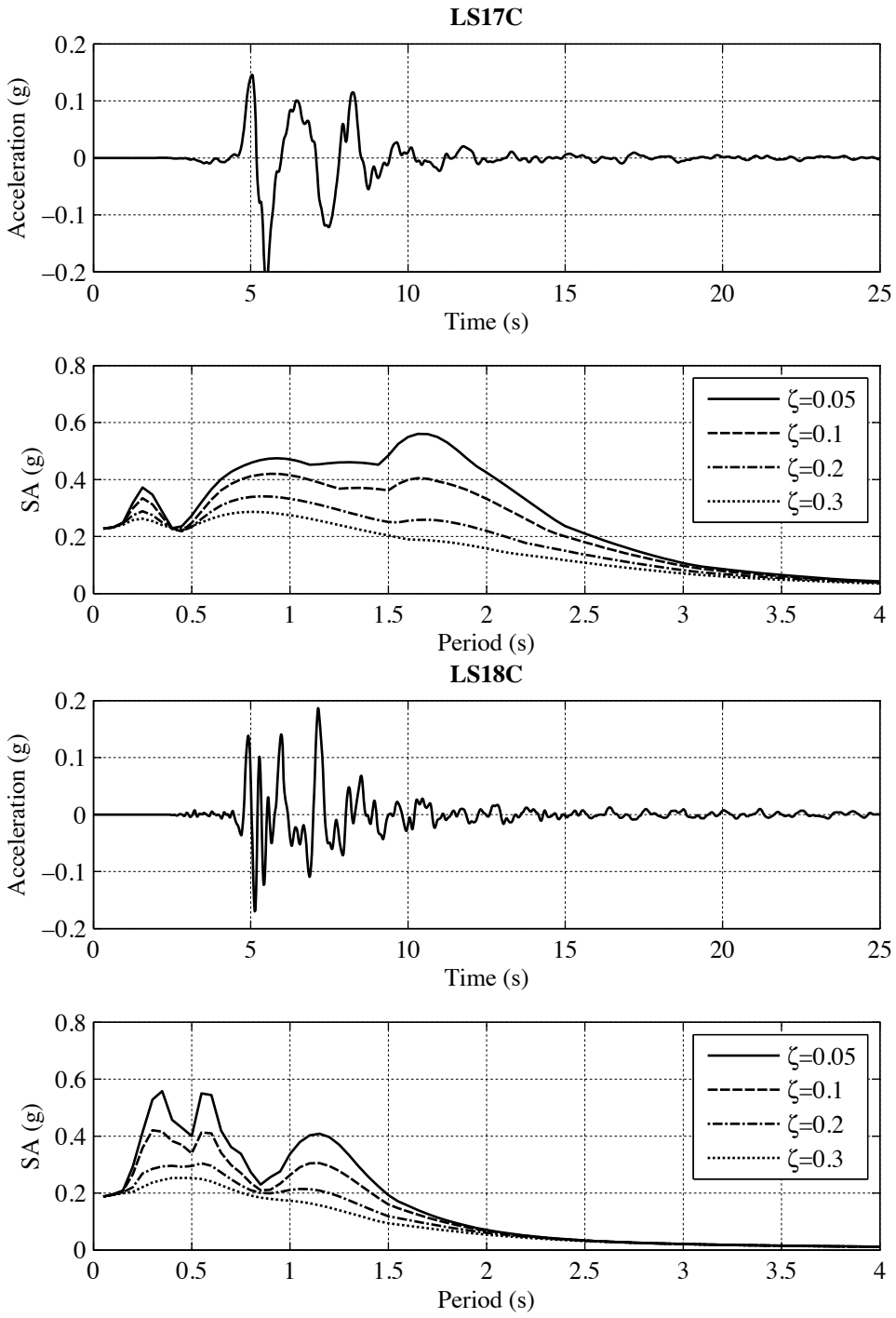

Figure 4.3 Northridge, Slymar input acceleration and response spectra, length scale 2 and amplitude factor 44%

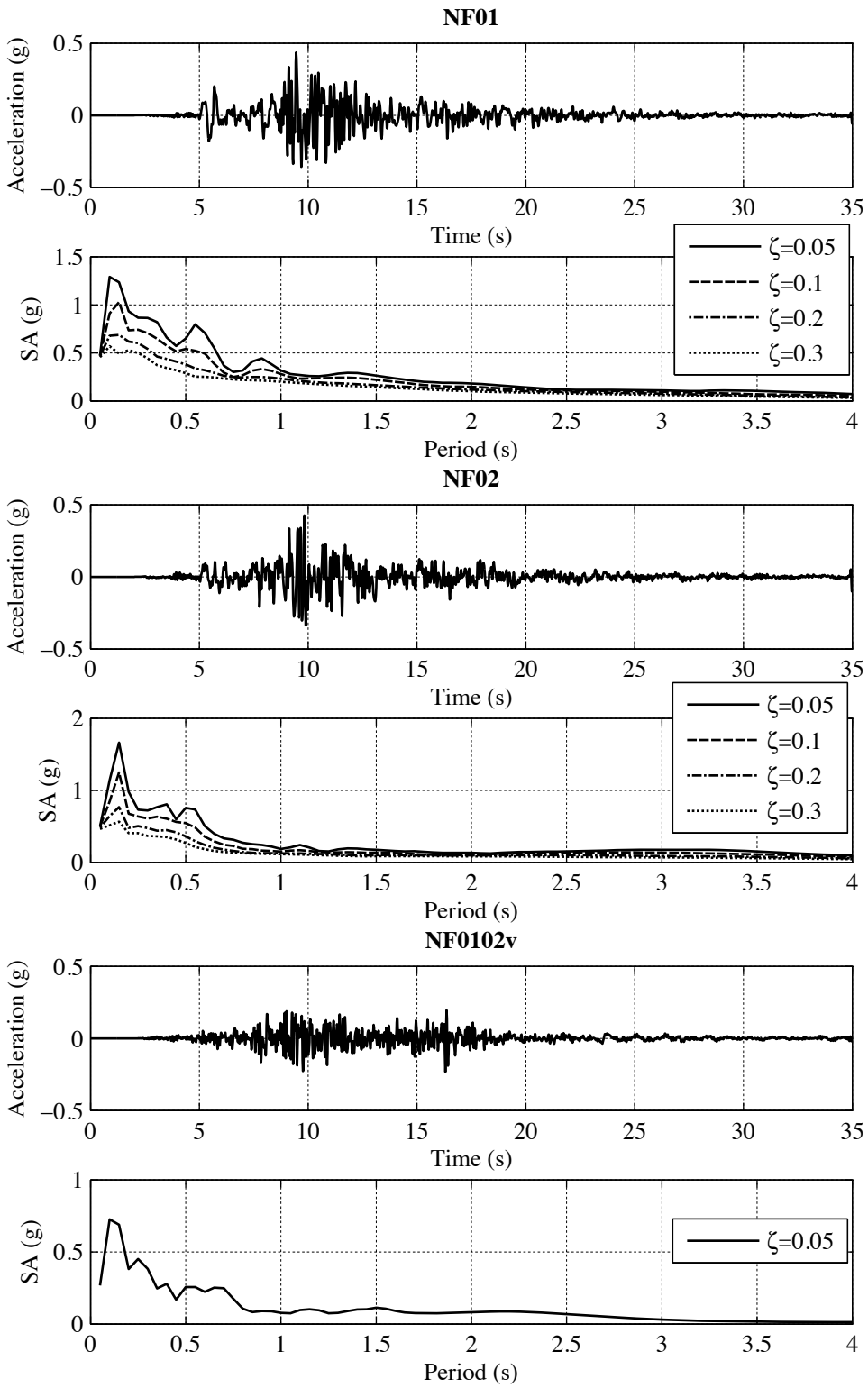

Figure 4.4 Tabas input acceleration and response spectra, length scale 2 and amplitude factor 50%

4.2 Comparison of Experimental and Numerical Results

The experimental test setup is identical to that described in Chapter 3, except that the struts used to hold the mass blocks stationary above the shake table were removed. This permitted the mass block to respond dynamically to earthquake and other dynamic excitations imposed by the shake table. The instrumentation and data acquisition system are also the same as previously described. For the experimental tests, the normalized base shear corresponds to the total horizontal shear in all four isolators in the reference direction divided by the axial load at each time step. The average displacement obtained from the two wire pots in each direction are used to obtain the *X* and *Y* displacements at the geometric center of the specimen.

The numerical model used in this section was identical to that used in Chapter 3, and the geometric parameters defining the TFP bearings were the retained. As the unrestrained input resulted in larger bearing velocities than imposed in the controlled-displacement motions, the friction coefficients found from the controlled-displacement unidirectional sine wave run with the largest peak velocity were used. These coefficients, taken from Table 3.2, are 0.04, 0.04, 0.119 and 0.128 for the four sliding surfaces respectively.

The symmetric tests specimen was idealized by a single bearing supported by the total load on all four bearings, and thus any effects of overturning moments of the rigid block mass on the axial loads acting in the bearings are neglected. As noted in Chapter 2, the TFP model was not developed to be able to simulate uplift. To avoid uplift in the tests, vertical accelerations were not input into the physical model in most cases. Consequently, the vertical motion of the mass block was not included in the numerical model. Because the horizontal stiffness of the TFP bearing is linearly related to axial load (friction coefficients are not pressure dependent), vertical accelerations are not expected to have a large effect on the horizontal displacements and normalized shear forces in the bearing, unless uplift occurs. The effect of the vertical component of excitation is discussed further in Section 4.3.2. However, as discussed in Section 4.3.5, the vertical motion of the bearings themselves, unintended vertical motion and bending distortions of the shake table platform and slight rotations of the specimen about the vertical axis result in differential axial loads in the bearings that are not accounted for in this simple numerical model of the test specimen. Another simplification in the numerical simulations was that the specimen and TFP bearing were assumed to have zero initial displacements at the beginning of each run. This does not match the initial conditions for experimental tests, where small global and local slider offsets are undoubtedly present. Because of the above assumptions, it is not expected that the numerical and experimental results will match precisely.

The TFP bearing exhibits hysteretic damping, and no additional viscous damping was added to the numerical model. Newmark's method with linear acceleration was used for the numerical integration. Each numerical analysis was run with the measured *X* and *Y* components of table acceleration applied simultaneously.

The basic dynamic behavior of the TFP bearings can seen in Figure 4.5 for a unidirectional sine wave input with period of 1 s at three levels of displacement. These

Table 4.4 Maximum absolute displacements, velocities and normalized shear force from experimental tests and numerical analysis for unidirectional sine wave input with period of 1 s

Input Amp (in)	*Disp Exp (in)*	*Disp Num (in)*	$\frac{D_{num}}{D_{exp}}$	*Vel Exp (in/s)*	*Vel Num (in/s)*	$\frac{V_{num}}{V_{exp}}$	*Force Exp*	*Force Num*	$\frac{F_{num}}{F_{exp}}$
2	2.79	2.89	1.04	21	18	0.86	0.18	0.16	0.89
3.5	6.06	5.18	0.85	33	29	0.88	0.20	0.18	0.90
5	Max	7.18	-	47	40	0.95	Impact	0.21	-

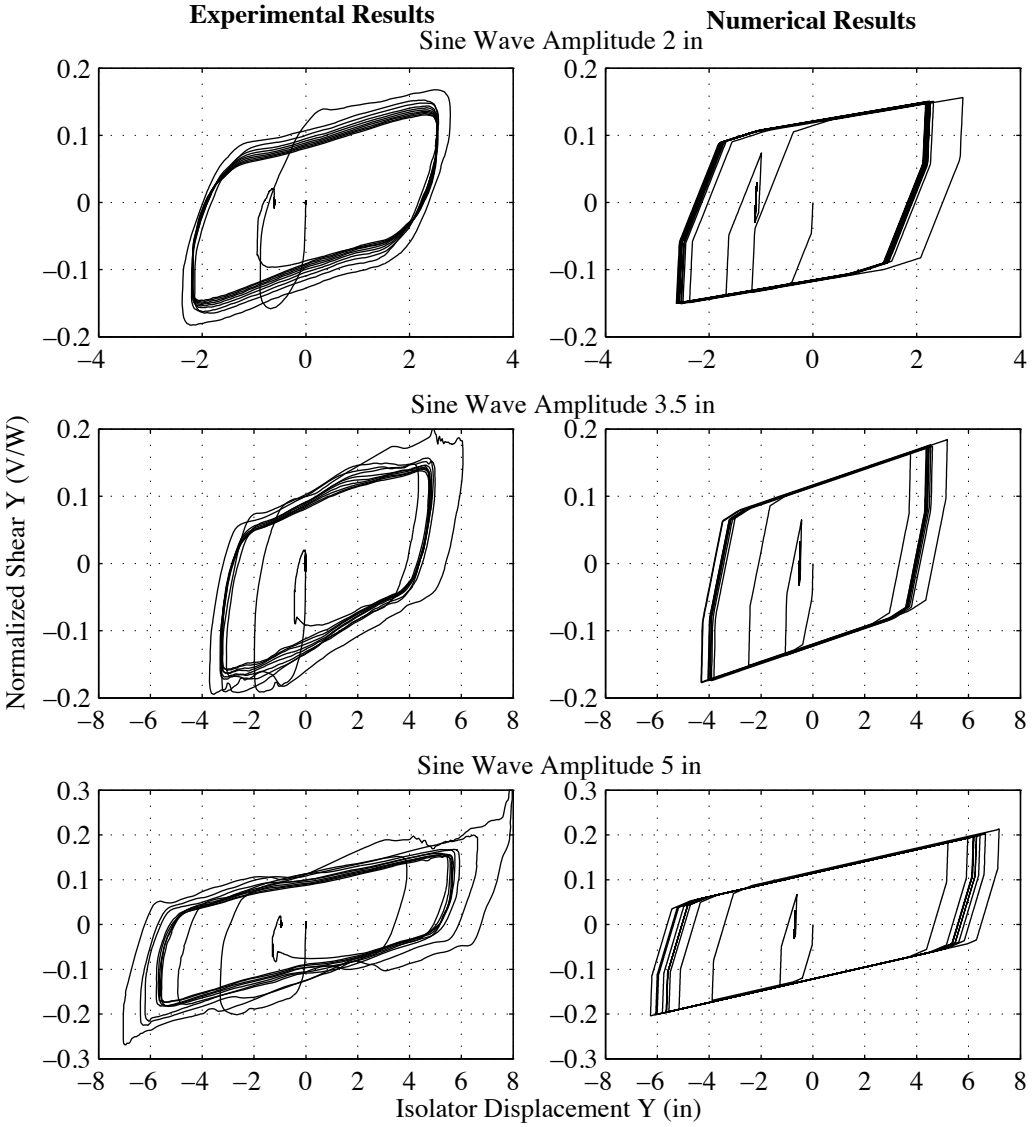

Figure 4.5 Experimental and numerical hystereses for unidirectional sine wave excitations with period 1s and varying displacement amplitude

results are similar to what was seen in Chapter 3. The general characteristics of the loops are similar for both experimental and numerical simulations. As mentioned previously, the closeness of the friction coefficients and dynamic effects appears to smooth the transition between the sliding stages described in Chapter 1. Table 4.4 compares experimentally and numerically derived maximum displacements, velocities and normalized shear forces for each sine wave amplitude. The results show that for the unidirectional sine wave motion, the numerical results tend to under-predict both displacements and shear force.

Experimental and numerical results obtained for the eleven test combinations presented in Table 4.1 are shown in Figure 4.6 through Figure 4.16 and the peak displacement, velocities and forces are compared in Table 4.5 through Table 4.7. Plots are shown for the normalized base shear in the *X* and *Y* directions, the displacement orbits in the *X*-*Y* plane, and the elastic response spectra in the *X* and *Y* directions for accelerations directly above the isolation plane. The displacements given are for the model scale, and need to be amplified by the length scale factor to correspond to prototype scale. The elastic floor response spectra for the X and Y directions are generated based on the accelerations recorded at the level of the frame above the isolators. The recorded acceleration histories were not filtered to remove noise in the signals before computing the response spectra.

It can be noticed from Figure 4.6 through Figure 4.16 that the hysteretic response under bidirectional earthquake loading is much more complex than observed in the unidirectional sine wave motion, and even than the behavior under the displacement-controlled excursions presented in Chapter 3. Most of the records have large amplitudes and little detail is discernible about the initial response on stages 1 and 2, other than during instances of unloading and reloading. For large displacement excursions, it is apparent that the bearings entered stages 4 and 5. In spite of the complex hysteretic bidirectional behavior exhibited by the bearings, the response of the isolated system during the tests achieved the purpose of isolation; limiting the forces transferred to the supported structure and developing large but stable displacements in the isolators. Comparison of the floor spectrum with the ground motion elastic spectra demonstrates the effectiveness in the isolators in reducing demands on the structure and its potential contents.

The numerical model shows similar behavior to the experimental results. The range of force listed in Table 4.7 is predicted in all events (with the exception of events were impact was predicted) within 15%. Peak velocity predictions, shown in Table 4.6, were also with in 15% for all but the Tabas source record runs. The predominant difference seen in all the excitations is that the numerical model consistently overestimates the displacements as shown in Table 4.5. Accordingly, the floor spectra from the numerical model are, in almost all cases, an upper bound of the spectra found from the acceleration data from the experimental tests. However, the floor spectra from the numerical model are quite a good match over most of the period range shown and give good estimates for design purposes. The floor spectra from the experimental results all have high values at low periods, this may be due to the high frequency electrical noise from instrumentation or increased high frequency input due to shake table characteristics.

For the Northridge, Sylmar ground motion with length scales 4 and 5 (Figure 4.12 and Figure 4.13) the numerical model predicts that the bearing reach their displacement

limits, while the experimental results came within half an inch of impact. As a result of the predicted impact, the floor response spectra from the numerical model have large pseudo acceleration values in the less than 0.5 s period range. Also note that, when the bearing reaches its ultimate restrainer limit, there are peaks in both the *X* and *Y* direction hystereses since the motion is bidirectional at that point. As the response had a predominant direction of the motion in the *X* direction, the *X* hysteresis is more classically shaped. However, the *Y* hysteresis shows a peak in force at an isolator displacement of 1in, which is the *Y* displacement at which the numerical model predicts that the bearing reaches its ultimate displacement.

Table 4.5 Maximum absolute displacement from experimental tests and numerical analysis

Source Record	*Length Scale*	*Amp Factor*	*Disp X Exp (in)*	*Disp X Num (in)*	$\frac{D_{Xnum}}{D_{X\,\mathrm{exp}}}$	*Disp Y Exp (in)*	*Disp Y Num (in)*	$\frac{D_{Ynum}}{D_{Y\,\mathrm{exp}}}$
Northridge, Newhall	2	100	2.88	3.21	1.11	3.76	5.31	1.41
Kobe, JMA	2	65	4.70	5.33	1.13	3.76	5.32	1.41
	3	100	5.22	5.24	1.00	5.20	6.42	1.23
	4	120	4.50	4.94	1.10	4.74	6.24	1.32
Northridge, Sylmar	2	44	2.99	4.70	1.57	1.17	1.83	1.56
	3	70	6.37	7.62	1.20	2.92	3.57	1.22
	4	90	7.03	Max	-	3.11	3.45	1.11
	5	115	7.37	Max	-	3.10	3.35	1.08
Tabas	2	50	2.43	3.41	1.40	1.17	1.79	1.53
	3	65	3.21	3.64	1.13	1.66	2.05	1.23
	4	80	3.34	4.05	1.21	1.96	2.18	1.11

Table 4.6 Maximum absolute velocities from experimental tests and numerical analysis

Source Record	*Length Scale*	*Amp Factor*	*Vel X Exp (in/s)*	*Vel X Num (in/s)*	$\frac{V_{Xnum}}{V_{X\,\mathrm{exp}}}$	*Vel Y Exp (in/s)*	*Vel Y Num (in/s)*	$\frac{V_{Ynum}}{V_{Y\,\mathrm{exp}}}$
Northridge, Newhall	2	100	22.6	22.8	1.01	22.2	19.9	0.90
Kobe, JMA	2	65	28.6	29.2	1.02	26.2	22.4	0.85
	3	100	33.0	36.6	1.11	28.2	30.5	1.08
	4	120	33.6	38.0	1.13	33.3	32.6	0.98
Northridge, Sylmar	2	44	12.3	14.4	1.17	9.7	10.5	1.08
	3	70	22.5	24.9	1.11	12.2	12.2	1.00
	4	90	26.7	29.0	1.09	14.7	13.3	0.90
	5	115	31.3	33.0	1.05	14.7	16.5	1.12
Tabas	2	50	10.7	11.6	1.08	13.0	8.9	0.68
	3	65	12.7	13.5	1.06	15.3	9.2	0.60
	4	80	15.0	16.1	1.07	17.1	11.0	0.64

Table 4.7 Maximum absolute normalized shear from experimental tests and numerical analysis

Source Record	*Length Scale*	*Amp Factor*	*Force X Exp*	*Force X Num*	$\frac{F_{Xnum}}{F_{X\,\exp}}$	*Force Y Exp*	*Force Y Num*	$\frac{F_{Ynum}}{F_{Y\,\exp}}$
Northridge, Newhall	2	100	0.17	0.16	0.94	0.21	0.18	0.86
Kobe, JMA	2	65	0.19	0.17	0.89	0.18	0.14	0.78
	3	100	0.20	0.22	1.10	0.17	0.17	1.00
	4	120	0.21	0.22	1.05	0.17	0.16	0.94
Northridge, Sylmar	2	44	0.18	0.18	1.00	0.11	0.12	1.09
	3	70	0.25	0.23	0.92	0.13	0.12	0.92
	4	90	0.26	Impact	-	0.12	Impact	-
	5	115	0.26	Impact	-	0.12	Impact	-
Tabas	2	50	0.17	0.15	0.88	0.13	0.13	1.00
	3	65	0.17	0.15	0.88	0.15	0.13	0.87
	4	80	0.17	0.15	0.88	0.16	0.13	0.81

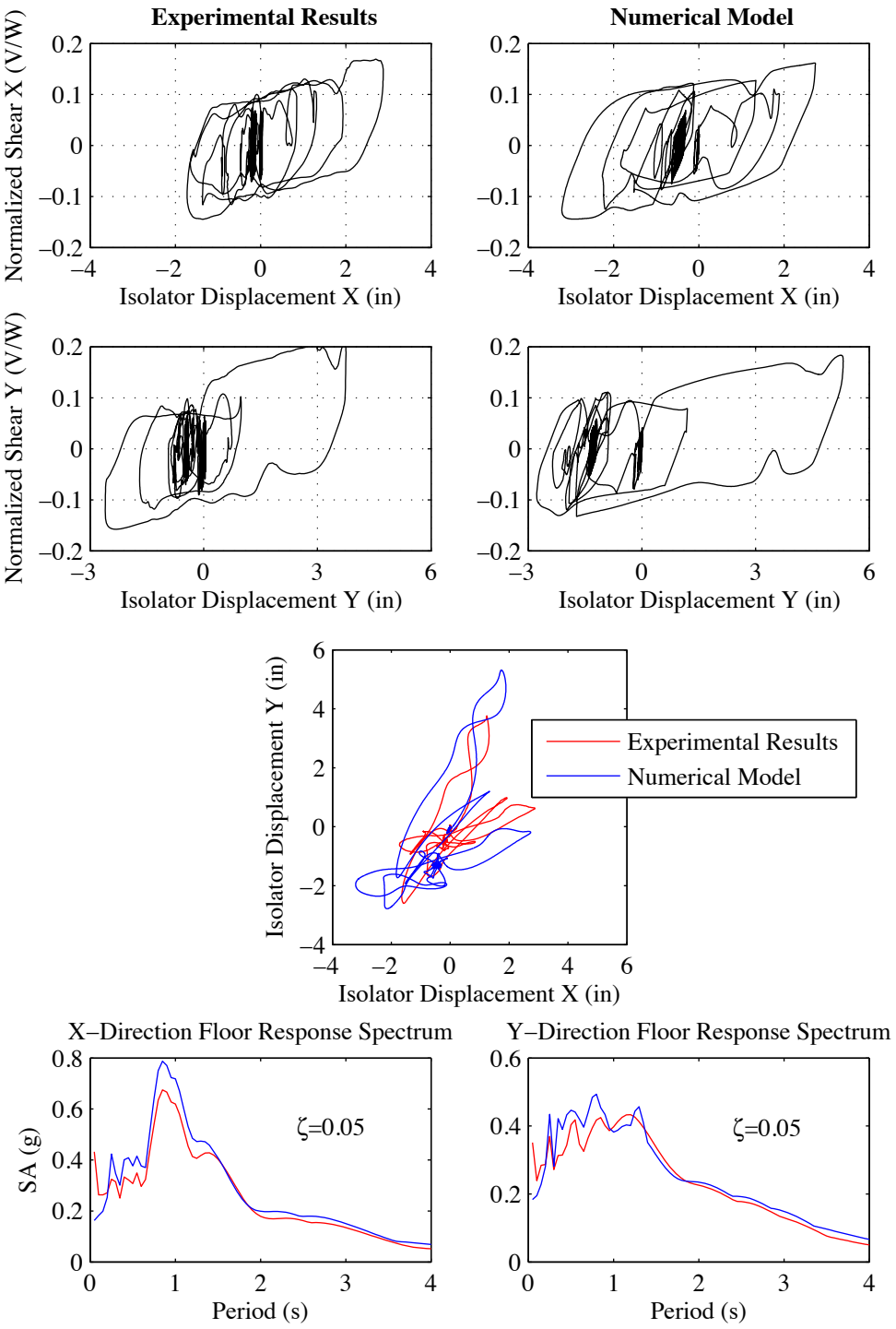

Figure 4.6 Experimental and numerical hystereses, displacements and floor response spectra from response to the Northridge earthquake Newhall record with length scale of 2 and 100% amplitude factor, with X and Y excitation.

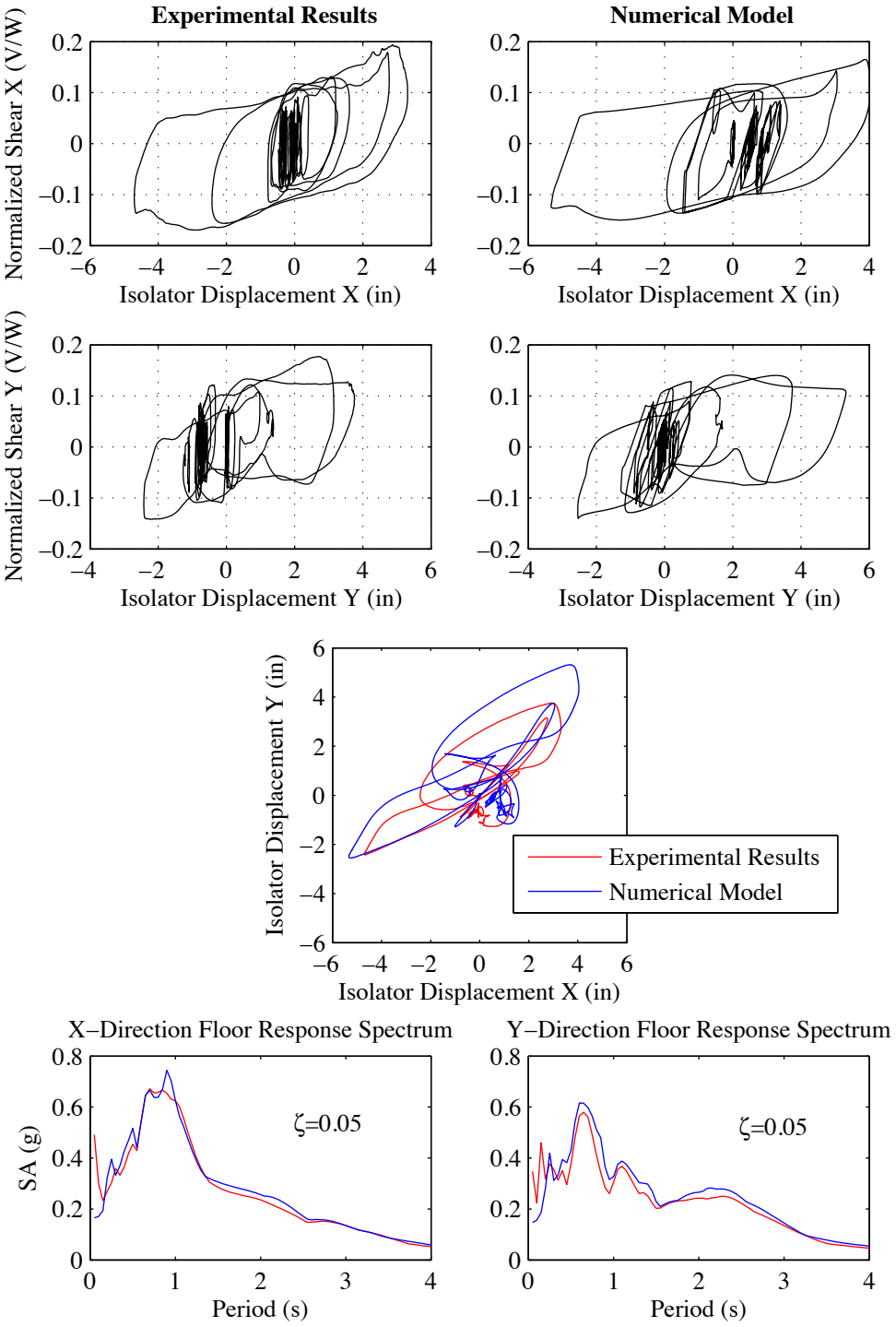

Figure 4.7 Experimental and numerical hystereses, displacements and floor response spectra from response to the Kobe earthquake JMA record with length scale of 2 and 65% amplitude factor, with X and Y excitation.

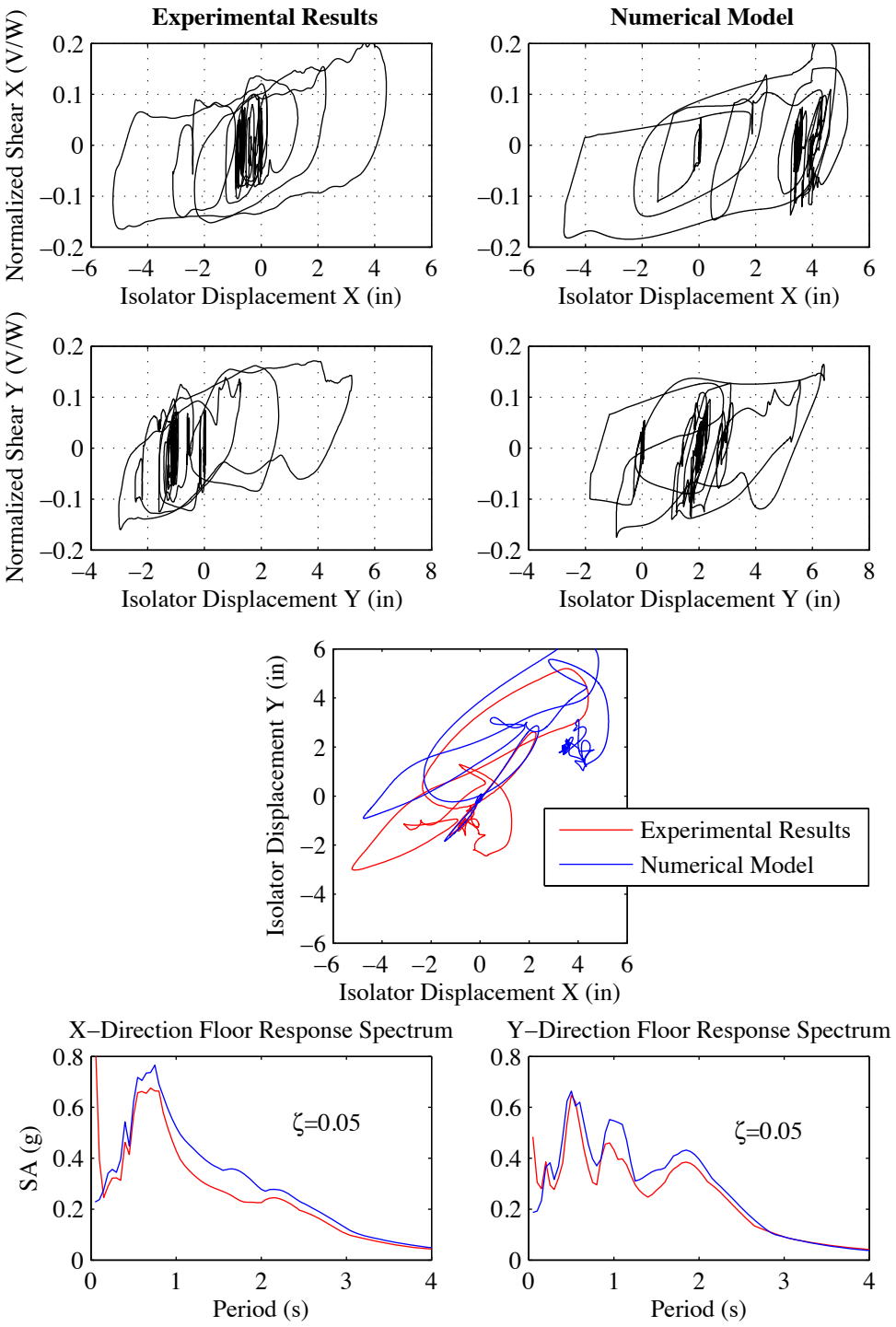

Figure 4.8 Experimental and numerical hystereses, displacements and floor response spectra from response to the Kobe earthquake JMA record with length scale of 3 and 100% amplitude factor, with X and Y excitation

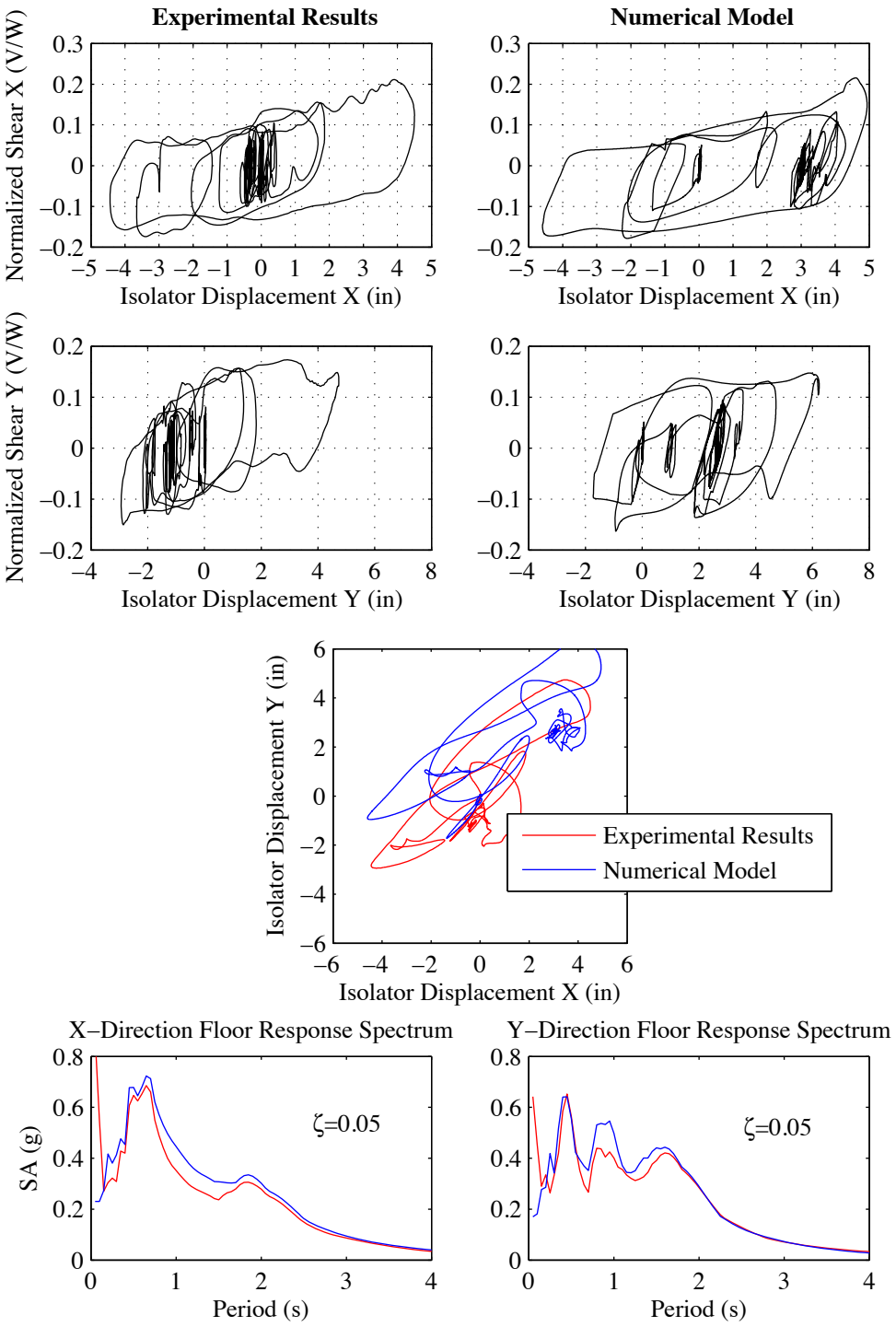

Figure 4.9 Experimental and numerical hystereses, displacements and floor response spectra from response to the Kobe earthquake JMA record with length scale of 4 and 120% amplitude factor, with X and Y excitation

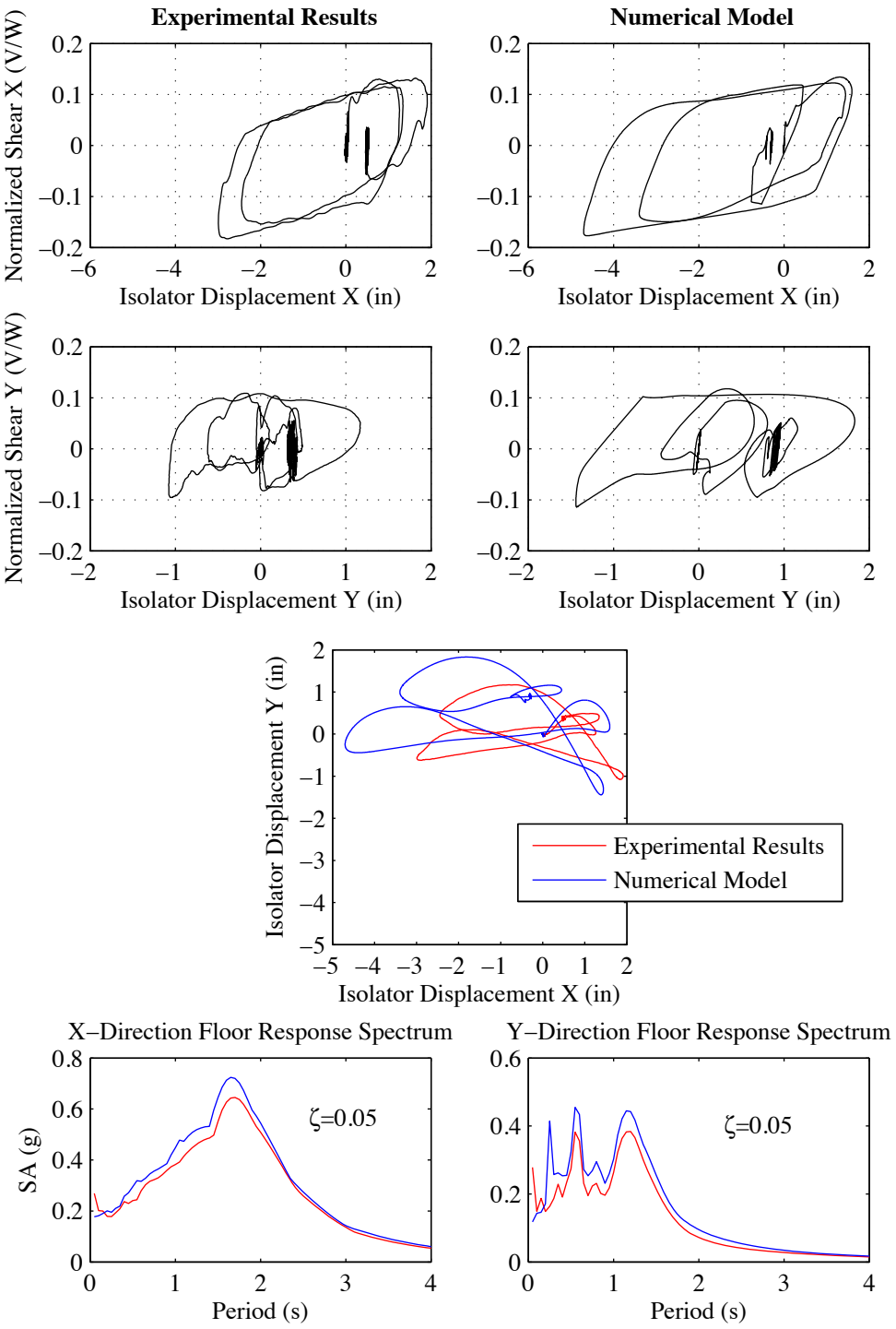

Figure 4.10 Experimental and numerical hystereses, displacements and floor response spectra from response to the Northridge earthquake Sylmar record with length scale of 2 and 44% amplitude factor, with X and Y excitation

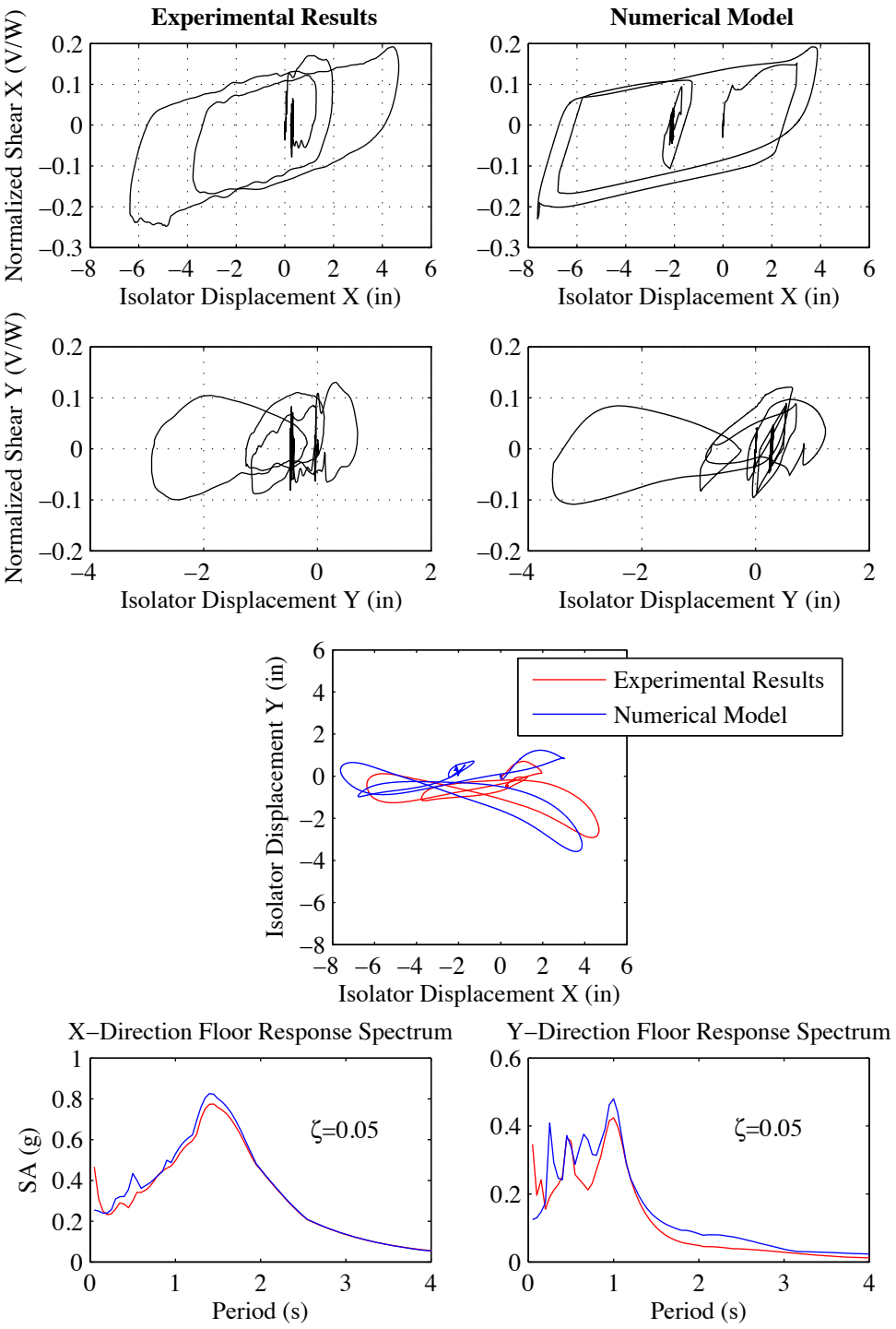

Figure 4.11 Experimental and numerical hystereses, displacements and floor response spectra from response to the Northridge earthquake Sylmar record with length scale of 3 and 70% amplitude factor, with X and Y excitation

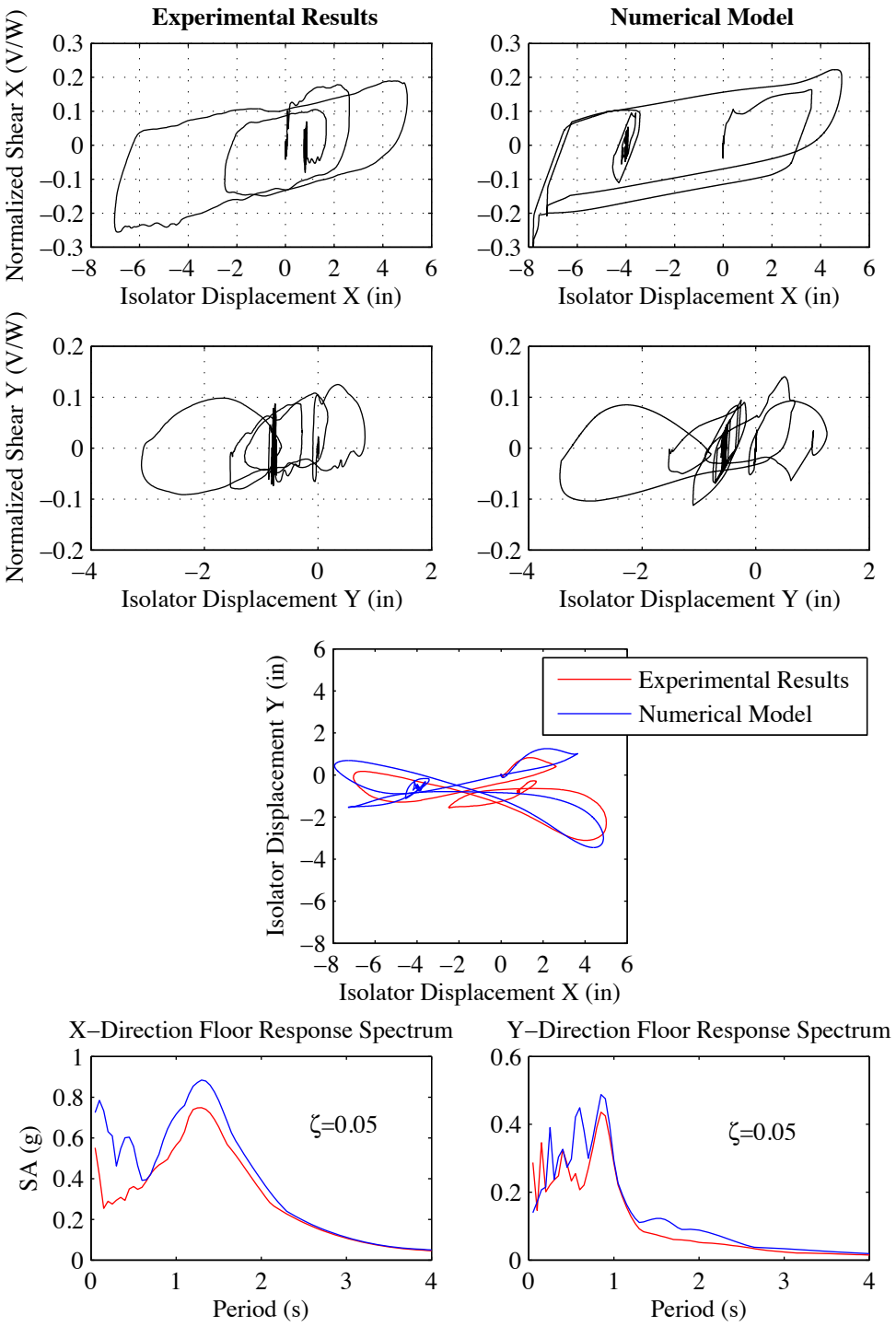

Figure 4.12 Experimental and numerical hystereses, displacements and floor response spectra from response to the Northridge earthquake Sylmar record with length scale of 4 and 90% amplitude factor, with X and Y excitation

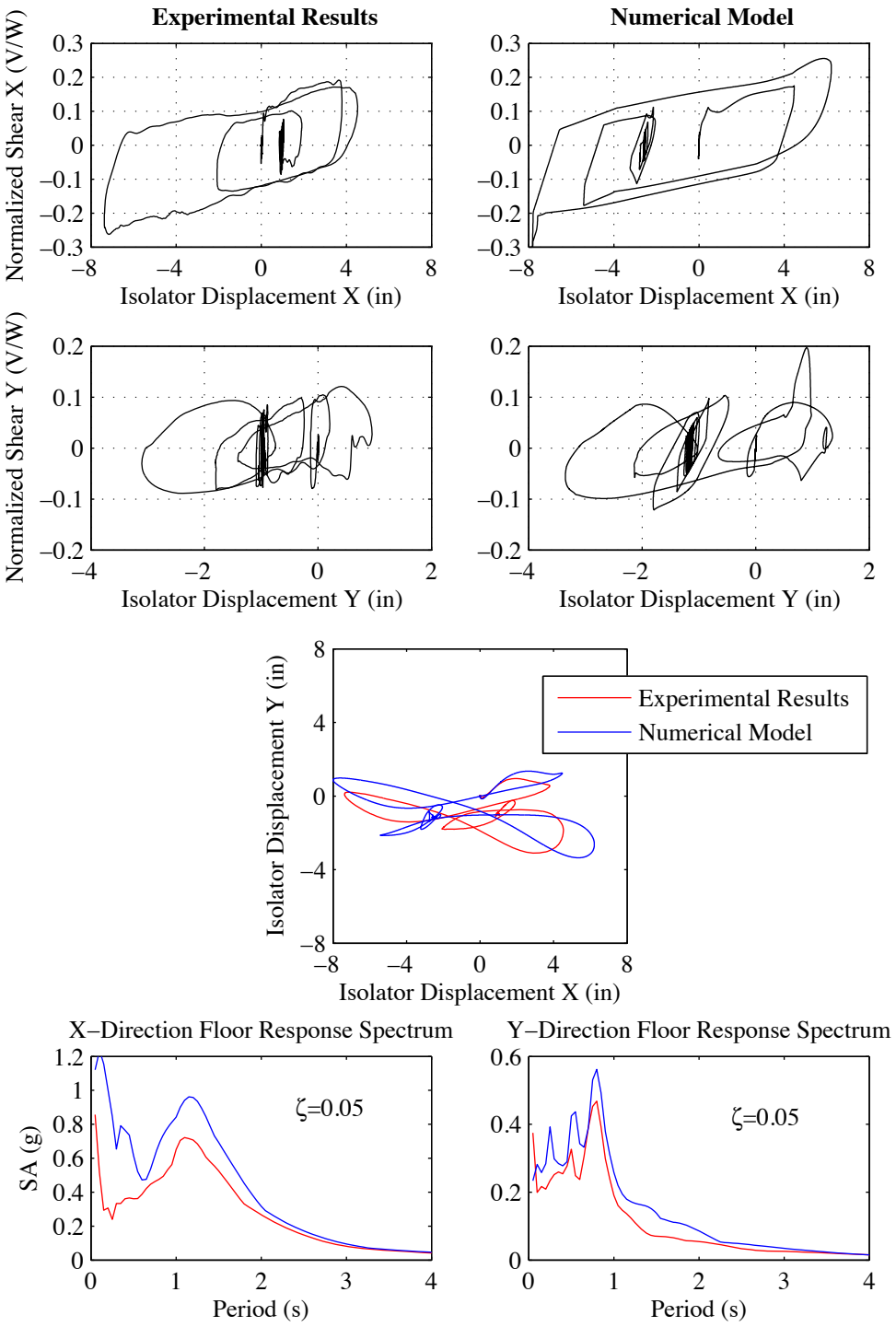

Figure 4.13 Experimental and numerical hystereses, displacements and floor response spectra from response to the Northridge earthquake Sylmar record with scale of 5 and 115% amplitude factor, with X and Y excitation

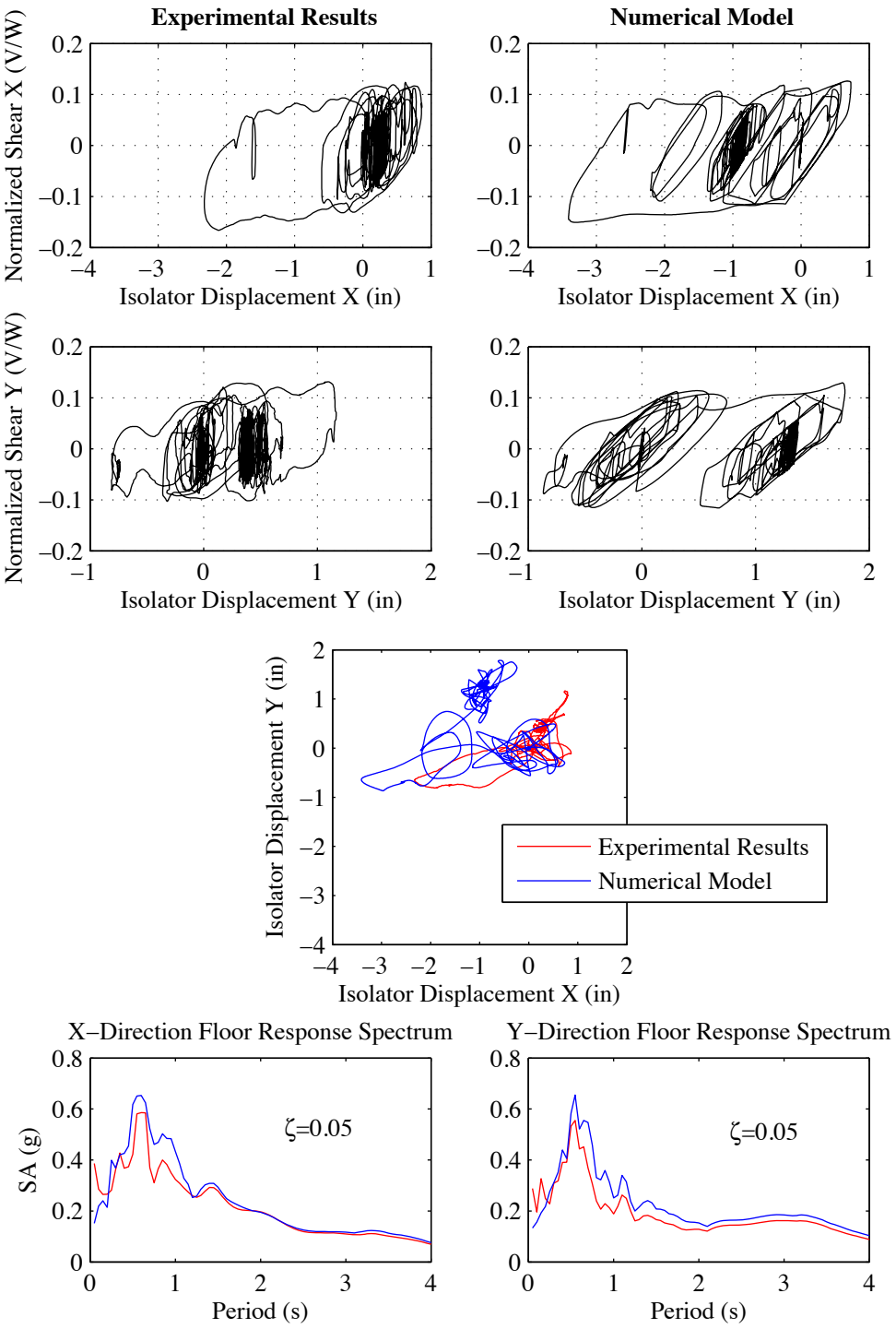

Figure 4.14 Experimental and numerical hystereses, displacements and floor response spectra from response to the Tabas earthquake record with length scale of 2 and 50% amplitude factor, with X and Y excitation

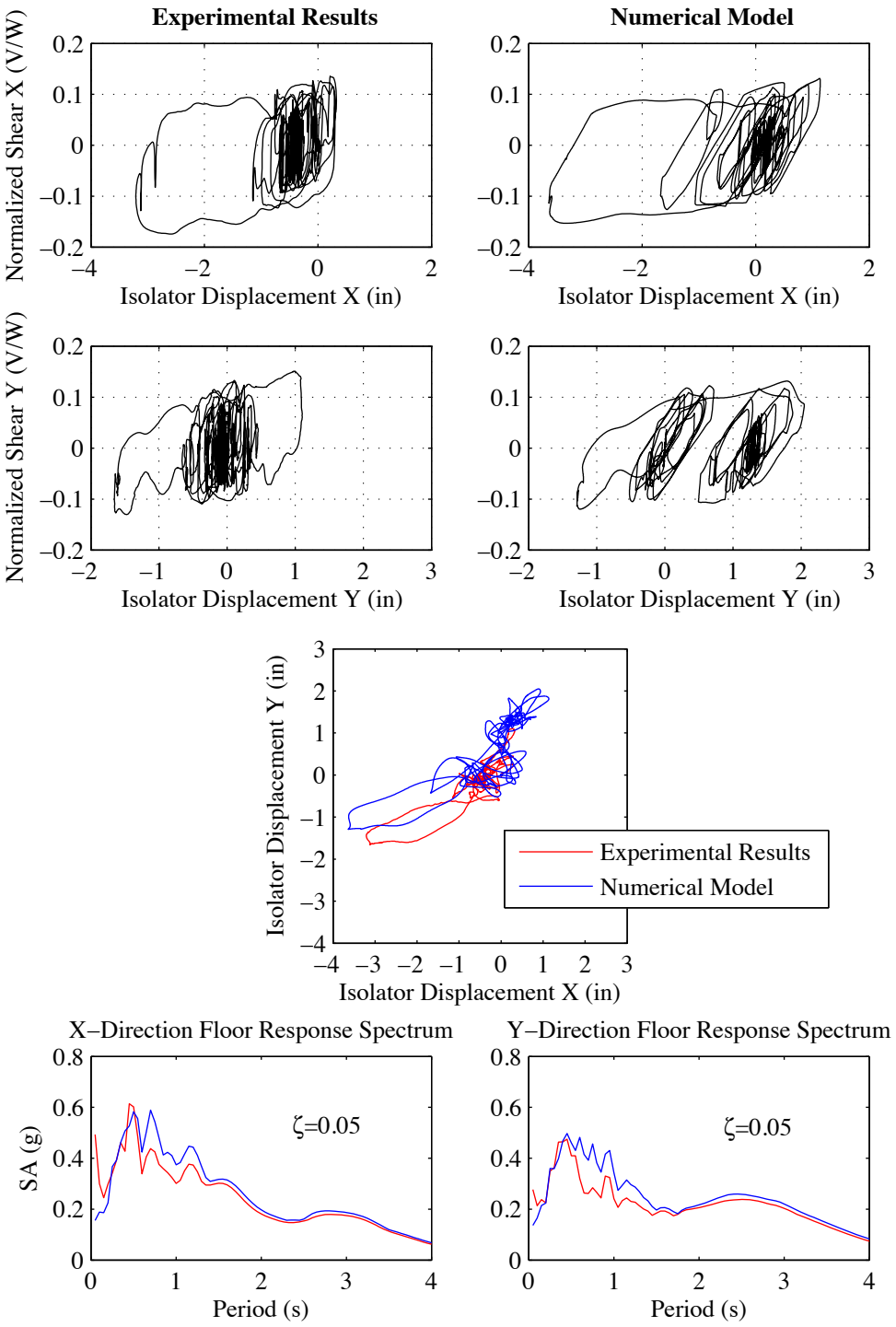

Figure 4.15 Experimental and numerical hystereses, displacements and floor response spectra from response to the Tabas earthquake record with length scale of 3 and 65% amplitude factor, with X and Y excitation

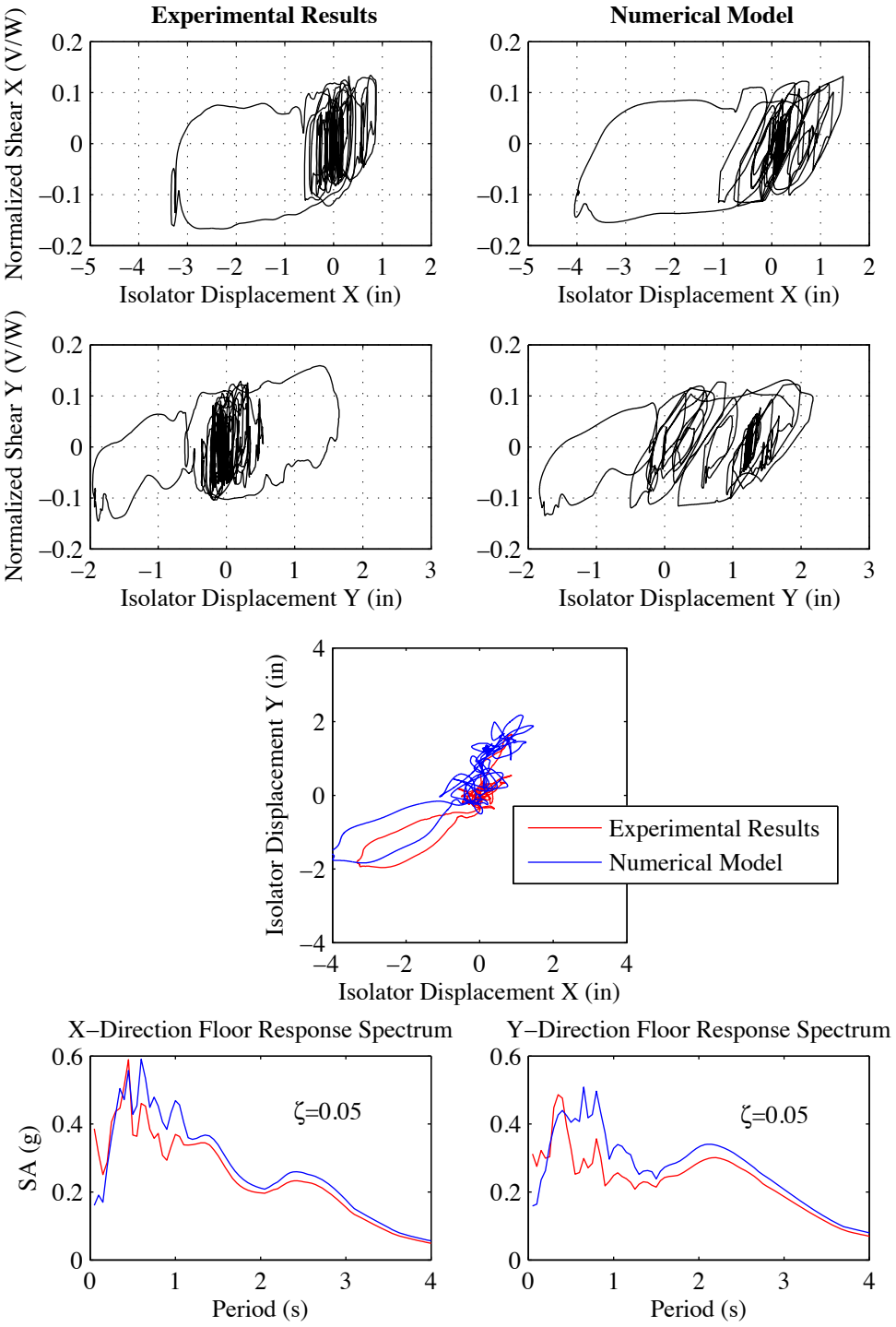

Figure 4.16 Experimental and numerical hystereses, displacements and floor response spectra from response to the Tabas earthquake record with length scale of 4 and 80% amplitude factor, with X and Y excitation

4.3 Other Aspects of Dynamic Behavior

Beyond validation of the numerical model, the unrestrained tests provided opportunity to understand the effects of testing conditions on the dynamic bearing behavior. In this section the effect of bidirectional earthquake excitation will be assessed by comparing to cases with only unidirectional excitation, and the effects of initial offsets, wear, and mass eccentricities will be examined.

4.3.1 Unidirectional vs bidirectional loading

The Tabas earthquake source motions with a 50% amplitude factor and a length scale factor of 2 was run with input in the *X* direction only and then with input in both the *X* and *Y* directions. Similarly, the Kobe earthquake motions at 65% acceleration scale factor and a length scale factor of 2 was run with input in the *X* direction only, in the *Y* direction only and then with input in both the *X* and *Y* directions. The comparison of the *X* direction responses to the Tabas motion is shown in Figure 4.17. The hysteretic behavior is quite similar for the uniaxial and bidirectional cases, with the bidirectional case exhibiting about 20% more displacement in the *X* direction under bidirectional

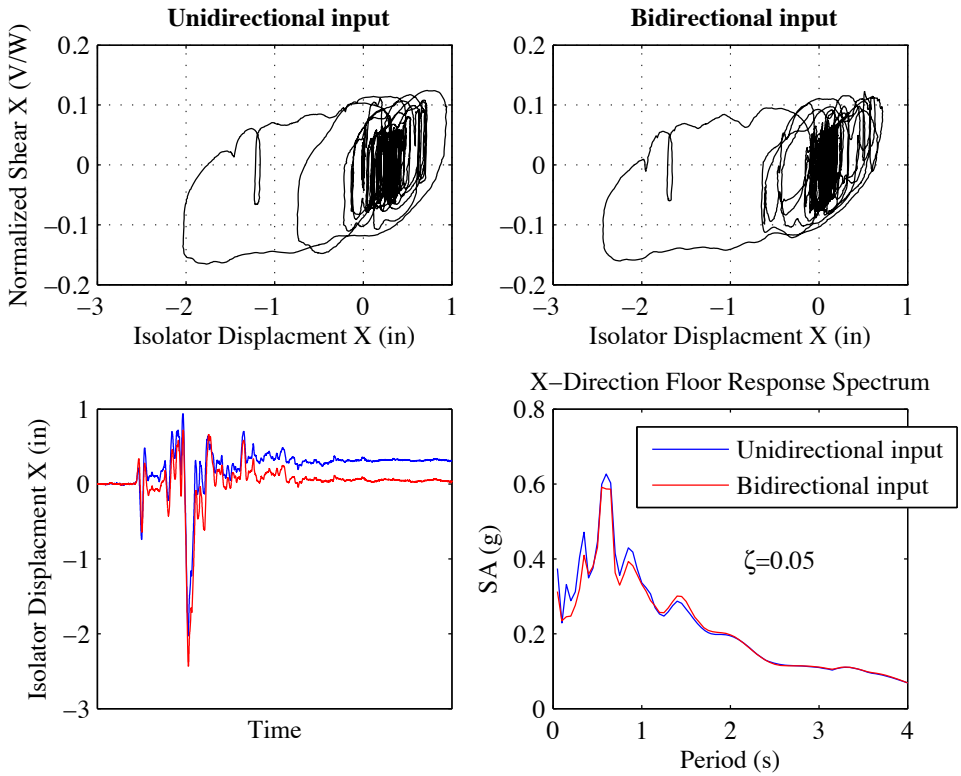

Figure 4.17 Comparison of X-direction hystereses, displacements and floor response spectrum from unidirectional input and bidirectional input for the Tabas source record with a length scale of 2, 50% amplitude factor

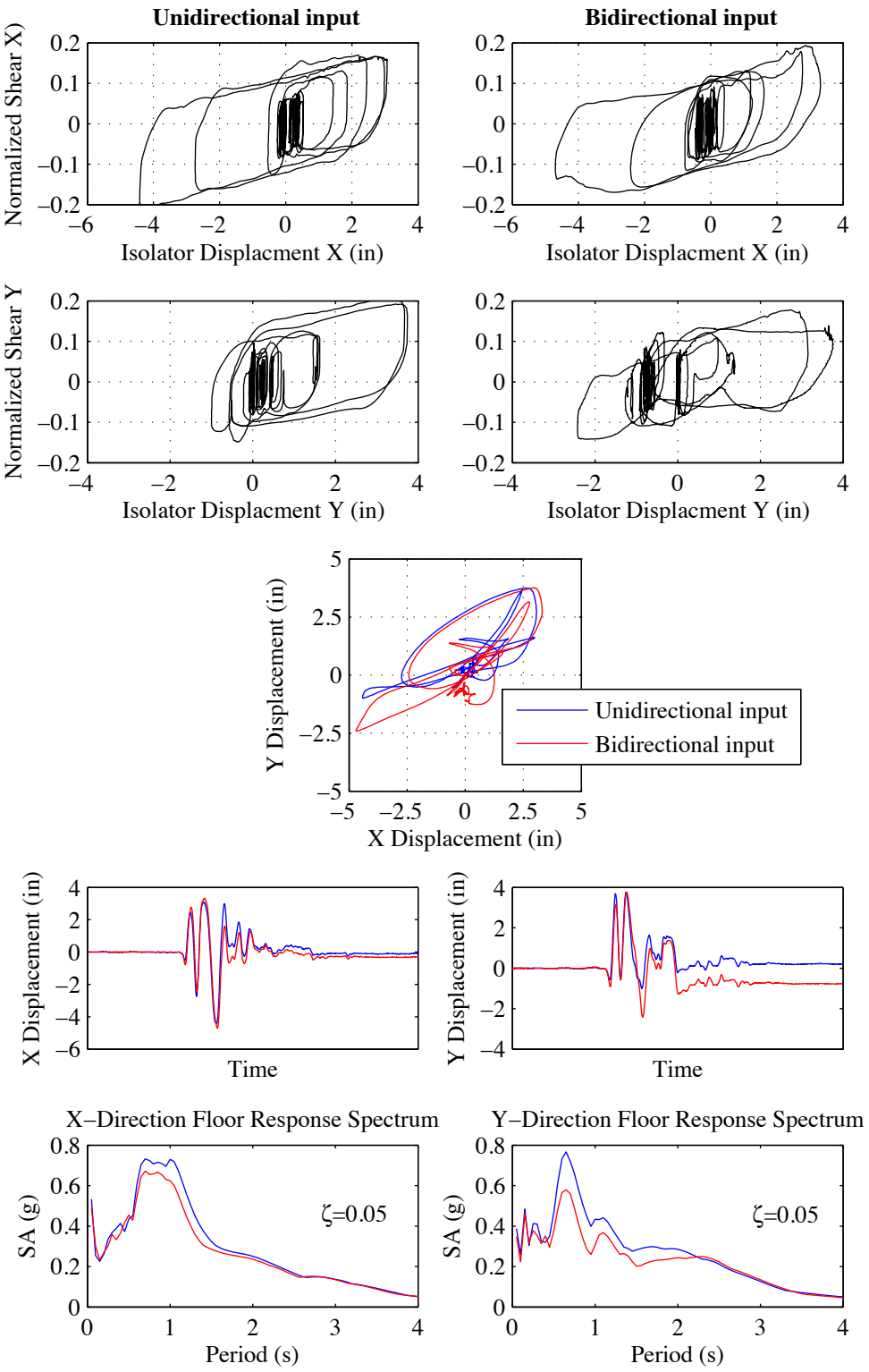

Figure 4.18 Comparison of hystereses, isolator displacement and floor response spectra from unidirectional input and bidirectional input for the Kobe source record with a length scale of 2, amplification factor of 65%

loading. However, the range of displacements is about the same for both unidirectional and bidirectional loading.

Comparison of both the *X* and *Y* responses to the Kobe motion is shown in Figure 4.18. The *X*-*Y* plane displacement orbit for the uni-directional input cases shown is made by plotting the unidirectional response in the *X* and *Y* displacements at the same time on the. This assumes that the responses are not coupled. As can be seen from the plots, there is not a strong coupling of the motions in the *X* and *Y* directions, but some does occur, resulting in slightly larger displacement excursions for the bidirectional case and different shape hysteretic loops. Interestingly, the floor spectra for the principal *X* and *Y* directions are slightly reduced due to bidirectional excitation.

The number of earthquakes compared herein is not large enough for a generalization; however, the unidirectional input behavior was, for these tests, a reasonable first-order approximation to the behavior under bidirectional input.

4.3.2 Inclusion of vertical ground motion input

The Tabas source record with amplification factor of 50% and length scale 2 was run with a two-component (*X* and *Y*) input and three-component (*X Y* and *Z*) input. A comparison of the TFP bearing hystereses for the runs is shown in Figure 4.19. Virtually no difference in the horizontal behavior can be seen between the two runs. As discussed before, if friction coefficients are not pressure dependent, the TFP bearing is linearly related to axial load, thus, bearing response is independent of axial load. Furthermore, this characteristic should make the bearing response resistant to fluctuating axial loads caused by vertical excitation. Again, observation from one source record is not sufficient to draw full conclusions; however, the results suggest that small vertical accelerations, that do not cause uplift, do not have large effects on horizontal TFP bearing behavior.

4.3.3 Initial bearing offsets

One of the results of a bearing with hysteretic behavior is that the bearing does not always return to zero displacement after loading. Although there is a positive restoring force due to the curvature of the sliding surfaces, the friction force may keeps the bearing offset from the origin. As noted previously, even if the global deformation is zero, the there may be internal deformations on the sliding surfaces that sum to zero because each sliding surface has its own hysteretic characterization. It is of interest to see if the initial offsets of bearings cause a difference in the overall bearing behavior.

The Tabas source record with amplification factor of 50% and length scale 2 was run twice, once with the bearings uncentered prior to the test and once with the bearings centered. In recentered case, the bearings were globally recentered by imposing a series of small pulses on the shake table. Similar recentering behavior could be expected due to aftershocks. In the uncentered case, the initial global offsets were on the order of half an inch. The force-displacement hystereses for both tests are shown in Figure 4.20. From the hystereses, it is shown that the initial bearing position can shift the displacement of the response. However, the shape of the bearing response and the bounds on the shear force remain essentially the same. As the accelerations transmitted through the isolation layer are of first concern to the building behavior, the initial global offset of the bearings on

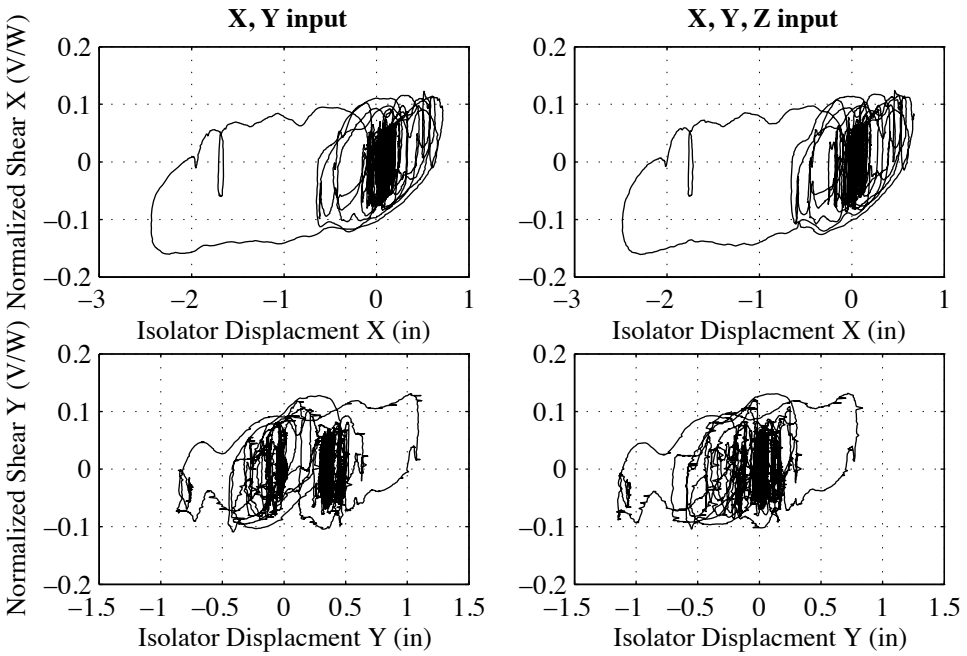

Figure 4.19 Comparison of hystereses from two component (*X* and *Y*) input and three component (*X Y* and *Z*) input for the Tabas source record with a length scale of 2, 50% amplitude factor

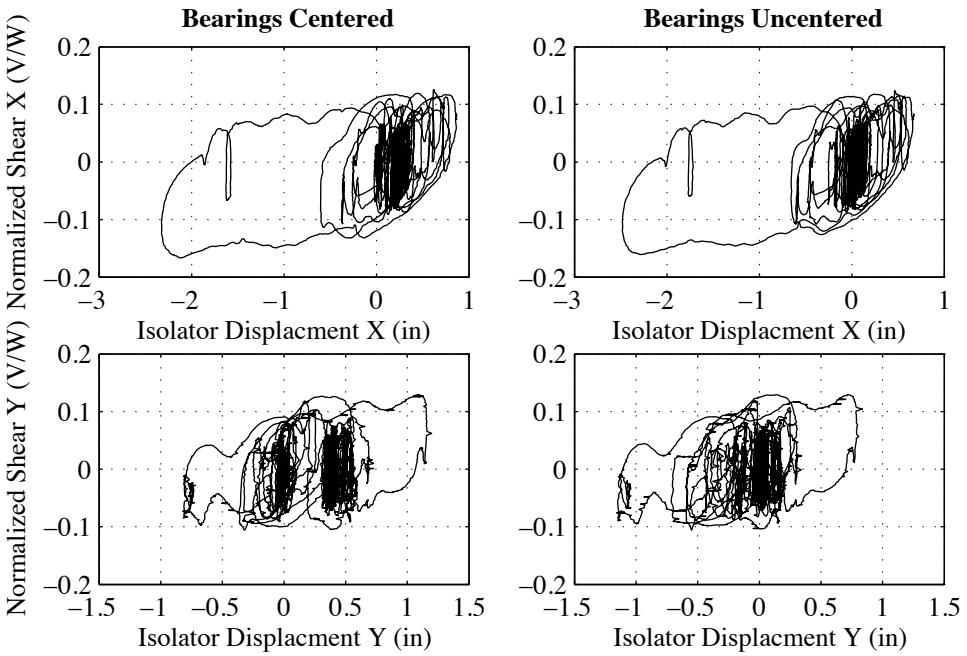

Figure 4.20 Experimental hystereses with bearings centered and uncentered before excitation for the Tabas earthquake record with 50% amplitude factor and length scale of 2, with X, Y and Z excitation

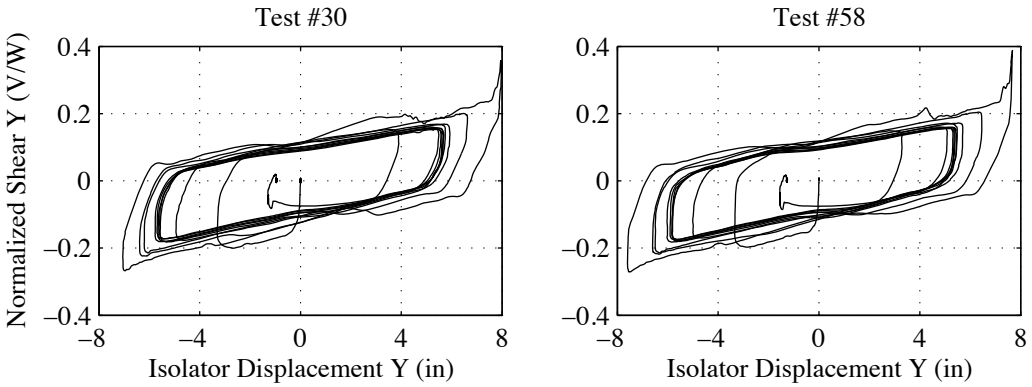

Figure 4.21 Hystereses for unidirectional sine wave of period 1s and amplitude 5 in, two different tests

this scale prove unimportant to the behavior of the superstructure. Global offsets may make a difference with regards to maximum displacements and behavior of the bearing as the ultimate displacement is approached.

This observation regarding bearing forces is in agreement with the findings from the displacement-controlled tests, in which the initial global displacements were zero, yet initial local slider displacements were non-zero. The only effect from offset initial local slider displacements was seen in the offset sine wave motion, shown in Figure 3.18, when the bearing came within an inch of its displacement capacity.

4.3.4 Behavior over many excitations

The same bearings used in the controlled-displacement motions were used in the dynamic motions; a total of 58 tests were run on the same set of sliders in the bearings. A sine wave of amplitude 5 in and period of 1 s was run with the unrestrained setup before the earthquake ground motions were run and then again after they were completed (see Appendix A). Twenty-seven ground motion tests were run on the bearings between the identical sine wave motions. The hystereses loops for the two sinusoidal tests are shown in Figure 4.21. The hystereses loops are almost identical. Both loops show the inner restrainer contact of the TFP bearing occurring at the same displacement and have the same force range. The similarity shows the repeatability of the behavior even after significant use of these reduced scale bearing. As noted in Chapter 2, many aspects of behavior associated with temperature, pressure and velocity may change by altering the length scale. As such, this lack of deterioration following many exposures to severe earthquake excitations should be verified for actual projects using full-scale prototypes exposed to realistic loading protocols.

4.3.5 Shift in center of mass

Earlier studies have been conducted to assess the effects of mass eccentricities on the behavior of single pendulum friction isolators (Zayas et al., 1987; Zayas et al., 1989; Anderson, 2003) Because the center of mass for these coincides with the center of lateral stiffness of the bearings, the response of rigid bodies tends to have little torsional response about a vertical axis.

To examine the effects of shifting the center of mass on a TFP isolated structure, M. Mieler, E. Keldrauk and B. Stojadinovic (personal communication, 2011) conducted experiments with the same setup as discussed above for the unrestrained shake table tests. However, in these tests the concrete mass blocks were restacked between earthquake runs to shift the location of the center of mass. As explained in Chapter 3, four concrete blocks were stacked on top of the TFP isolators. In their tests, Mieler, Keldrauk and Stojadovic used seven different three-component earthquake records. The records used and the peak ground displacements they were run at are listed in Table 4.8. Each record was run with three mass block configurations. In one case no blocks were offset (the baseline case considered previous to this sub-section), and in the other two cases, two blocks were offset and three blocks were offset by 3 feet in the positive *Y* (East, referring to Figure 3.1) direction. The setup with three offset blocks is shown in Figure 4.22. The shift in the center of mass with *n* blocks offset (out of *N* total) is equal to

$$\Delta\text{CoM}=\frac{nM\delta}{NM} \tag{4.2}$$

where δ is the displacement offset of the blocks and *M* is the mass of each block assumed to be the same for all blocks. The blocks weighed roughly 16.9 kips each. The steel support frame has a small mass (approximately 1 kip) compared to the blocks and is ignored in the discussion below. The shift of the center of mass with respect to the geometric center of the isolator bearings is 0, 17% and 25% of the longest length between the bearings for the three setups.

To understand the effect of the shift in center of mass, the effect on the eccentricity of the system needs to be examined. The eccentricity is defined as the distance between the center of mass and the center of rigidity. However, in friction pendulum isolators, the horizontal stiffness of the bearings is directly dependent on the axial load, thus a shift in center of mass leads to a shift in center of rigidity. From statics, the axial force on the isolators on the East and West side of the specimen is

$$\begin{aligned} A_{East} &= \frac{1}{2}\frac{NW\,d/2 + nW\delta}{d} \\ A_{West} &= \frac{1}{2}\frac{NW\,d/2 - nW\delta}{d} \end{aligned} \tag{4.3}$$

respectively, where *W* is the weight of each block and *d* is the distance between the isolators in the *Y* direction, which for the setup was 9 ft. The stiffness of the bearings is represented as the normalized backbone stiffness *k* multiplied by the axial load on the bearing. Ignoring the effects of different pressures acting on the bearings, all four isolators have the same theoretical normalized backbone behavior. When three of the four concrete blocks are shifted 3 ft, approximately 75% of he total weight is supported by the two Eastern bearings. The shift in the center of rigidity can be found as

$$\Delta CoR = \frac{A_{East}k*\left(d/2\right) + A_{West}k*\left(-d/2\right)}{A_{East}k + A_{West}k} \tag{4.4}$$

Plugging in Eq 4.3, this reduces to

$$\Delta \text{CoR} = \frac{nW\delta}{NW} \tag{4.5}$$

which is equal to the shift in the center of mass in Eq 4.2. The eccentricity is defined as the distance between the center of mass and the center of rigidity

$$e = \Delta CoM - \Delta CoR \tag{4.6}$$

Thus, offsetting the mass does not result in any eccentricity. The same argument can be done for all stages of TFP behavior so long as each bearing is on the same stage and axial loads are distributed according to static gravity considerations for the offset position.

Thus, torsional response is only expected (1) when bearings are on different stages of behavior (have different *k* values) or (2) when the bearing loads are not distributed according to the static equilibrium resulting in Eq. 4.3. The first situation is possible if different types of bearings were used in the specimen, if bearings experience substantially different pressure, temperature or velocity conditions or if bearings undergo different horizontal displacements due support flexibility or torsional response. The latter situation is likely due to the presence of overturning moments during earthquake excitations acting on the rigid block. In this case, the distribution of axial loads in the bearings fluctuates to maintain equilibrium under the added overturning moments, shifting the instantaneous center of rigidity away from the center of mass. Thus, the amount of torsion of a rigid block about a vertical axis is expected to be small if the bearings are acting on the same stage (likely if there is little torsion) and if the fluctuation of axial load in the bearing due to transient overturning moments is small compared to the axial load due to gravity and vertical excitations.

Figure 4.22 Rigid block experimental setup with offset center of mass at the UC Berkeley Earthquake Simulator Laboratory

Table 4.8 Source records and associated peak ground displacements for the offset block experimental tests

Source Record	*Peak Ground Displacement (in)*		
	X	*Y*	*Z*
Duzce, Turkey	1.347	1.651	0.621
Erzincan, Turkey	0.774	0.614	0.211
Imperial Valley, El Centro 7	0.591	1.073	0.224
Imperial Valley, El Centro Differential Array	1.650	0.505	0.418
Landers, California	9.460	2.510	0.772
Loma Prieta, California	1.447	0.538	1.433
Superstition Hills, California	1.050	0.310	0.000

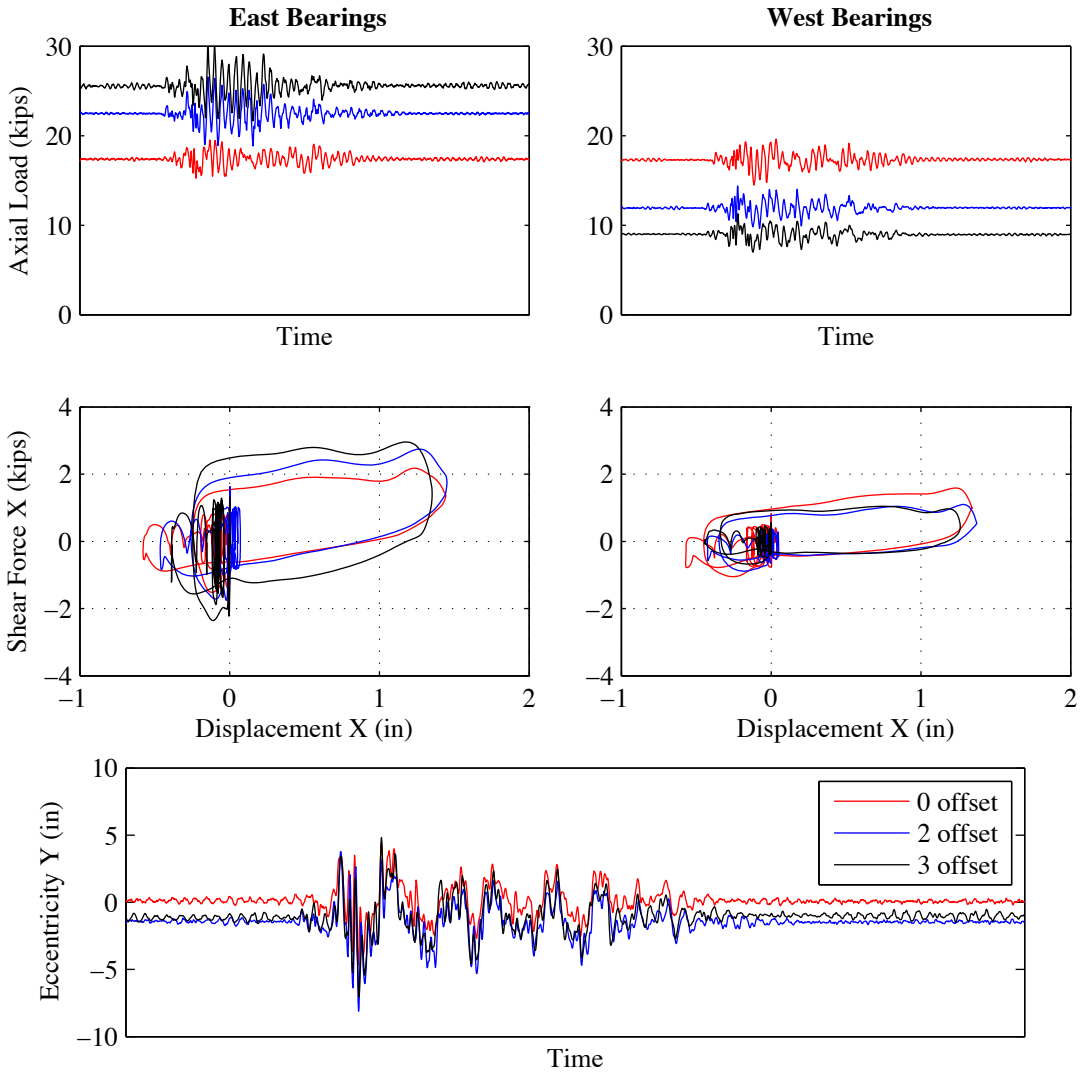

Figure 4.23 Axial loads, *X* direction hysteresis loops and eccentricity for Erzincan earthquake excitation with 0, 2 and 3 blocks offset from experimental data

Table 4.9 TFP bearing properties used in offset block experiment

	Surface 1	*Surface 2*	*Surface 3*	*Surface 4*
R (in)	6	6	18.64	18.64
μ	0.048	0.048	0.1	0.1
D_{out} (in)	3.2	3.2	8.5	8.5
D_{in} (in)	2	2	4	4
h (in)	0.75	0.75	1.25	1.25

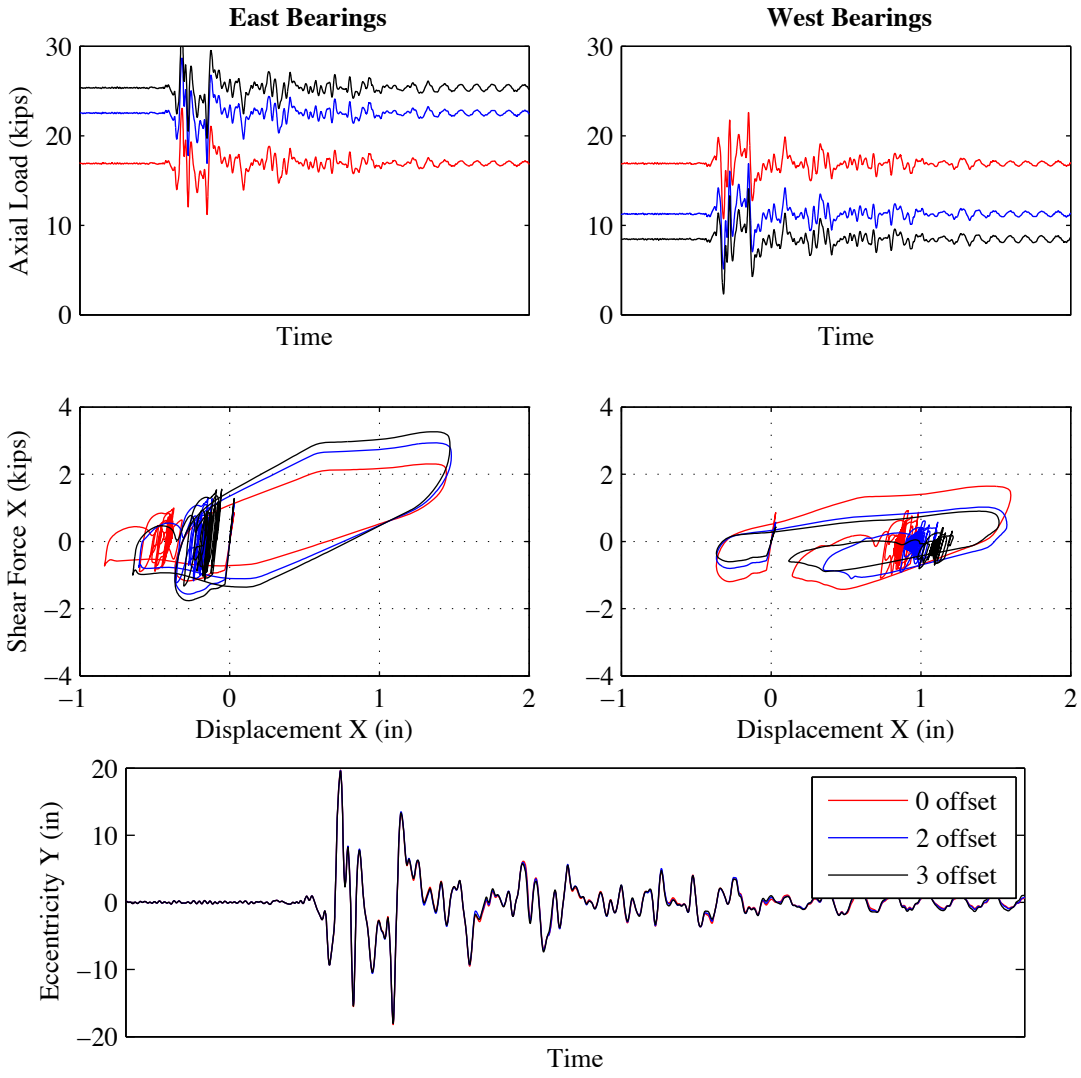

Figure 4.24 Axial loads, X direction hysteresis loops and eccentricity for Erzincan earthquake excitation with 0, 2 and 3 blocks offset from numerical simulation

The TFP bearing model developed in Chapter 2 was implemented to simulate the experimental setup. The properties of the TFP bearings used in the experiments are shown in Table 2.1. Friction coefficients were found using unidirectional sine wave tests. For the bearings used in this set of experiments, the friction coefficients for the outer two surfaces were found to be identical. Each of the four bearings was modeled separately, all with the same bearing properties. The axial loads on each bearing were different and continually fluctuated due to the overturning moments in both the *X* and *Y* directions. Vertical accelerations of the shake table and mass block were not included in the numerical model. The tangent horizontal and rotational stiffnesses of the system were compiled from the *X* and *Y* stiffnesses of the four bearings considering their deformed configuration and the axial load induced by gravity and overturning moments at each time step using the appropriate transformation matrices. As before, no viscous damping was considered in the analyses.

Figure 4.23 and Figure 4.24 show test and computed results for the axial loads, and *X* (North-South) direction bearing hysteresis for the East and West bearings measured during the Erzincan, Turkey earthquake excitation for the three offset mass configurations. The time history of the variation of axial forces and eccentricities differ somewhat in character between the experimental and numerical results, and the hysteretic loop does not recenter in the numerical simulation in one direction. These differenced are not unexpected due to the modeling simplifications described previously. The resulting eccentricity is calculated assuming all bearings are on the same stage of behavior using Eqs. 4.2 through 4.6. No significant difference in eccentricity is observed either numerically or experimentally between the three offset mass cases.

Accordingly, the experimental tests showed that the effect of offsetting the center of mass even by relatively larger amounts does not have a significant influence on behavior in rigid TFP isolated structures under bidirectional earthquake support excitation. The hysteresis loops shown in Figure 4.23 for the bearings on the East and West side of the experiment are similar regardless of the offset of the mass blocks. Displacement orbits measured at the original center of mass (before blocks were offset) for all cases and rotation time histories for the earthquakes run are shown in Figure 4.25 and Figure 4.26. Displacement orbits are similar for all offset cases with decrease in displacements in the 3 block offset case for many of the motions. Interestingly, peak rotation of the rigid block decreased when blocks were offset for all but one earthquake.

Table 4.10 lists the maximum displacements, found from both the experimental results and from the numerical model, in the *X* direction measured at the geometric center of the bearings and at the bearing that experiences the largest displacement in the *X* direction. Values for the increase in displacements show that the model predicts an accurate range of increase when little torsion is seen. However, for motions where greater than 10% increase was seen experimentally, the numerical model greatly over-predicts the increase in displacement. This increase could be due to simplifications made in the numerical model, particularly the assumptions that vertical motions of the specimen can be ignored, and that the steel frame on which the concrete masses were placed was rigid. Flexibility of the steel frame would help evenly distribute the mass and reduce the fluctuation in axial loads on the bearings. The numerically calculated fluctuation in axial loads (shown in Figure 4.24) is much greater than the experimentally measured fluctuation (shown in Figure 4.23) and results in greater eccentricity in the system.

Design codes specify increases in displacement due to torsional response. The ASCE (2005) code gives total displacement D_T due to torsion as

$$D_T = D\left[1 + y\frac{12e}{b^2 + d^2}\right] \tag{4.7}$$

where D is the displacement at the center of rigidity, e is defined as in Eq. 4.6, b and d are the dimensions of the structure and structure and y is the distance form the center of rigidity the element of interest. The term for e in the code includes an addition for accidental torsion of 5% of the longest plan dimension of the structure. If, for the experiments presented here, this is taken to be 5% of 9 ft, Eq. 4.7 results in a 20% increase in displacement of for the corner bearings. As seen in Table 4.10, increase in displacement from the geometric center of the bearings to the bearing that underwent the greatest amount of displacement remained under 20% for all excitations.

The study shows that seismic isolation with triple friction pendulum bearings could be beneficial for irregular structures with non-uniform mass distributions. The horizontal stiffness in elastomeric (rubber) bearings is not linearly related on the axial load (although it is dependent on it); thus torsional coupling is expected to occur when the center of mass if offset. However, Pan and Kelly (1983) found that, for small eccentricities, the transient torsional response in rubber-isolated structures is insignificant. In addition, Jangid and Kelly (2000) show that the effect of eccentricities in rubber isolated structures is dependent on the torsional frequency of the isolation system. In cases where the torsional frequency is greater than the lateral frequency, Eq. 4.7 overestimates when the increase in displacements due to torsion. However, the tendency of the center of mass and center of rigidity to coincide for most loading conditions is a benefit for friction pendulum isolation systems with significant mass eccentricities.

Table 4.10 Maximum *X* displacement measured at the geometric center of the specimen and at the bearing with largest displacement

Source Record	*# Blocks Offset*	*Experimental Results*			*Numerical Results*		
		Max Center Disp X (in)	*Max Bearing Disp X (in)*	*% Inc*	*Max Center Disp X (in)*	*Max Bearing Disp X (in)*	*% Inc*
Duzce, Turkey	0	2.16	2.47	15	1.41	2.82	100
	2	2.19	2.36	8	1.24	2.13	71
	3	1.62	1.71	6	1.61	2.98	84
Erzincan, Turkey	0	1.39	1.45	4	1.52	1.60	5
	2	1.41	1.45	3	1.54	1.60	4
	3	1.31	1.36	4	1.52	1.56	3
Imperial Valley, El Centro Array #7	0	0.96	1.06	10	0.81	1.09	33
	2	0.62	0.73	16	0.90	1.19	32
	3	0.78	0.88	13	0.87	1.09	26
Imperial Valley, El Centro Diff. Array	0	1.79	1.86	4	2.06	2.12	3
	2	1.68	1.71	1	2.08	2.07	5
	3	1.53	1.55	2	2.12	2.32	9
Landers California	0	4.83	5.00	3	5.35	5.76	7
	2	4.82	4.88	1	5.39	5.85	8
	3	4.52	4.67	3	5.33	5.66	6
Loma Prieta, California	0	1.70	1.82	7	2.01	2.13	6
	2	1.81	1.83	1	2.00	2.06	3
	3	1.74	1.76	1	2.02	2.11	4
Superstition Hills, California	0	1.05	1.13	7	1.28	1.31	3
	2	1.02	1.08	5	1.45	1.65	14
	3	1.01	1.05	4	1.38	1.52	10

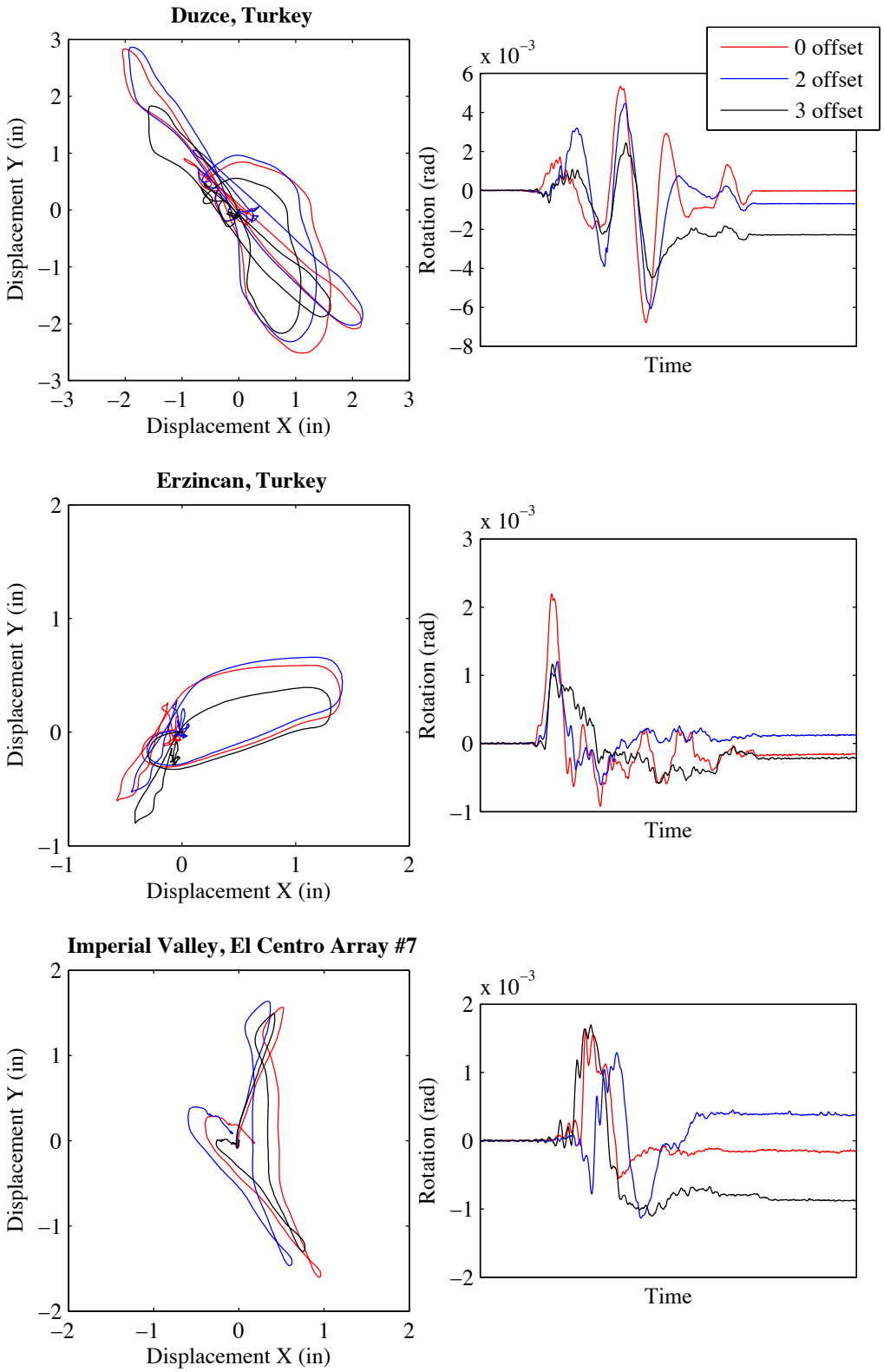

Figure 4.25 Displacement orbits and rotation time histories from 3-component earthquake excitation with 0, 2 and 3 blocks offset from experimental data

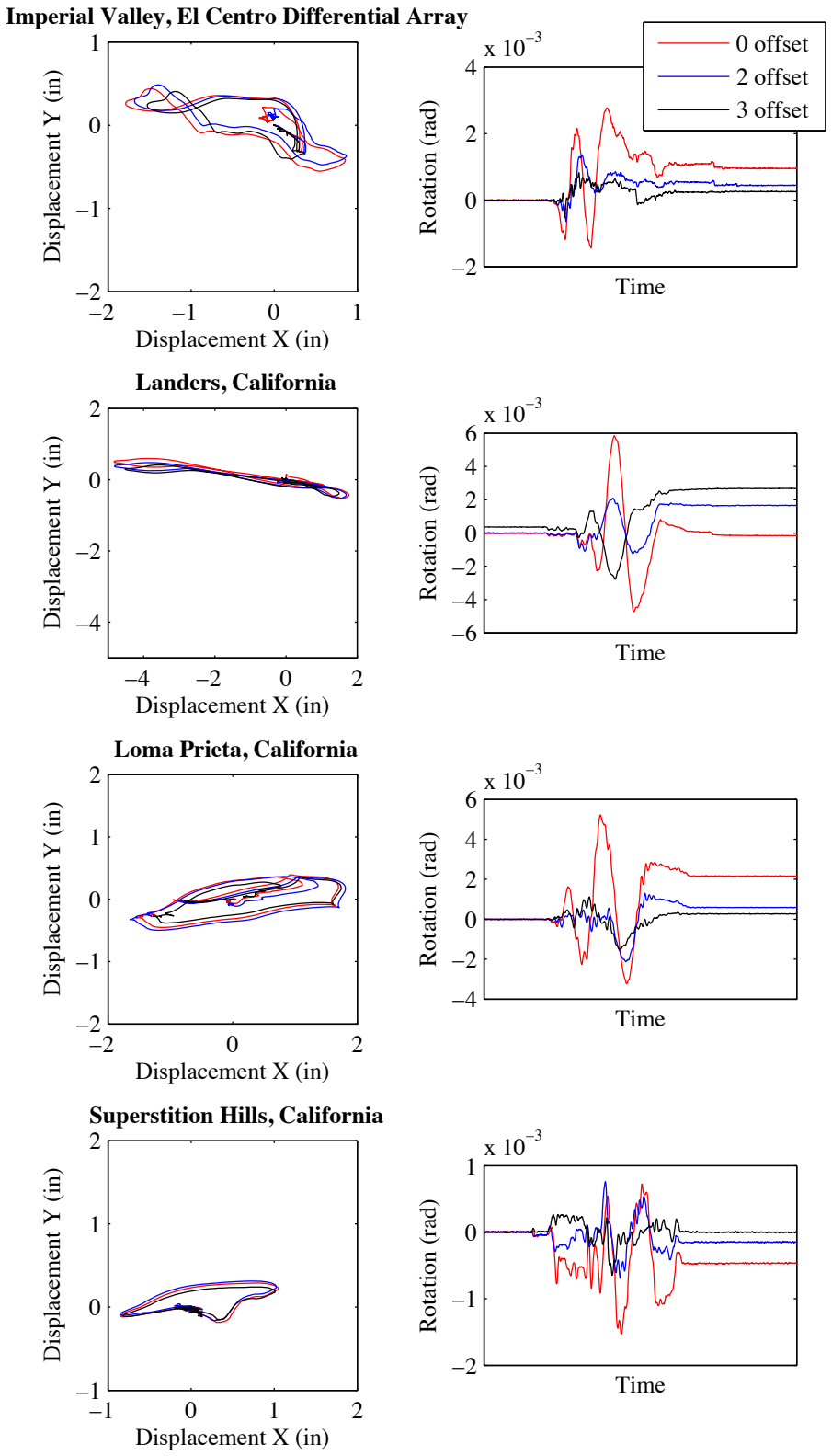

Figure 4.26 Displacement orbits and rotation time histories from 3-component earthquake excitation with 0, 2 and 3 blocks offset from experimental data

5 Effect of Horizontal Rotation on TFP Bearing Behavior

The numerical model described in Chapter 2 has been shown in Chapters 3 and 4 to model the bidirectional behavior of a triple friction pendulum (TFP) bearing reasonably well when the top and bottom of the bearing remain parallel. Many frequently encountered boundary conditions would necessitate models that include global rotation about one or more of the horizontal axes. For example, transient rotations about a horizontal axis can be important in bearings mounted on flexible structural elements, such as at top of cantilever columns in buildings and bridges. Other quasi-static rotations can occur due to the inherent flexibility of the structural system or foundations to which the bearing is attached, construction imperfections and other environmental causes.

Consequently, it is desirable to extend the numerical model developed in Chapter 2 to be able to account for the effect of these rotational degrees of freedom. This will allow engineers to understand the effects of the flexibility of the structure near isolation bearings on the local bearing deformations and forces as well as on the global response, including relative residual displacements and forces among groups of isolators.

In this chapter, the model developed in Chapter 2 is extended to include rotations of the outer concave sliding surfaces of a TFP bearing about the horizontal X and Y axes. As before, rotation about the vertical Z axis is disregarded.

5.1 Extension of the Numerical Model

The model developed in Chapter 2 is used as a basis for the TFP model with global rotations included. Changes are made in the compatibility relations to relax the previous restraint of parallel upper and lower components. There are also additions in the model to account for the effect of global rotations on the sliding surface rotations as well as the P-Δ moments below the bearing. However, basic constitutive behavior of the sliding surfaces remains the same. All other model assumptions, described in Chapter 2, remain in place.

5.1.1 Geometric compatibility relationship

The local rotation vector $\boldsymbol{\theta}$ remains the same as defined for the rotationally restrained problem; it is composed of the relative rotations θ_n of the sliders given in Figure 5.1. The local displacement vector $\mathbf{u}$ also remains the same as the rotationally restrained case and is composed of the associated relative horizontal displacements of the sliding surfaces measured relative to the center of the bearing as described in Section

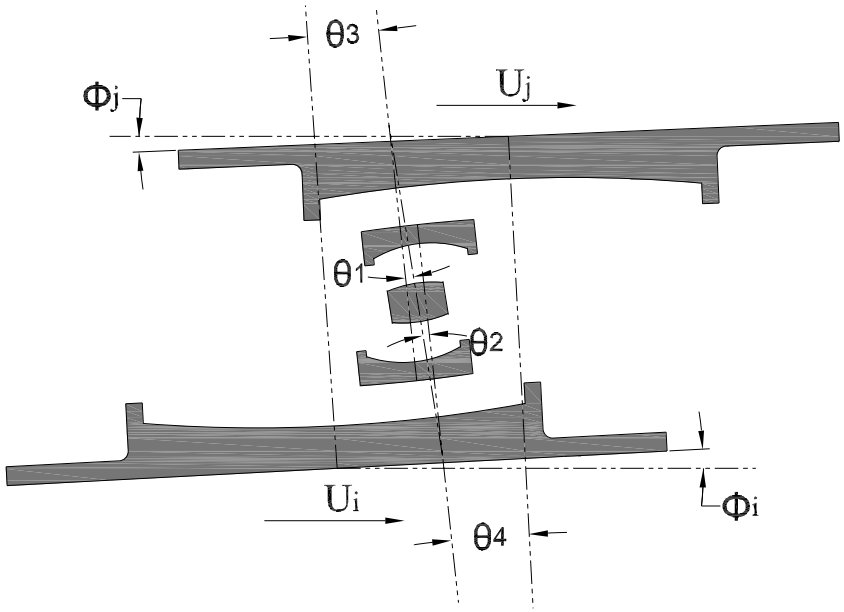

Figure 5.1 Local slider rotations with global rotation allowed.

1.2.1. The transformation matrix $\mathbf{T_{local}}$ from $\boldsymbol{\theta}$ to **u** remains unchanged.

The global displacement vector **U**, which was 8x1 for the rotationally restrained problem, is now 12x1 (6x1 for a unidirectional problem). The additional degrees of freedom are due to the rotation of the top and bottom of the bearing about the *X*- and *Y*-axes. The first eight displacements in the vector are $[U_{Xj}\ U_{Xi}\ \Phi_{Xj}\ \Phi_{Xi}\ \ U_{Yj}\ U_{Yi}\ \Phi_{Yj}\ \Phi_{Yi}]$. The other four displacements may be chosen for simplicity, two from each coordinate direction. This model uses the local rotations in the *X* and *Y* directions of the innermost slider relative to the outer sliders, θ_{1X}, θ_{2X}, θ_{1Y} and θ_{2Y}.

The geometry of the bearing under a combination of translation and rotation is shown in Figure 5.1. In the case where no global rotation was allowed, the rotation of the top sliders equaled the rotation of the bottom sliders. When global rotation is allowed, the difference between the top and bottom slider rotations is equal to the difference between the global rotations in the top and bottom of the bearings. Thus, the local slider rotations and the global rotations of the top and bottom nodes, Φ_{iX}, Φ_{jX}, Φ_{iY} and Φ_{jY} can be related to the local rotations by

$$\begin{aligned} \theta_{1X} - \theta_{2X} + \theta_{3X} - \theta_{4X} &= -\Phi_{iX} + \Phi_{jX} \\ \theta_{1Y} - \theta_{2Y} + \theta_{3Y} - \theta_{4Y} &= -\Phi_{iY} + \Phi_{jY} \end{aligned} \tag{5.1}$$

The global displacement is the summation of the local relative slider displacements; however, the displacement due to global rotation must be included in the case where rotation is allowed because the displacement between the top and bottom of the bearing is desired. Thus, the global displacements become

$$U_{jX} - U_{iX} = \sum_{n=1}^{4} u_{nX} - \frac{H}{2}\Phi_{iX} - \frac{H}{2}\Phi_{jX}$$
$$U_{jY} - U_{iY} = \sum_{n=1}^{4} u_{nY} - \frac{H}{2}\Phi_{iY} - \frac{H}{2}\Phi_{jY} \tag{5.2}$$

Where H is the total height of the bearing. Equations 5.1 and 5.2 are used to develop a transformation matrix **T** between the global displacements **U** and local rotation $\boldsymbol{\theta}$.

$$\mathbf{T} = \begin{bmatrix}
0 & 0 & 0 & 0 & 0 & 0 \\
0 & 0 & 0 & 0 & 0 & 0 \\
-\frac{1}{L_{3X}+L_{4X}} & \frac{1}{L_{3X}+L_{4X}} & \frac{-L_{4X}+\frac{H}{2}}{L_{3X}+L_{4X}} & \frac{L_{4X}+\frac{H}{2}}{L_{3X}+L_{4X}} & 0 & 0 \\
-\frac{1}{L_{3X}+L_{4X}} & \frac{1}{L_{3X}+L_{4X}} & \frac{L_{3X}+\frac{H}{2}}{L_{3X}+L_{4X}} & \frac{-L_{3X}+\frac{H}{2}}{L_{3X}+L_{4X}} & 0 & 0 \\
0 & 0 & 0 & 0 & 0 & 0 \\
0 & 0 & 0 & 0 & 0 & 0 \\
0 & 0 & 0 & 0 & -\frac{1}{L_{3Y}+L_{4Y}} & \frac{1}{L_{3Y}+L_{4Y}} \\
0 & 0 & 0 & 0 & -\frac{1}{L_{3Y}+L_{4Y}} & \frac{1}{L_{3Y}+L_{4Y}}
\end{bmatrix} \ldots$$

$$\begin{bmatrix}
0 & 0 & 1 & 0 & 0 & 0 \\
0 & 0 & 0 & 1 & 0 & 0 \\
0 & 0 & -\frac{L_{1X}+L_{4X}}{L_{3X}+L_{4X}} & \frac{-L_{2X}+L_{4X}}{L_{3X}+L_{4X}} & 0 & 0 \\
0 & 0 & \frac{-L_{1X}+L_{4X}}{L_{3X}+L_{4X}} & -\frac{L_{1X}+L_{3X}}{L_{3X}+L_{4X}} & 0 & 0 \\
0 & 0 & 0 & 0 & 1 & 0 \\
0 & 0 & 0 & 0 & 0 & 1 \\
\frac{-L_{4Y}+\frac{H}{2}}{L_{3Y}+L_{4Y}} & \frac{L_{4Y}+\frac{H}{2}}{L_{3Y}+L_{4Y}} & 0 & 0 & -\frac{L_{1Y}+L_{4Y}}{L_{3Y}+L_{4Y}} & \frac{-L_{2Y}+L_{4Y}}{L_{3Y}+L_{4Y}} \\
\frac{L_{3Y}+\frac{H}{2}}{L_{3Y}+L_{4Y}} & \frac{-L_{3Y}+\frac{H}{2}}{L_{3Y}+L_{4Y}} & 0 & 0 & \frac{-L_{1Y}+L_{4Y}}{L_{3Y}+L_{4Y}} & -\frac{L_{1Y}+L_{3Y}}{L_{3Y}+L_{4Y}}
\end{bmatrix} \tag{5.3}$$

The relationship between global and local displacements is

$$\begin{bmatrix} u_{1\mathrm{X}} \\ u_{2\mathrm{X}} \\ u_{3\mathrm{X}} \\ u_{4\mathrm{X}} \\ u_{1\mathrm{Y}} \\ u_{2\mathrm{Y}} \\ u_{3\mathrm{Y}} \\ u_{4\mathrm{Y}} \end{bmatrix} = \mathbf{T}_{\mathbf{local}}\mathbf{T} \begin{bmatrix} U_{iX} \\ U_{jX} \\ \Phi_{iX} \\ \Phi_{iY} \\ U_{iY} \\ U_{jY} \\ \Phi_{iY} \\ \Phi_{jY} \\ \theta_{1X} \\ \theta_{2X} \\ \theta_{1Y} \\ \theta_{2Y} \end{bmatrix} \tag{5.4}$$

5.1.2 Correction for surface rotations

For the bearing constrained to have parallel top and bottom surfaces, we found in Section 2.2.4 that a correction was needed for the effect of rotation on only the inner sliding surfaces. However, this changes when global rotation is permitted. Allowing the top and bottom surfaces to rotate, we can reexamine at the 1D equilibrium equations (for the free body diagram is shown in Figure 5.2) and resulting force-displacement equations for each surface:

Surface 1:

$$\begin{aligned} F &= f_{N1}\sin\left(\theta_1+\theta_3+\Phi_i\right)+f_{T1}\cos\left(\theta_1+\theta_3+\Phi_i\right) \\ W &= f_{N1}\cos\left(\theta_1+\theta_3+\Phi_i\right)-f_{T1}\sin\left(\theta_1+\theta_3+\Phi_i\right) \end{aligned} \tag{5.5}$$

$$F = W\left(\frac{1}{L_1}u_1+\theta_3+\Phi_i\right)+\mu_1 W = W\left(\frac{1}{L_1}u_1+\frac{1}{L_3}u_3+\Phi_i\right)+\mu_1 W \tag{5.6}$$

Surface 2:

$$\begin{aligned} F &= f_{N2}\sin\left(\theta_2+\theta_4+\Phi_j\right)+f_{T2}\cos\left(\theta_2+\theta_4+\Phi_j\right) \\ W &= f_{N2}\cos\left(\theta_2+\theta_4+\Phi_j\right)-f_{T2}\sin\left(\theta_2+\theta_4+\Phi_j\right) \end{aligned} \tag{5.7}$$

$$F = W\left(\frac{1}{L_2}u_2+\theta_4+\Phi_j\right)+\mu_2 W = W\left(\frac{1}{L_2}u_2+\frac{1}{L_4}u_4+\Phi_j\right)+\mu_2 W \tag{5.8}$$

Surface 3:

$$F = f_{N3}\sin\left(\theta_3 + \Phi_i\right) + f_{T3}\cos\left(\theta_3 + \Phi_i\right)$$
$$W = f_{N3}\cos\left(\theta_3 + \Phi_i\right) - f_{T3}\sin\left(\theta_3 + \Phi_i\right) \tag{5.9}$$

$$F = W\left(\frac{u_3}{L_3} + \Phi_i\right) + \mu_3 W \tag{5.10}$$

Surface 4:

$$F = f_{N4}\sin\left(\theta_4 + \Phi_j\right) + f_{T4}\cos\left(\theta_4 + \Phi_j\right)$$
$$W = f_{N4}\cos\left(\theta_4 + \Phi_j\right) - f_{T4}\sin\left(\theta_4 + \Phi_j\right) \tag{5.11}$$

$$F = W\left(\frac{u_4}{L_4} + \Phi_j\right) + \mu_4 W \tag{5.12}$$

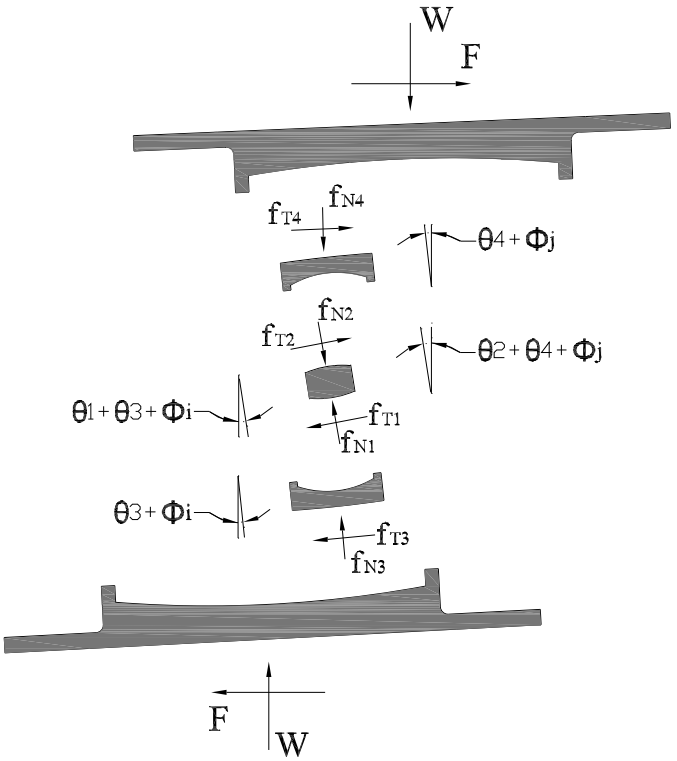

Figure 5.2 Forces in an offset TFP bearing with top and bottom rotation

The effect of displacements on the outer sliding surfaces on force-displacement curve of the inner sliding surfaces remains the same; however, we now find that the force equations of all the sliding surfaces are effected by the global rotations. Force-displacement relations for the bottom sliding surfaces are shifted up by counterclockwise global rotation at the bottom of the bearing; force-displacement relations of the top sliding surfaces are effected in the same manner by global rotation at the top of the bearing.

The transformation between global and local displacements is not one-to-one; there are six global degrees of freedom and four local degrees of freedom for each direction of displacement. Thus, the effect of the global rotations on local force-displacement relations cannot be simply added to the local geometric stiffness matrix described in Section 2.2.4. Instead, we use two geometric stiffness matrices: $\mathbf{k_g}$ from Eq. 2.28 and $\mathbf{k_{Gg}}$ in which is the change in force in the local degrees of freedom due to displacements in the global degrees of freedom. For the bidirectional problem, $\mathbf{k_{Gg}}$ is an 8x12 matrix

$$\mathbf{k}_{Gg} = \begin{bmatrix} 0 & 0 & W & 0 & 0 & 0 & 0 & 0 & 0 & 0 & 0 & 0 \\ 0 & 0 & 0 & W & 0 & 0 & 0 & 0 & 0 & 0 & 0 & 0 \\ 0 & 0 & W & 0 & 0 & 0 & 0 & 0 & 0 & 0 & 0 & 0 \\ 0 & 0 & 0 & W & 0 & 0 & 0 & 0 & 0 & 0 & 0 & 0 \\ 0 & 0 & 0 & 0 & 0 & 0 & W & 0 & 0 & 0 & 0 & 0 \\ 0 & 0 & 0 & 0 & 0 & 0 & 0 & W & 0 & 0 & 0 & 0 \\ 0 & 0 & 0 & 0 & 0 & 0 & W & 0 & 0 & 0 & 0 & 0 \\ 0 & 0 & 0 & 0 & 0 & 0 & 0 & W & 0 & 0 & 0 & 0 \end{bmatrix} \tag{5.13}$$

The matrix is added on after the stiffness is post multiplied by the transformation matrix so that $\mathbf{K} = (\mathbf{T_{local}T})^{\mathbf{T}}\left[(\mathbf{k_s} + \mathbf{k_g})(\mathbf{T_{local}T}) + \mathbf{k_{Gg}}\right]$.

5.1.3 Addition of P-Δ moment

In isolation bearings the relative displacements are large and the P-Δ moment caused by them cannot be ignored. Additionally, there is an added moment from the shear acting at the top of the bearing over the height of the bearing. Physically transferring these moments through the bearing would necessitate nonuniform pressure distributions on the sliders. However, since the model assumes point contacts at the sliding surfaces, these moments must be added in separately to the model. They are added by a global geometric stiffness matrix, $\mathbf{k_G}$, which has the dimensions of the global degrees of freedom, 12x12. The P-Δ moment at the bottom of the bearing is simply the axial load multiplied by the relative global displacement of the bearing, $M_i = W\left(U_j - U_i\right)$. The moment due to the shear at the top of the bearing is due to the shear multiplied by the height of the bearing. Thus, $\mathbf{k_G}$ has only two non-zeros rows,

$$\mathbf{k}_{\mathbf{G}M_{iX},:} = \Big[-W + K_{F_{jX}U_{iX}}H \quad W + K_{F_{jX}U_{jX}}H \quad K_{F_{jX}\Phi_{iX}}H \quad K_{F_{jX}\Phi_{jX}}H \quad K_{F_{jX}U_{iY}}H \quad K_{F_{jX}U_{jY}}H \ldots$$
$$K_{F_{jX}\Phi_{iY}}H \quad K_{F_{jX}\Phi_{jY}}H \quad K_{F_{jX}\theta_{1X}}H \quad K_{F_{jX}\theta_{2X}}H \quad K_{F_{jX}\theta_{1Y}}H \quad K_{F_{jX}\theta_{2Y}}H\Big] \tag{5.14}$$

and

$$\mathbf{k}_{\mathbf{G}M_{iY},:} = \begin{bmatrix} K_{F_{jY}U_{iX}}H & K_{F_{jY}U_{jX}}H & K_{F_{jY}\Phi_{iX}}H & K_{F_{jY}\Phi_{jX}}H & -W + K_{F_{jY}U_{iY}}H & W + K_{F_{jY}U_{jY}}H \ldots \\ K_{F_{jY}\Phi_{iY}}H & K_{F_{jY}\Phi_{jY}}H & K_{F_{jY}\theta_{1X}}H & K_{F_{jY}\theta_{2X}}H & K_{F_{jY}\theta_{1Y}}H & K_{F_{jY}\theta_{2Y}}H \end{bmatrix}$$

(5.15)

The global geometric stiffness matrix $\mathbf{k_G}$ is added to the stiffness matrix **K** before it is condensed, now to an 8x8 matrix rather than the 4x4 matrix shown in Eq. 2.30. The 8x8 matrix includes the stiffness of displacements and moments at the top and bottom of the bearing in the *X* and *Y* directions. As before, the stiffness matrix is updated at each displacement increment.

5.2 Slider Displacements due to Rotation

To investigate the effects of rotation on the TFP bearing an example bearing, with properties described in Table 2.1 and backbone behavior shown in Figure 2.5, is used. When including rotational behavior in the bearing model the total height of the bearing is also needed; for the example bearing, the height is taken as 10 in.

Figure 5.3 shows the local slider displacements in the TFP bearing as either the top or bottom of the bearing is rotated. The global bearing lateral *X* and *Y* displacement is restrained during the rotation. As the bearing begins to rotate, motion begins on the inner sliding surfaces, 1 and 2, where the friction force is the smallest. When motion occurs on these two surfaces only, the local slider rotations can be solved using Eqs. 5.1 and 5.2. When rotation occurs at the bottom of the bearing with zero translation

$$\theta_1 = \frac{-\Phi_b L_2 + \frac{H}{2}\Phi_b}{L_1 + L_2} \text{ and } \theta_2 = \frac{\Phi_b L_1 + \frac{H}{2}\Phi_b}{L_1 + L_2} \tag{5.16}$$

When rotation occurs at the top of the bearing with zero translation

$$\theta_1 = \frac{\Phi_b L_2 + \frac{H}{2}\Phi_b}{L_1 + L_2} \text{ and } \theta_2 = \frac{-\Phi_b L_1 + \frac{H}{2}\Phi_b}{L_1 + L_2} \tag{5.17}$$

For the case of rotation of the bottom of the bearing, sliding continues on the inner two surfaces until sliding begins on the top outer surface, surface 4. This may seem counterintuitive as surface 4 has a larger friction coefficient than the bottom outer surface, surface 3. However, as seen in Eq 5.10, the force on surface 3 increases with the rotation of the bottom of the bearing. Thus, sliding on the surface 3 does is not necessary for force equilibrium and sliding is delayed. For the case of rotation of the top of the bearing, sliding begins on surface 3 before surface 4 and motion on surface 4 is delayed due to the same phenomenon.

5.3 Effect of Permanent Support Rotations on Hysteretic Behavior

As shown in Figure 5.3, when the bottom of the bearing has been rotated by 0.1 radian, but the overall translation of the bearing is restrained, surface 1 moves through a local displacement of 0.25 in and surface 2 moves through a local displacement of 0.75 in in the opposite direction. Thus, surface 2 has traveled almost one third of its displacement capacity for this bearing. Consequently, if a bearing has permanent support rotations, these initial displacements will affect the hysteretic behavior of the bearing under subsequent translations. That is, if surface 2 does not have enough remaining displacement capacity and contacts its restraining rim before μ_4, then the bearing will suddenly harden and exhibit a jump in force until μ_4 is reached. Whether or not there is enough remaining displacement capacity to maintain normal transitions from Stage 1 through Stage 3, the end stages of the TFP behavior will be either shortened or completely suppressed and the ultimate displacement of the bearing will be shortened.

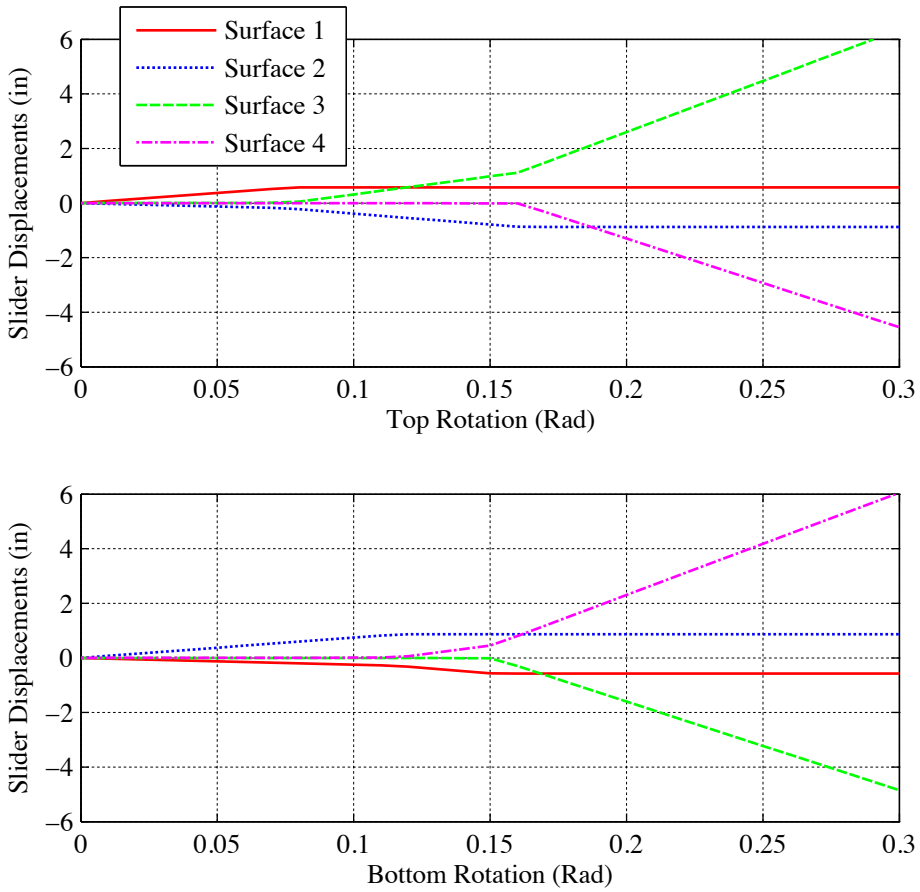

Figure 5.3 Slider displacements due to either top or bottom global rotation of the TFP bearing with zero global translation

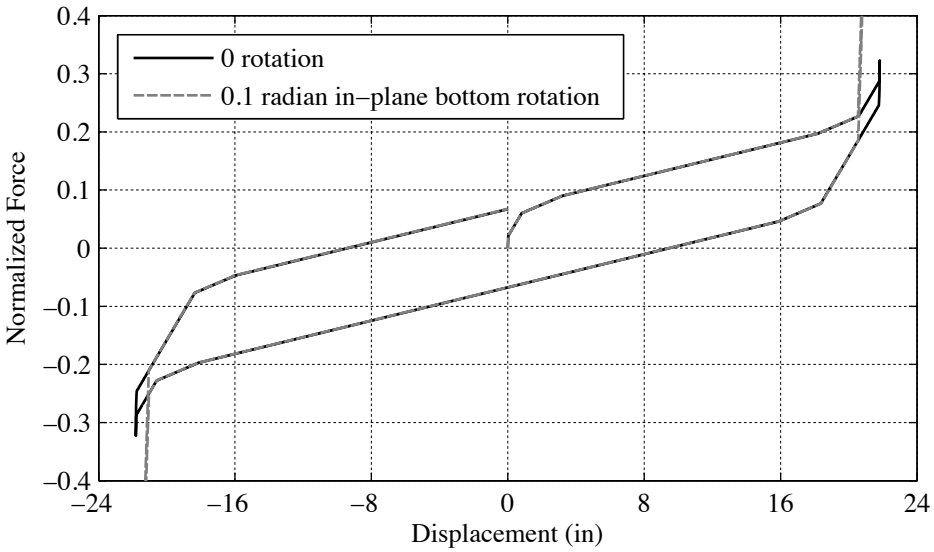

Figure 5.4 1D TFP bearing hysteresis with and without permanent in-plane rotation

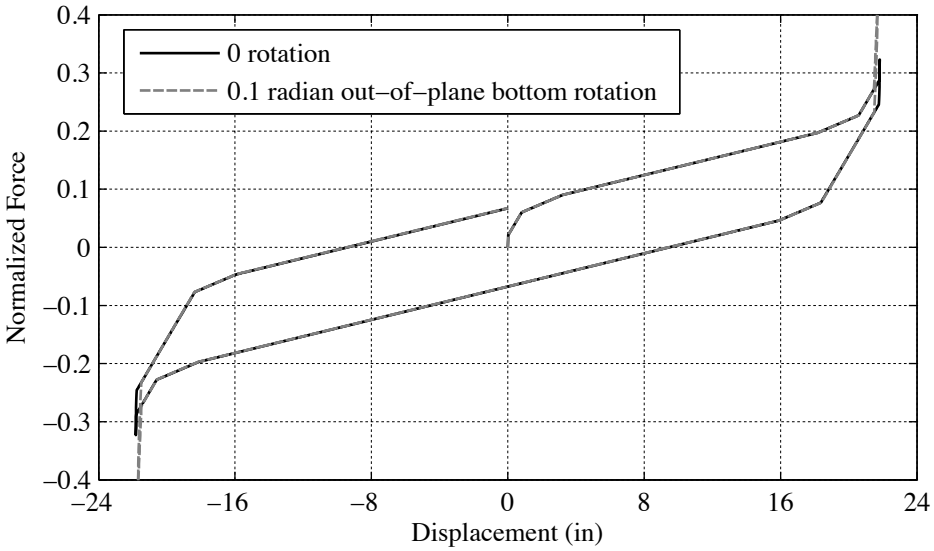

Figure 5.5 1D TFP bearing hysteresis with and without permanent out-of-plane rotation

Figure 5.4 shows the 1D hysteretic behavior of the example bearings when the bottom of the bearing has been rotated in-plane 0.1radian. The displacement capacity of the bearing has been shortened by over an inch in the positive direction and just under an inch in the negative direction. In the positive direction, Stage 5 of the typical bearing behavior has been eliminated. The effect of permanent support rotation on bearing behavior depends on bearing geometry. However, the preservation of the smooth transition between the first three stages of motion can be maintained by modifying Eq. 1.17 to

$$\mu_4 \le \mu_2 + \frac{u_{\max 2} - u_{2\text{initial}}}{L_2} \tag{5.18}$$

where $u_{2\text{initial}}$ is the displacement on surface 2 due to the permanent rotation. Assuming that only the inner sliders are displaced due to the rotation and substituting in Eqs. 2.4 and 5.16, the maximum allowed permanent rotation of the bottom support to ensure smooth transitions through Stage 3

$$\Phi_{i\max} \le \left[\frac{u_{\max 2}}{L_2} - \left(\mu_4 - \mu_2\right) \right] \frac{L_1 + L_2}{L_1 + \dfrac{H}{2}} \tag{5.19}$$

For the example bearing, this rotation is 0.25radians. However, at this rotation the motion would have stopped on the inner surfaces and began on the outer surfaces, thus the assumption that only the inner sliders displaced would not hold. As a result, for the example bearing geometry, smooth transition through Stage 3 will always occur.

Figure 5.5 shows the effect of out-of-plane rotation of the bottom of the bearing on the bearing behavior. The effect from out-of-plane rotation is less than the in-plane rotation; for the example bearing the displacement capacity is reduced by less than half an inch. When the bearing is rotated out-of-plane, the stiffness of the surfaces in-plane are increased according to Eq. 2.5. However, for the example bearing, the effect is negligible.

5.4 Effect of Flexible Supports on Behavior

To examine the effect of placing a TFP bearing on top of a flexible support, the example bearing was modeled on top of a 12 ft tall column and the column stiffness was varied to achieve different rotations during response. The bearing was given a constant axial load of 200kips. The rotation of the top of the bearing was restrained to remain horizontal as would occur in a building with a rigid diaphragm above the isolation layer or in a bridge with a rigid bent cap over a group of bearings. A sketch of the idealized setup is shown in Figure 5.6.

The supporting column was designed with three different flexural stiffnesses. The first is a rigid column with theoretically infinite stiffness. The second stiffness was chosen to limit the column drift to 1.25% at 18in bearing displacement. Eighteen inches was chosen because it is the displacement at which the bearing transitions to Stage 5 and hardens significantly. This displacement is often used as the maximum displacement for the median maximum considered earthquake. The third stiffness was chosen to limit the column drift to 2.5% at 18in bearing displacement. For the column with 1.25% drift limit, EI was equal to $3.54*10^7$ kip-in^2; for the column with 2.5% drift limit, EI was equal to $1.77*10^7$ kip-in^2. The column is assumed to remain elastic in these analyses. The effect of geometric nonlinearities due to the lateral displacement of the loads acting on the bearing are considered in predicting the displacement of the column.

Lateral loading on the column is initially considered to be quasistatic. These cyclic loading excursions were then followed by cases of dynamic loading.

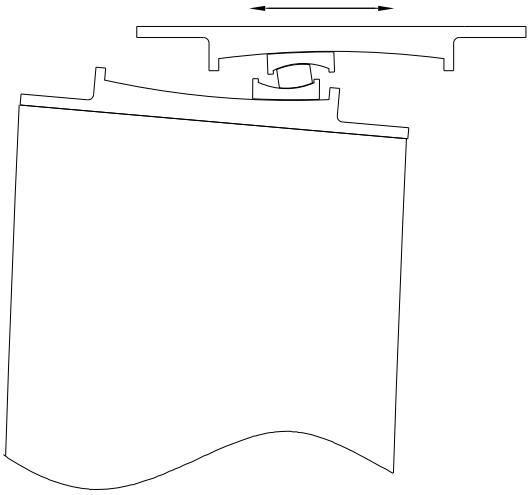

Figure 5.6 TFP bearing on top of a flexible column with rotation at the top of the bearing restrained

5.4.1 Quasistatic Cyclic loading

For quasistatic cyclic loading, the bearing was cycled in 1D to the ultimate bearing displacement capacity. The distance the bearing was cycled varied with the flexibility of the column as the force in the bearing depends on the relative bearing displacement between the top of the bearing and top of the column. The bearing hysteresis, and resulting displacement and rotation of the top of the column are shown for the three configurations in Figure 5.7. The hysteresis shows that as the stiffness of the column decreases, the forces at which transitions in bearing behavior decrease and the stiffness of the bearing decrease. This result is in agreement with the effects of placing a single friction pendulum bearing on top of a flexible support described by Gilberto et al. (2004b). In addition to the change in stiffness, the displacement capacity of the bearing decreases slightly. However, the total displacement that the top of the bearing moves before ultimate displacement is reached increases with the flexibility of the column sine the flexible column translates more. As expected, the column rotates clockwise with positive displacement due to the large P-Δ moment.

Figure 5.8 shows the local slider displacements for the three column stiffnesses for the initial positive global displacement portion of the loading cycle. The local displacements are plotted against the global relative displacement of the bearing, defined as the difference between displacements of the top and bottom nodes of the bearing. The first difference in behavior is seen when the bearing is traveling on surfaces 2 and 3. Here the increases in displacement on surface 2 relative to the relative displacement of the bearing decreases as the column flexibility increases. This is because the clockwise rotation at the bottom of the column increases with the flexibility of the column. Looking at Figure 5.3, counterclockwise rotation at the bottom of the bearing causes positive displacement on surface 2; thus, clockwise rotation would decrease the displacement on surface 2. The second difference in behavior is that motion on surface 4 initiates at a greater relative displacement when the bearing is on a more flexible column. Then, when the bearing is sliding on the two outer surfaces, displacement on surface 3 relative to the

displacement of the bearing is greater with a more flexible column whereas displacement on surfaces 4 is less. These changes in rate of local displacement can be explained in the same manner as the displacement on surface 2.

One interesting result form the bearing on the most flexible column is that motion resumes on surface 1 much earlier in the relative bearing displacement than with a rigid column. Thus, when the bearing approaches its ultimate displacement limit, there is no displacement capacity remaining on surface 1. However, there is remaining capacity on surface 2. When the displacement continues on the top of the bearing, the top of the column continues to rotate clockwise. In order to enforce compatibility, surface 2 begins to reverse in motion even though the displacement is still positive.

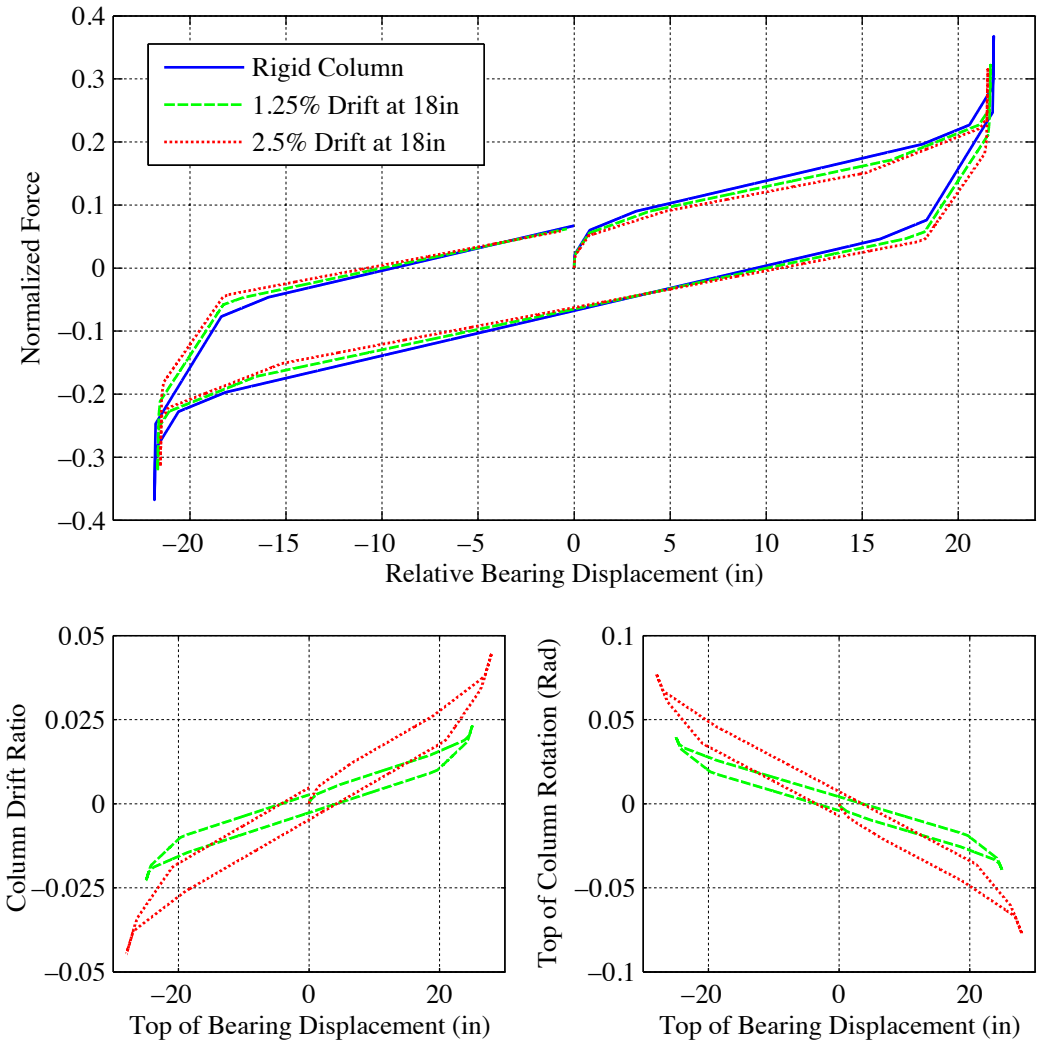

Figure 5.7 1D behavior of TFP bearings on top of columns of varying flexibility, including bearing hysteresis and displacements and rotation of the top of the column

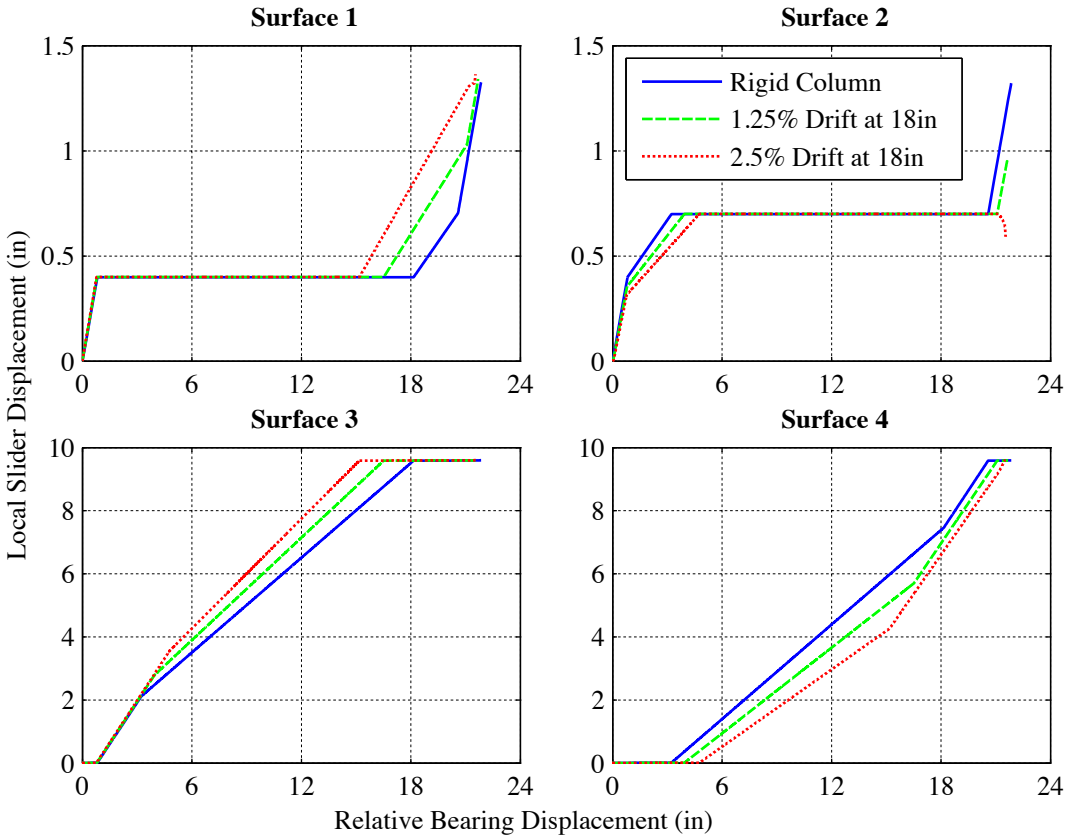

Figure 5.8 1D TFP slider displacements for a bearing on top of a column of varying stiffness

5.4.2 Dynamic loading

To examine the dynamic behavior of the TFP bearing on top of a flexible column, the example bearing was run with bidirectional excitation considering the four earthquakes described in Chapter 4. The earthquakes were run with a length scale of 1; however, the amplitude factors corresponding to the length scale 2 runs from Chapter 4 were used.

The responses of the system to the earthquake excitations are shown in Figure 5.9 through Figure 5.12. It is seen that the flexibility of the column does not have a large effect on the forces and displacement seen at the top of the bearing, suggesting that the global behavior of a structure with a rigid diaphragm supported by TFP bearings on top of columns would be relative unaffected by the column flexibility. However, as expected, column rotations and drifts are considerably larger with the more flexible columns. Thus, the supports must be capable of withstanding the local demands due to the large P-Δ moments transmitted through the bearing. The addition of rotation to the TFP bearing model will allow for further studies on this topic.

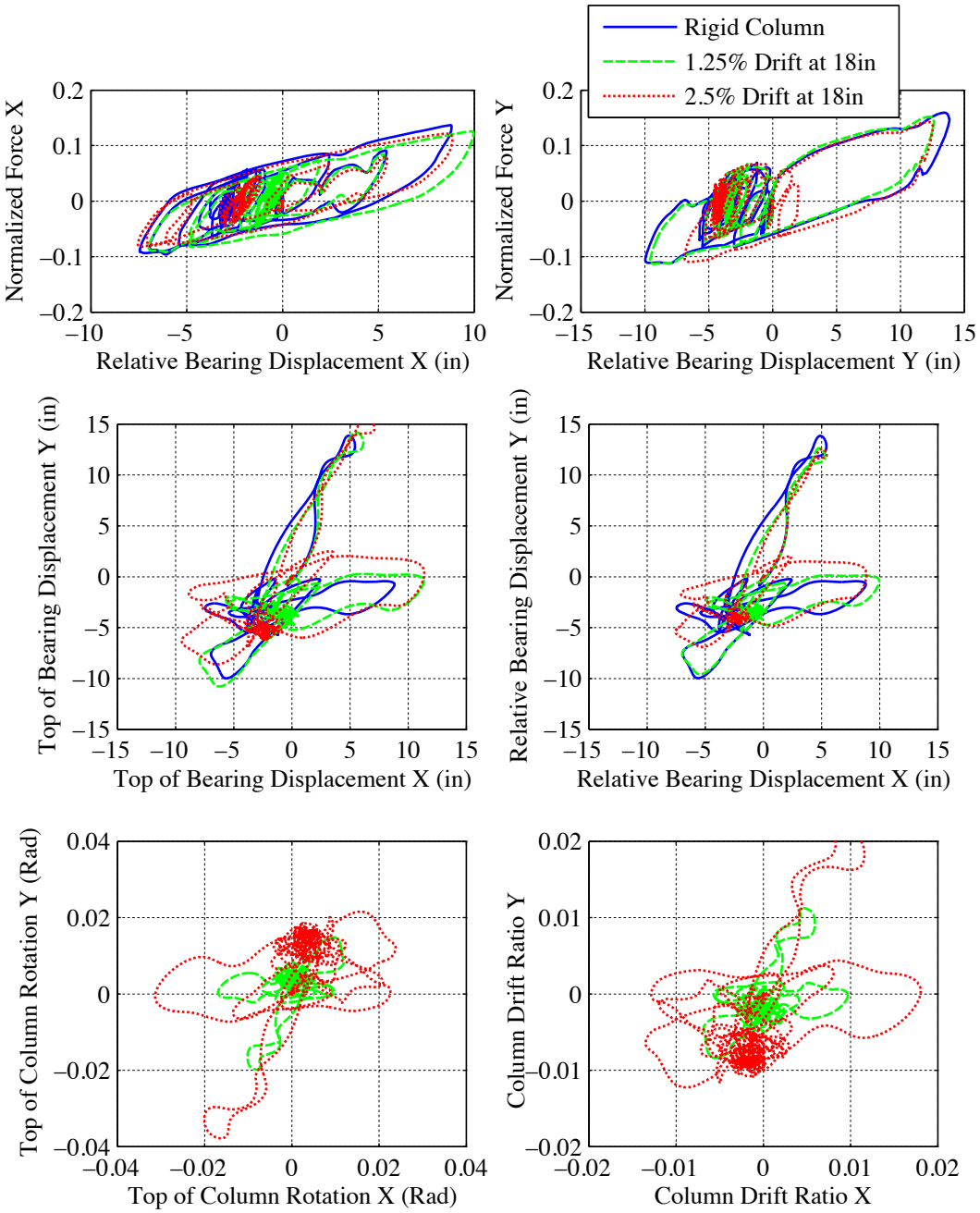

Figure 5.9 TFP bearing supported columns of varying flexibility response to Northridge earthquake Newhall record with 100% amplitude factor, with X and Y excitation

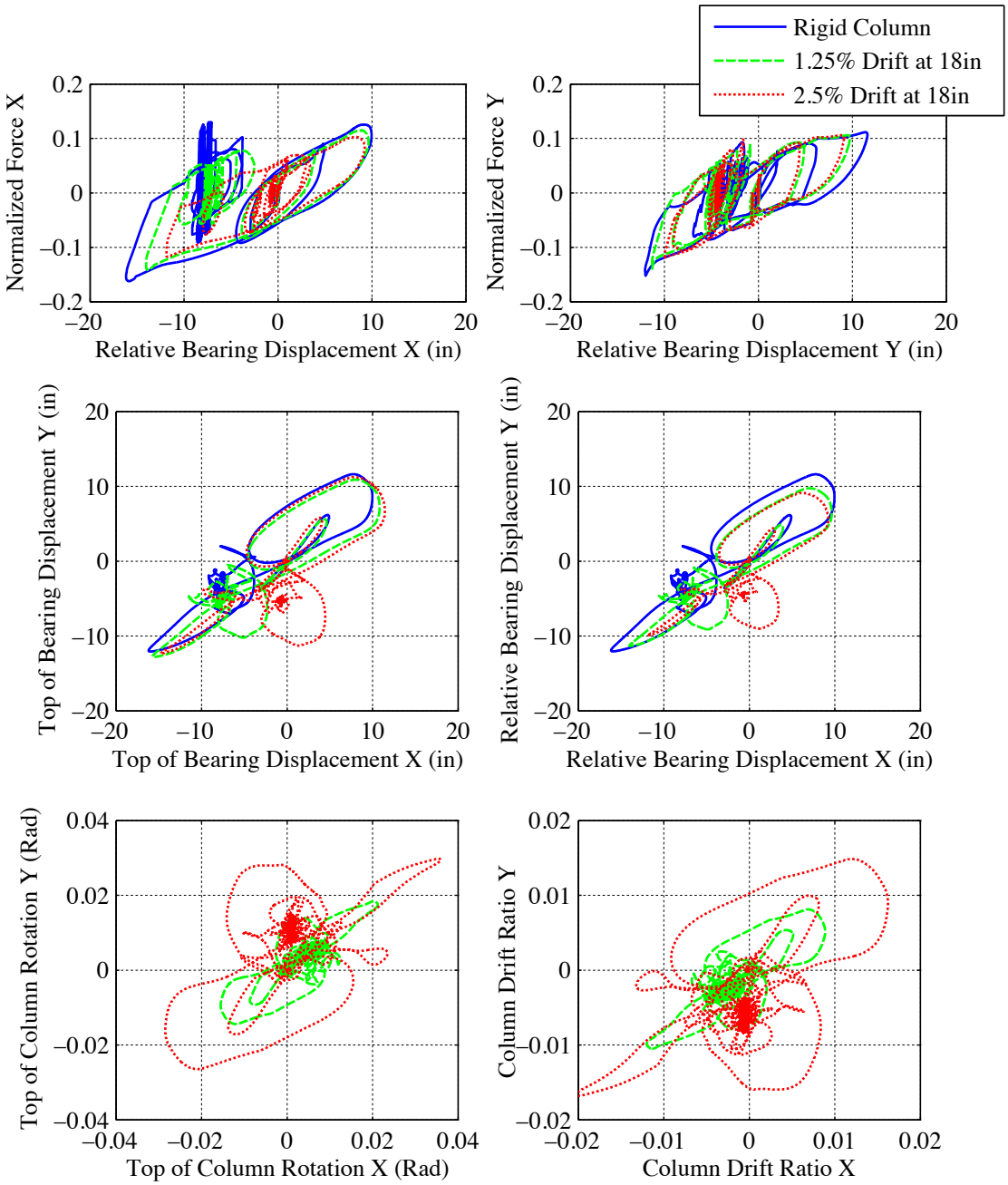

Figure 5.10 TFP bearing supported columns of varying flexibility response to the Kobe earthquake JMA record with 65% amplitude factor, with X and Y excitation

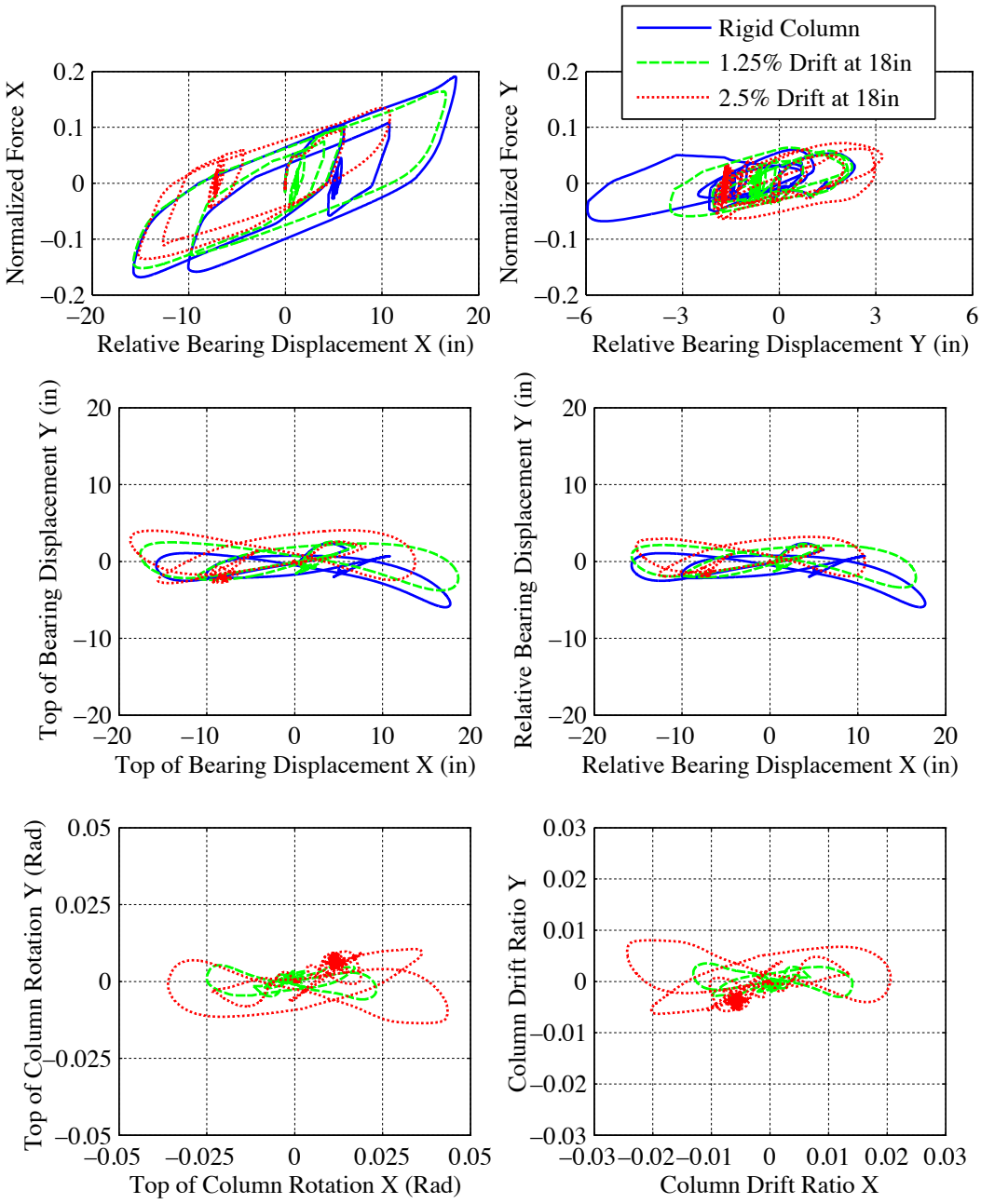

Figure 5.11 TFP bearing supported columns of varying flexibility response to the Northridge earthquake Sylmar record with 44% amplitude factor, with X and Y excitation

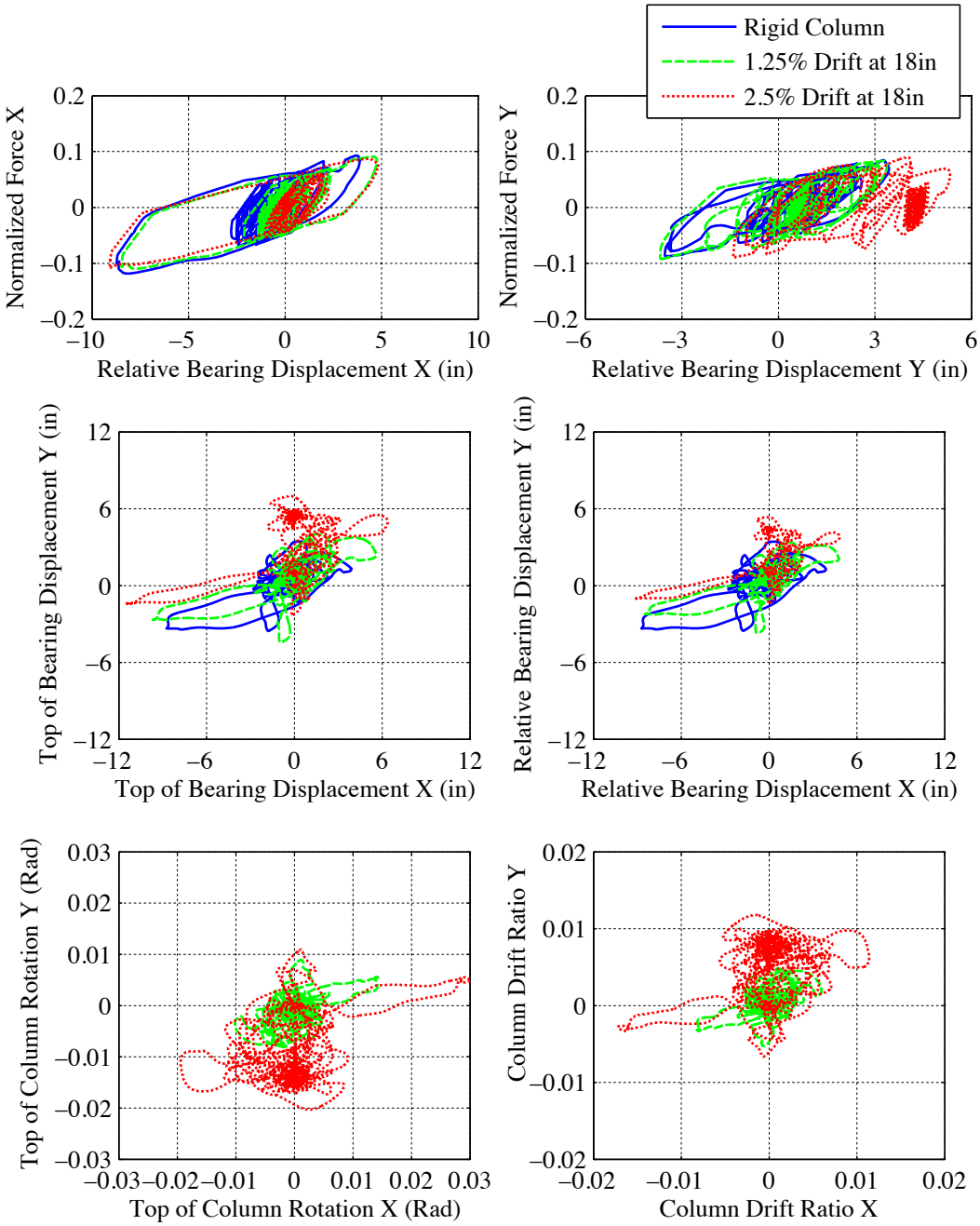

Figure 5.12 TFP bearing supported columns of varying flexibility response to the Tabas earthquake with 50% amplitude factor, with X and Y excitation

6 Approximating Peak Responses in Isolated Buildings

Many isolation systems, including single and triple friction pendulums, lead-plug rubber bearings and crystallizing rubber bearings, exhibit non-linear hysteretic behavior. As shown in Chapters 2 through 4, for the triple friction pendulum (TFP) bearing, these non-linear properties are often complex, but can be tailored to provide increased confidence of achieving particular performance goals. While the numerical models developed in Chapters 2 and 5 permit detailed assessment of response by means of nonlinear time-history analyses, such analyses are time consuming and inefficient in the preliminary stages of design where suitable bearing properties are being sought to achieve particular performance goals. It would be therefore desirable to have a simplified analysis tool that can estimate peak structure response parameters, such as story drifts, floor level accelerations and even floor spectra directly from the design spectrum.

In this chapter, the ability of several modal response spectrum methods to estimate peak responses of isolated buildings is investigated. The resulting estimates are compared to mean peak responses obtained from nonlinear time-history analyses of various isolation systems. For the time-history analyses, the experimentally validated numerical model presented in Chapter 2 as well as other classic isolator models are used to simulate the response of structures with three different heights supported on three types of bearings. This study is focused on situations where performance criteria stipulate little or no damage to the structural and nonstructural elements during the earthquake shaking considered. As such, the structure is assumed to remain elastic.

Multiple engineering design parameters are typically used to characterize response for performance-based design. This chapter focuses on parameters that include: peak roof displacement, peak isolator displacement, peak story shears and drifts and floor response spectra.

Roof displacement relative to the top of the isolation plane provides a useful index of overall structural response. By dividing by the height of the roof relative to the isolation plane, the resulting roof drift index can be used to assess structural and nonstructural damage in an average sense. Aschheim and Black, 2000 use simple methods to estimate drifts at which different structural systems will yield, based on the basic configuration and proportions of the structural system and the strength of materials used. It has been shown that most of the likely lifetime cost of earthquake repair of most buildings is associated with nonstructural contents (Aslani and Miranda, 2005, Mayes 2002). As such, the roof drift ratio provides a useful index for assessing the potential for damage in displacement sensitive nonstructural elements such as partitions, cladding, stairways, elevators and so on. Drifts in individual stories can vary significantly over the height of a structure due to changes in configuration, variations in mass and stiffness with height, higher mode effects, etc. Consequently, for more detailed assessment or to refine a design, it is important to exam story drifts.

The story shears and their variation over the height of an isolated structure are also of importance for design of the structure. Studies by Kikuchi et al. (2008) and Politopoulos and Pham (2009) find that once yielding occurs in an isolated structure, failure is more likely to occur than when yielding occurs in a fixed base structure, further emphasizing the importance of understanding force demands in the superstructure.

Many types of nonstructural elements are sensitive to accelerations. These elements include ceilings, piping systems, equipment rigidly connected to the structure, cladding (out-of-plane response) and so on. While the peak floor level acceleration may be a useful engineering design parameter for many applications, floor response spectra are more generally applicable. Typically, floor spectra are obtained only after conducting nonlinear time history analyses and computing the response spectra for the acceleration records obtained at the floors of interest.

Thus, the ability to accurately estimate engineering demand parameters for non-linear isolated buildings at the early stages of design would have great benefit in terms of selecting and optimizing isolation systems, as well as improving our understanding isolated system dynamics.

6.1 Isolated Building Model and Ground Motions

For these investigations, relatively simple elastic structure models will be utilized to illustrate the underlying modal analysis techniques. It is important to examine their capability to estimate peak response over a broad range of buildings and isolation systems. Three different height superstructures are considered. For each, three sets of isolators are used having different period and damping pairs. Isolation systems used in this investigation include: linear elastic bearings with linear viscous dampers, bilinear isolators representative of single pendulum friction bearings, and TFP bearings.

For the sake of simplicity in these examples, only planar structure models are considered, subjected to unidirectional horizontal ground shaking. In Section 4.3.1, the response, including floor spectra, of isolated structures supported on the TFP bearing under bidirectional ground motion was shown to be adequately approximated by unidirectional inputs.

Current building codes place substantial limitations on the use of modal analysis in the design of isolated buildings. For example, ASCE-7 (2005) requires non-linear time history analyses for all isolated buildings over four stories. Additionally, to be able to use static or modal analysis methods for short buildings, the period of the isolation system must be less than 3.0 s. Lastly, the period of the isolation system must be three times greater than the predominate fixed-base period of the building. Thus, in formulating this study, one of the buildings selected is taller than 4 stories, two have isolation system periods greater than 3 s and two have been selected where the ratio of the periods of the superstructure and isolation system is less than 3. Thus, the potential of extending the range over which modal analysis methods can be used is explored in this chapter.

6.1.1 Ground motions

The ground motions chosen for this study were selected by Baker et al. (2011) for the PEER Transportation Research Program. The motions were selected for a site in

Oakland, CA, 7 km from the Hayward fault with an assumed Vs_{30} = 360 m/s. Sets of 40 earthquake records were included in this set and amplitude scaled to match in an average sense uniform hazard spectra (UHS) for the site. In this chapter, results are only presented for the motions corresponding to the 10% probability of exceedance in 50 years hazard level. The pseudo-acceleration uniform hazard spectrum is given in Table 6.1. The 10% in 50 years records include 16 motions with significant velocity pulses with periods of 1 to 7 seconds in the fault normal direction. As this study considers only unidirectional response of the isolated structure, both fault normal and fault parallel records are run individually in the time history analyses, resulting in a suite of 80 motions. The mean displacement and pseudo-acceleration spectra for 5% viscous damping for these 80 records are plotted in Figure 6.1 and compared to curves corresponding to the target uniform hazard spectrum. The displacement spectrum shown in this figure is used for the modal response spectrum analyses of the isolated buildings.

Table 6.1 5% damped uniform hazard spectrum for Oakland, CA with 10% probability of exceedance in 50 years

T (s)	0.0	0.1	0.2	0.3	1.0	2.0	5.0
Sa (g)	0.94	1.78	2.20	2.13	1.14	0.60	0.22

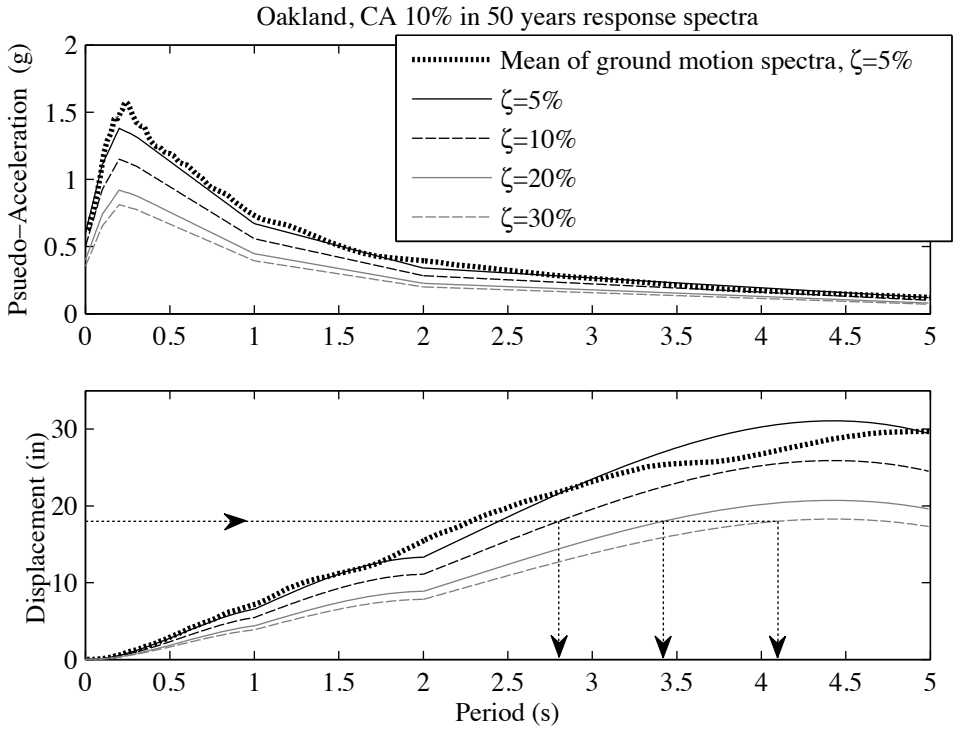

Figure 6.1 Oakland site-specific spectra for multiple damping ratios

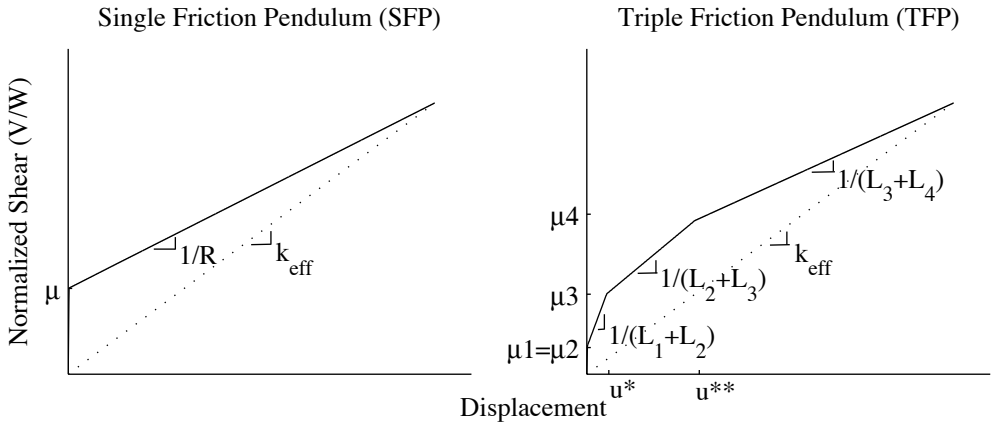

Figure 6.2 Single and triple friction pendulum backbone curves for the design basis earthquake displacement

The desired isolation bearing properties are determined from the response spectra to provide a broad range of isolator characteristics (i.e., not to particularly optimize response). First, three equivalent viscous damping ratios for the isolation system were selected, 10%, 20% and 30%. To compute the spectra for these damping ratios, the mean displacement spectrum computed for 5% viscous damping from the 80 records is divided by the damping reduction factor, B_M, from ASCE-7 (2005). For 10%, 20% and 30% viscos damping, the reduction factors are 1.2, 1.5 and 1.7, respectively. The target displacement is chosen so that the 30% damped system would not need an excessively high period to achieve it. Accordingly, 18 in was chosen as the target displacement. Yang et al. (2010) showed that the average displacement of the isolation system is almost independent of the superstructure stiffness; thus, the properties of the isolator can be chosen without consideration of the period of the superstructure. The corresponding equivalent periods are then found directly from the spectra for each target displacement and equivalent damping ratio, as illustrated in Figure 6.1. The equivalent period and damping ratio pairs are given in Table 6.2.

6.1.2 Bearing properties

The bearings considered in this study include single friction pendulum bearings (SFP) and triple friction pendulum bearings (TFP). Additionally, this study looks at a system of linear elastic bearings (such as natural rubber bearings) combined with linear viscous damping, referred to below as the LV system. The SFP bearing behavior is bilinear hysteretic and is described in Chapter 1. It is representative of other types of isolation systems exhibiting this bilinear behavior. The TFP bearing has a more complicated hysteric behavior, described in Chapter 2.

The ASCE (2005) code uses effective linear stiffness and effective viscous damping ratios to estimate the behavior of non-linear isolation bearings. Fadi and Constantinou (2010) found that this provides a good estimate of maximum isolator displacements especially when averaged over many motions. The effective period, T_{eff}, and damping ratio, ζ_{eff}, are given by

$$T_{eff} = 2\pi\sqrt{\frac{W}{k_{eff}\,g}} \tag{6.1}$$

and

$$\zeta_{eff} = \frac{E_{loop}}{2\pi k_{eff} D^2} \tag{6.2}$$

in which E_{loop} is the energy dissipated in each cycle of the isolator, k_{eff} is the effective linear stiffness and D is the maximum displacement of the isolator under the specified level of motion. A visual representation of k_{eff} for the SFP and TFP bearing is shown in Figure 6.2.

For the SFP bearing, the equivalent stiffness and energy dissipated in a symmetrical cycle at a displacement, D, are

$$k_{eff} = \frac{\mu + \frac{1}{R}\left(D - D_y\right)}{D} W \tag{6.3}$$

and

$$E_{loop} = 4\left(\mu - \frac{1}{R} D_y\right)\left(D - D_y\right) W \tag{6.4}$$

where D_y is the displacement of the isolator assembly at which motion on the sliding surface initiates. For SFP bearings Sheller and Constantinou (1999) suggest using D_y = 0.01 in, but larger values may be appropriate depending on the number, thickness and type of liner materials used and on the flexibility of the subassembly used to attach the isolator to the structure. As the behavior of the SFP bearing is governed by two independent parameters, at a target displacement there exists a single design for a specified period and equivalent damping ratio.

TFP bearings are commonly designed to displace to Stage 3 of the backbone behavior, described in Chapter 1, during a design basis earthquake having a probability of exceedance of 10% in 50 years. For this reason, to design the TFP bearing it is assumed that the largest friction coefficient has been reached and the bearing is in Stage 3 of motion. The equivalent stiffness in this sliding stage is

$$k_{eff} = \frac{\mu_4 + \frac{1}{L_3 + L_4}\left(D - u^{**}\right)}{D} W \tag{6.5}$$

where

$$u^{**} = u^{*} + \left(\mu_4 - \mu_3\right)\left(L_3 + L_2\right) \tag{6.6}$$

and where

$$u^{*} = \left(\mu_3 - \mu_1\right) L_1 + \left(\mu_3 - \mu_2\right) L_2 \tag{6.7}$$

The energy dissipated in each cycle at the third sliding stage is found using geometry as

$$E_{loop} = 4\left(\mu_4 - \frac{1}{L_3+L_4}u^{**}\right)DW - 4\left(\frac{1}{L_2+L_3} - \frac{1}{L_3+L_4}\right)u^{**2}W$$
$$-4\left(\frac{1}{L_1+L_2} - \frac{1}{L_2+L_3}\right)u^{*2}W - 4\left(\frac{\mu_1}{D_y} - \frac{1}{L_1+L_2}\right)D_y^2 W \quad (6.8)$$

In addition to the constraints needed to achieve the effective period and damping ratio, it is assumed that the two inner sliding surfaces have identical properties and the two outer sliding surfaces have the same radius of curvature. These assumptions are typical for TFP bearings used in practice today. Even with these constraints, there is not a unique solution for the TFP bearing properties for the given the desired effective period and damping at a target displacement. Reasonable bearing properties are selected through trial and error. These are not necessarily optimal in terms of the engineering demand parameters of interest. The resulting properties for the SFP and TFP bearings are listed in Table 6.2 and the corresponding hysteretic loops computed for them at the target displacement are shown in Figure 6.3.

The isolator radii and friction coefficients chosen using these methods are not necessarily standard sizes and values available from manufacturers. Additionally, in practice, it is difficult to obtain exact friction coefficients, and a range represented by upper and lower bounds is typically specified. The resulting properties presented here are theoretical with the aim of looking at the ability of modal analysis methods to estimate engineering demand parameters of interest for a large range of bearing properties and structural dynamic characteristics.

To model both the TFP and SFP bearings, the TFP bearing model described by in Chapter 2 was used; global rotation of the bearing was restrained. To model the SFP bearings using the TFP model, the radii of the outer concave sliders are set to half of the desired radius of the SFP bearing, $L_3 = L_4 = R/2$, and inner radii are set much smaller, $L_1 = L_2 \ll R/2$. All friction coefficients are set equal to the desired coefficient of the SFP bearing. This study does not consider effects of restrainer or moat impact on the system. Thus, all slider displacement capacities were set large enough so that they would not be reached in both the SFP and TFP systems. This means the TFP system exhibits only the first three stages of behavior.

Table 6.2 Properties of the bearings used building response study

18 in Displacement Design				
ζ_{eff}	T_{eff}	*Bearing Type*	*R or L_1, L_2, L_3, L_4*	*μ, or μ_1, μ_2, μ_3, μ_4*
10%	2.80 s	SFP	91 in	0.037
		TFP	15, 15, 47, 47 in	0.01, 0.01, 0.027, 0.09
20%	3.42 s	SFP	167 in	0.049
		TFP	15, 15, 90, 90 in	0.01, 0.01, 0.046, 0.087
30%	4.10 s	SFP	311 in	0.052
		TFP	20, 20, 175, 175 in	0.01, 0.01, 0.058, 0.07

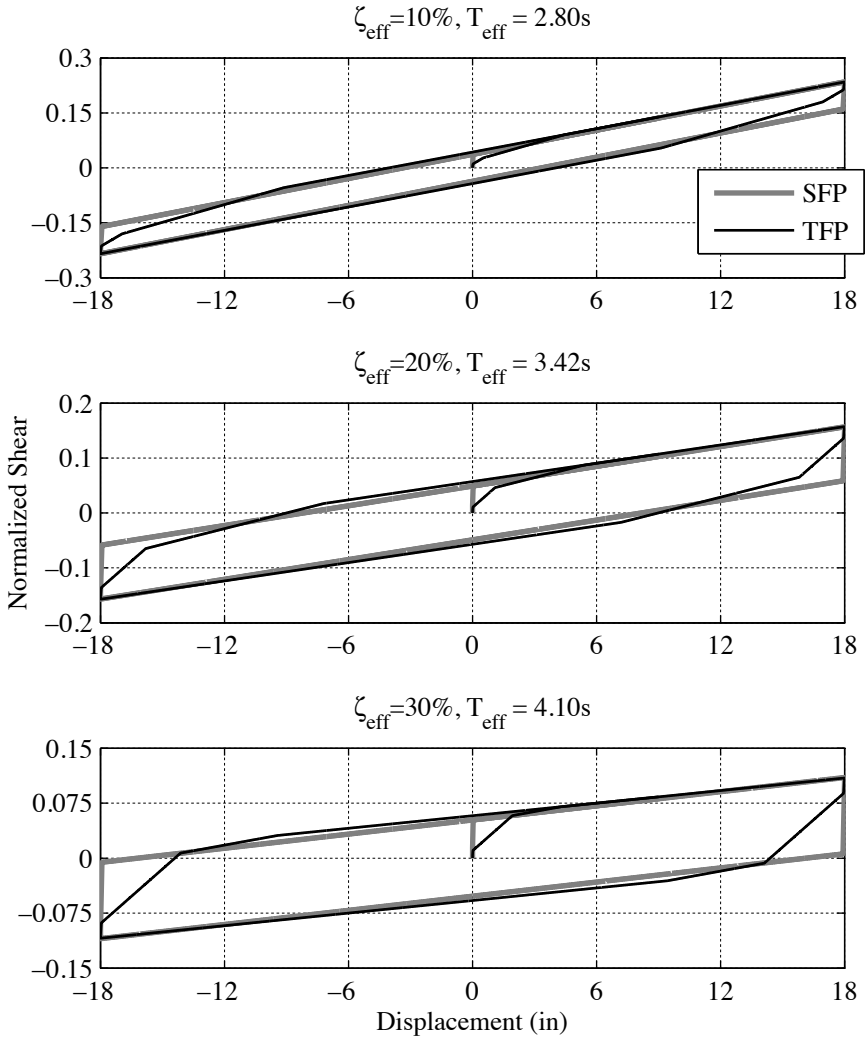

Figure 6.3 Hysteretic loops for friction pendulum bearing designs at 18 inches of displacement

6.1.3 Building properties

In this study, the response of a one-story, a three-story and a nine-story building are investigated. For simplicity, a shear building model with one lateral degree-of-freedom per floor was used to represent the structures. For each building, the floor level mass, *m*, and story stiffness, *k*, remains the same up the height. An additional mass of the same value is added for the floor above the isolators. The three-story isolated building model is shown in Figure 6.4. The predominant fixed base periods were selected to be 0.2 s, 0.6 s and 1.2 s for the one-, three- and nine-story buildings, respectively. The superstructure is assumed to have 2% viscous damping. The story heights are assumed to be 12 ft for all buildings.

As noted previously, the building is assumed to remain elastic and the bearings are assumed to be sufficiently large to avoid impact or other displacement restraints. These assumptions are reasonable considering the purposes of this investigation.

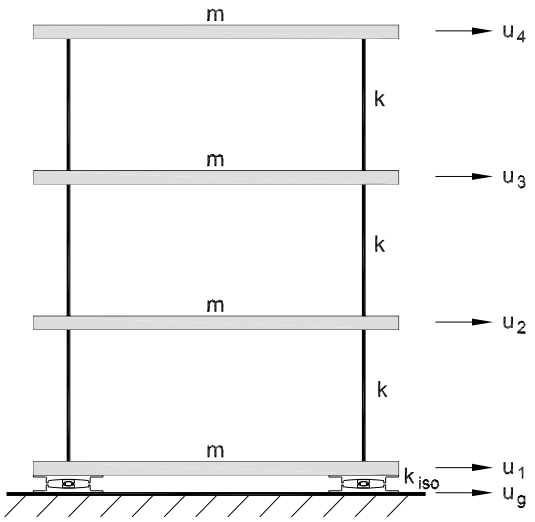

Figure 6.4 Model three-story isolated building

6.2 Modal Response Spectrum Analysis for Isolated Buildings

Classical modal analysis (CMA) uses natural frequencies and modes that are obtained by solving the matrix eigenvalue problem that involves only the mass and stiffness matrix. The orthogonality property of natural modes transforms the system of N coupled differential equations into N uncoupled differential equations. The damping matrix is not used directly in this procedure, rather a damping term that depends on an assumed damping ratio ζ_n is introduced in each mode. This assumption is often acceptable in pratical applications when viscous damping is small and the damping characteristics of the structure are uniformly distributed throughout the structure. However, isolation systems have higher than normal values of damping, and damping is concentrated in the isolation elements. Since isolation tends to reduce the deformations of the superstructure, the amount of damping developed by the superstructure is reduced compared to fixed base conditions. This nonuniformity of damping charactristics in different parts of the structure makes use of CMA problematic.

Chopra (2007) recommends constructing separate damping matrices for subsystems having different damping properties and assembling these to form the overall damping matrix for the system. Ryan and Polaco (2008) warn that even when following this approach, use of mass and stiffness proportional (Rayleigh) damping to represent the damping in the superstructure can cause the response to be underestimated. Ryan and Polaco recommend that only stiffness-proportional damping be to used model superstructure damping. Superposition of modal damping, a method in which the damping for each mode is explicitly stipulated, can also be used to represent damping in an isolated structure. In such cases, the first mode is primarily associated with the response of the isolators. However, these types of models damping simplify the interaction between the isolation level and the superstructure in higher modes.

Generalized modal analysis (GMA) for non-classically damped systems,

described by Igusa et al. (1984) and Veletsos and Ventura (1986), is a more comprehensive method of looking at the behavior of an isolated structure. In generalized modal analysis, the damping matrix is included in the characteristic equation resulting in complex-valued mode shapes. For undamped and classically damped systems, the results from GMA are the same as from CMA. As background to subsequent discussion, a brief review of generalized modal analysis is given below. For more information, refer to Igusa et al. (1984) and Veletsos and Ventura (1986).

Consider the elastic dynamic behavior of the system described by

$$\mathbf{M\ddot{x} + C\dot{x} + Kx = -Mi\ddot{x}_g} \tag{6.9}$$

In which **x** is the *n*-dimension vector of building displacements and **i** is the influence vector. If displacements are measured relative to the ground then **i** is a column vector of ones; if displacements correspond to relative displacement between floors, **i** is a column vector with the first entry equal to one followed by zeros. Solved with classical modal analysis the problem would have eigenvalues ω_i and eigenvectors ϕ_i. To solve the full system including the damping terms as a standard eigenproblem, the *n*-dimensional problem is made into a *2n*-dimensional problem

$$\mathbf{A\dot{z} + Bz = Y} \tag{6.10}$$

where

$$\mathbf{z} = \begin{Bmatrix} \dot{\mathbf{x}} \\ \mathbf{x} \end{Bmatrix} \mathbf{A} = \begin{bmatrix} \mathbf{0} & \mathbf{M} \\ \mathbf{M} & \mathbf{C} \end{bmatrix}, \ \mathbf{B} = \begin{bmatrix} \mathbf{-M} & \mathbf{0} \\ \mathbf{0} & \mathbf{K} \end{bmatrix}, \ \mathbf{Y} = \begin{Bmatrix} \mathbf{0} \\ \mathbf{-Mi\ddot{x}_g} \end{Bmatrix} \tag{6.11}$$

Under free vibration, the right hand side of the equation is zero and there exists a solution

$$\mathbf{z} = \hat{\Phi} e^{st} \tag{6.12}$$

where s_i are the eigenvalues and $\hat{\Phi}_i$ are the eigenvectors. From the definition of **z**

$$\hat{\Phi} = \begin{Bmatrix} s\Phi \\ \Phi \end{Bmatrix} \tag{6.13}$$

where $\mathbf{\Phi}$ are the modal displacements and $s\mathbf{\Phi}$ are the modal pseudo-velocities. The eigenvalues and their associated vectors occur in *n* conjugate pairs. The *i*th pair of eigenvalues are defined as

$$s_i = -\zeta_i \omega_i \pm i\omega_{Di} \tag{6.14}$$

where

$$\omega_i = |s_i|, \ \zeta_i = -\frac{\mathrm{Re}(s_i)}{|s_i|}, \ \omega_{Di} = \omega_i \sqrt{1-\zeta_i^2} \tag{6.15}$$

The terms ω, ζ and ω_D are the natural frequencies, damping ratios and damped natural frequencies of the generalized system.

The free vibration solution is found by summing the responses of all conjugate pairs

$$\mathbf{x} = \sum_{i=1}^{n} \left(C_i \boldsymbol{\Phi} e^{s_i t} + \bar{C}_i \boldsymbol{\Phi} e^{\bar{s}_i t} \right) = \sum_{i=1}^{n} 2\,\mathrm{Re}\left(C_i \boldsymbol{\Phi} e^{s_i t} \right) \tag{6.16}$$

where

$$C_j = \frac{s_j \boldsymbol{\Phi}^T \mathbf{M}\mathbf{x}(0) + \boldsymbol{\Phi}^T \mathbf{C}\mathbf{x}(0) + \boldsymbol{\Phi}^T \mathbf{M}\dot{\mathbf{x}}(0)}{2 s_j \boldsymbol{\Phi}^T \mathbf{M}\boldsymbol{\Phi} + \boldsymbol{\Phi}^T \mathbf{C}\boldsymbol{\Phi}} \tag{6.17}$$

are the complex participation factors.

To find the forced vibration response the free vibration due to initial velocity changes is considered. The coefficient B_j (the value of C_j when $\mathbf{x}(0) = \{\mathbf{0}\}$ and $\dot{\mathbf{x}}(0) = \{\mathbf{1}\} or \begin{Bmatrix} 1 \\ 0 \\ \vdots \end{Bmatrix}$ depending on how the degrees of freedom are defined) are found as

$$B_j = \frac{\boldsymbol{\Phi}^T \mathbf{M}\dot{\mathbf{x}}(0)}{2 s_j \boldsymbol{\Phi}^T \mathbf{M}\boldsymbol{\Phi} + \boldsymbol{\Phi}^T \mathbf{C}\boldsymbol{\Phi}} \tag{6.18}$$

The response of the system to an excitation is found as

$$\mathbf{x} = -\sum_{i=1}^{n} \left[\boldsymbol{\alpha}_i \omega_j \int_0^t \ddot{x}_g(\tau) h_i(t-\tau) d\tau + \boldsymbol{\beta}_i \int_0^t \ddot{x}_g(\tau) \dot{h}_i(t-\tau) d\tau \right] \tag{6.19}$$

where

$$2 B_i \boldsymbol{\Phi}_i = \boldsymbol{\beta}_i + i\boldsymbol{\gamma}_i, \; \boldsymbol{\alpha}_i = \zeta_i \boldsymbol{\beta}_i - \sqrt{1-\zeta_i^2}\,\boldsymbol{\gamma}_i \tag{6.20}$$

The function h(t) is the impulse response function of a single degree of freedom (SDF) system

$$h(t) = \frac{1}{\omega_D} e^{-\zeta\omega t} \sin\left(\omega_D t\right) \tag{6.21}$$

and

$$\int_0^t \ddot{x}_g(\tau) h_i(t-\tau) d\tau \tag{6.22}$$

is commonly known as Duhamel's integral. Equation 6.19 can be re-written as

$$\mathbf{x} = \sum_{i=1}^{n} \left[\boldsymbol{\alpha}_i V(t) + \boldsymbol{\beta}_i \dot{D}(t) \right] \tag{6.23}$$

where V(t) and $\dot{D}(t)$ are the velocity and pseudo-velocity responses of the SDF system. This is the solution for generalized modal time history analysis. Tsai and Kelly (1988) used this method to look at equipment response in base isolation buildings. They found that generalized modal analysis did a better job of capturing the response of higher modes.

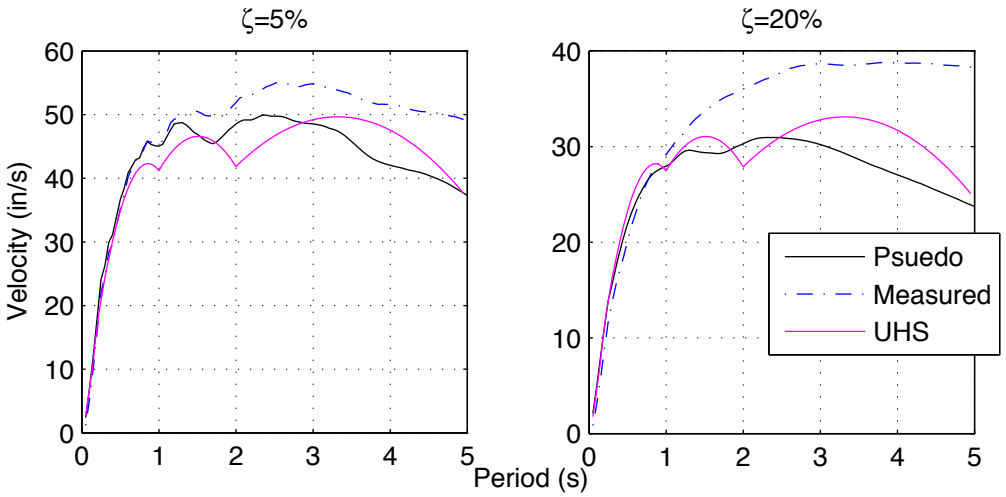

Figure 6.5 Mean pseudo-velocity and velocity spectra from the Oakland, CA ground motion set plotted with the pseudo-velocity uniform hazard spectra

The next step is to look at modal response spectrum analysis. For a classically damped system, the maximum response for each modal pair of frequency and damping ratio is found from the response spectrum and the results from the modes are combined using a modal combination method such as the square-root-of-the-sum-of-the-squares (SRSS) method. However, with generalized response spectrum analysis, the response of each mode is found by the addition of the responses related to both the velocity and pseudo-velocity. This presents two problems. Firstly, design codes specify the pseudo-acceleration spectrum, which is derived from the displacement spectrum. Thus, the pseudo-velocity spectrum can be derived conveniently, but the velocity spectrum is not available. Figure 6.5 shows the mean pseudo-velocity and velocity spectra from the 80 ground motion records used in the study. The spectra show that the greater the damping in the SDF system, the greater the difference in velocity and pseudo-velocity, especially at longer periods.

The second problem is that peak value of pseudo-velocity, which is directly related to displacement, does not occur at the same time as the peak value of velocity. As a result, the response of the mode cannot be found by simply adding the response due to the peak velocity and pseudo-velocity as might be suggested by Eq. 6.23.

One solution method involves making two assumptions. First, that the maximum values of pseudo-velocity and velocity are close enough to use only the value of pseudo velocity computed from the code spectrum or other pseudo-acceleration spectrum used in design and second, that the times at which the maximum values occur are distinct. With these assumptions, the SRSS combination rule can be used first with the responses due to velocity and pseudo-velocity within the mode to find the peak modal response and then the SRSS combination rule can be used to combine all modal responses and estimate the peak responses.

A more sophisticated combination method, originally developed to generate floor response spectra using modal response spectrum analysis, is presented by Igusa and Der Kiureghian (1985). The floor response spectrum is developed by placing a separate SDF oscillator on the floor where the spectra is desired. A separate analysis is done for each

desired response spectrum period. For each period desired, the oscillator properties are defined with the appropriate stiffness and mass and the maximum relative displacement of the oscillator is calculated. The pseudo-acceleration value is calculated from the maximum displacement. This method was developed to deal with three issues when using an oscillator degree of freedom to generate floor response spectra: (1) tuning, due to the oscillator having one of the natural frequencies of the structure, which results in amplification of estimated response, (2) interaction between the structure and oscillator systems, and (3) non-classical damping, which occurs when the damping of the oscillator system is different than that of the structure. This last issue is the same seen with modal response spectrum analysis for isolated structures; thus, this method is applicable to the isolation problem. This method is based on the same principals used by Der Kiureghian (1981) to develop the complete quadratic combination (CQC) rule for modal combination for classical modal response spectrum analysis. Hence, this method is referred to as generalized modal response spectrum analysis with CQC combinations.

In the method presented by Igusa and Der Kiureghian (1985), the mean of the peak response of the system is

$$p\sqrt{\lambda_0} \tag{6.24}$$

where p is the peak factor and λ_0 is the first spectra moment of the response where

$$\lambda_0 = \sum_i \sum_j \left[a_i a_j \rho_{0,ij} - (a_i c_j - a_j c_i)\eta_{1,ij} w_{1,ij} + c_i c_j \rho_{2,ij} w_{2,ij} \right] \frac{1}{p_i p_j} D_i D_j \tag{6.25}$$

where D_i is the displacement of the SDF system and

$$\mathbf{a_i} = \mathbf{q}\alpha_i \omega_i, \ \mathbf{c_i} = \mathbf{q}\beta_i \tag{6.26}$$

where $\mathbf{q}$ is vector length n where $\mathbf{q}^T\mathbf{x}$ gives the desired response quantity. The coefficients ρ, η and w and the peak factors p are given in the reference. This combination rule does not require the use of the velocity spectrum.

For the three-story building described in Section 6.1 with isolation system with T_{eff} = 3.42 s and ζ_{eff} = 0.2, the frequency and damping ratios and peak story drifts using classical modal analysis (CMA) and generalized modal analysis (GMA) with both SRSS and CQC combination rules are given in Table 6.3. GMA_{SRSS} and GMA_{CQC} do not differ

Table 6.3 Three-story isolated building frequency, damping and peak story drifts found with three modal response spectrum analyses

	CMA	GMA_{SRSS}	GMA_{CQC}
ω_1, ζ_1	3.46s, 0.2	3.45s, 0.19	3.45s, 0.19
ω_2, ζ_2	0.35s, 0.02	0.35s, 0.07	0.35s, 0.07
ω_3, ζ_3	0.19s, 0.02	0.19s, 0.04	0.19s, 0.04
ω_4, ζ_4	0.14s, 0.02	0.14s, 0.02	0.14s, 0.02
x_1	16.59 in	16.84 in	16.84 in
x_2	0.31 in	0.34 in	0.34 in
x_3	0.21 in	0.24 in	0.24 in
x_4	0.11 in	0.13 in	0.13 in

in method until the calculation of peak responses; however, for this system, calculated peak story drifts are the same for both methods. In the next section it is shown that both methods give very similar results for all the isolated building systems examined. CMA gives similar results for modal frequencies, but story drifts are less than calculated from the GMA methods.

6.3 Comparison of Results

To evaluate which method best predicts the peak responses of isolated buildings, the values of peak roof displacement and story shears are examined. The peak roof displacement is given by the ratio of the displacement between the roof and the isolation level to the height of the building. The story heights are assumed to be 12 ft. The story shears are defined as the peak inter-story drifts multiplied by the story stiffness. Thus, they indicate whether the three modal response spectrum analysis methods can predict displaced shapes and can capture higher mode effects.

The peak values for the roof drift index and story shears are presented from classical modal response spectrum analysis (CMA), generalized modal response spectrum analysis with SRSS combination (GMA_{SRSS}), generalized modal response spectrum analysis with CQC combination (GMA_{CQC}) and means of the maximum responses of the non-linear time-history for the buildings with linear bearings with viscous damping (LV) isolation system, single friction pendulum (SFP) isolation system and triple friction pendulum (TFP) isolation system.

Additionally, the first floor (immediately above the isolation system) and roof response spectra generated by GMA_{CQC} are compared against the mean first floor response spectra from the time-history analyses of the different systems. Due to amplification from tuning, classical modal response spectrums analysis and generalized modal response spectrums analysis with SRSS combinations cannot be used to accurately generate response spectra because of amplification of response as discussed by Igusa and Der Kiureghian (1985). When using GMA_{CQC} to generate floor spectra, the results are dependent on the ratio of oscillator mass to the structure; a ratio of 0.0002 was used in this study.

In the analysis presented here superposition of modal damping is used to represent damping in the superstructure with 2% damping assigned to all modes. For the CMA method, SRSS modal combination is used because of the large separation between isolation and building periods.

6.3.1 Displacements and shears

The peak roof drift ratios are listed in Table 6.4. CMA underestimates the roof drift for all isolation types and all building-isolation property combinations. GMA with either combination rule provides a good estimate to roof drift for the LV and TFP systems, either predicting or slightly underestimating the value. The LV and TFP systems had roughly the same roof drifts with the LV system having larger drifts for some building-isolation properties and smaller or equal drifts for others. The SFP system resulted in the highest roof drifts of the three isolation systems. The difference in drifts

between the isolation systems increases with increasing effective damping ratio. The largest difference is seen in the one-story building with bearings having 30% equivalent damping. In this configuration, the mean maximum roof drift in the SFP system is 65% larger than in the LV system and 85% larger than in the TFP system.

Peak isolator displacements are listed in Table 6.5. For damping greater than 10%, CMA predicts a lower displacement than the GMA methods. GMA methods predicted isolation displacements close to (or at) 18 in, which was the design displacement for all bearings. However, the LV bearing average displacement decreased with increasing bearing effective period. This has a simple explanation; Figure 6.1 shows that the mean of the ground motion spectra dips below the design spectra at larger periods. The SFP systems had consistently lower displacements than the equivalent LV systems, and the TFP systems had average displacements around 18 in, higher than the equivalent LV systems, but at the target displacement.

This shows a need for further investigation into equivalent linearization techniques. Iwan and Gates (1979) found that another method for finding the effective linear stiffness and viscous damping, referred to as the average stiffness and energy method, better predicted response of a non-linear single-degree-of-freedom system with ductility ratios of up to eight. Future study is necessary to determine which method for deriving effective properties results in best estimations of bearing response.

Table 6.4 Values of peak roof drift ratio for the one-, three- and nine-story buildings from modal response spectrum analyses and averages of time-history analyses

		Peak Roof % Drift Ratio (Relative to Isolation Level)					
		CMA	GMA_{SRSS}	GMA_{CQC}	LV	TFP	SFP
1 story	T=2.8s ζ=0.1	0.064	0.066	0.066	0.066	0.067	0.070
	T=3.42s ζ=0.2	0.043	0.047	0.047	0.046	0.045	0.063
	T=4.1s ζ=0.3	0.030	0.036	0.036	0.037	0.033	0.061
3 story	T=2.8s ζ=0.1	0.23	0.24	0.24	0.24	0.25	0.26
	T=3.42s ζ=0.2	0.15	0.17	0.17	0.17	0.17	0.21
	T=4.1s ζ=0.3	0.11	0.14	0.14	0.14	0.13	0.20
9 story	T=2.8s ζ=0.1	0.31	0.34	0.34	0.34	0.34	0.34
	T=3.42s ζ=0.2	0.21	0.25	0.24	0.24	0.24	0.26
	T=4.1s ζ=0.3	0.14	0.20	0.19	0.20	0.20	0.23

Table 6.5 Values of peak isolation level displacement for the one-, three- and nine-story buildings from modal response spectrum analyses and averages of time-history analyses

		Peak Isolation Level Displacement (in)					
		CMA	GMA_{SRSS}	GMA_{CQC}	LV	TFP	SFP
1 story	T=2.8s ζ=0.1	18.0	18.0	18.0	17.8	18.3	16.8
	T=3.42s ζ=0.2	18.0	18.0	18.0	15.8	17.8	15.8
	T=4.1s ζ=0.3	18.0	18.0	18.0	14.5	18.2	15.8
3 story	T=2.8s ζ=0.1	17.8	18.1	18.1	17.8	18.2	16.6
	T=3.42s ζ=0.2	17.8	18.0	18.0	15.7	17.7	16.5
	T=4.1s ζ=0.3	17.8	18.0	18.0	14.6	18.2	16.3
9 story	T=2.8s ζ=0.1	17.0	18.1	18.1	17.5	17.5	16.2
	T=3.42s ζ=0.2	17.1	18.1	18.1	15.6	17.5	15.5
	T=4.1s ζ=0.3	17.0	17.9	17.8	14.5	18.0	16.3

The maximum story shears are found by multiplying the maximum story drifts by the respective story stiffness, with the exception of the isolation layer of the TFP and SFP systems. These systems change effective stiffness with displacement and thus the maximum force can be found from the value of the bearing characteristic backbone curve at the maximum bearing displacement. The story shears are shown for the three building sizes in Figure 6.6 through Figure 6.8. Due to the variations in the design displacement spectrum and the mean of the ground motion spectra at high periods as discussed above, there is a distinct difference between the isolation level shears.

CMA does an acceptable job of predicting story shears for the lowest levels of damping in the isolation system. However, when the equivalent damping increases, CMA under predicts the story shears for all superstructure levels. GMA using either SRSS or CQC combinations rules does a much better job of predicting story shears in the LV and TFP systems, even predicting an amplification of shear force from the isolation level to the first floor level in the nine-story building with 30% damping isolation system. The LV system sees an amplification in shear from the isolation layer to first floor in the three-story building with 30% damping isolation and the nine-story with 20% and 30% damping isolation. These systems have larger contributions in behavior from higher mode effects that cannot be accounted for with CMA.

The SFP isolation system with higher damping is not well predicted by any modal response spectrum analysis method. With 30% equivalent damping there are major

amplifications in the story shear for all level buildings. Interestingly, the TFP and LV systems had similar results for maximum drifts and story shears. This shows that although further research is necessary on methods for deriving effective properties, global behavior of structures isolated with TFP bearings can be approximated by equivalent linear elastic systems with linear viscous damping with good results, as long as the hardening stages of the TFP are not reached.

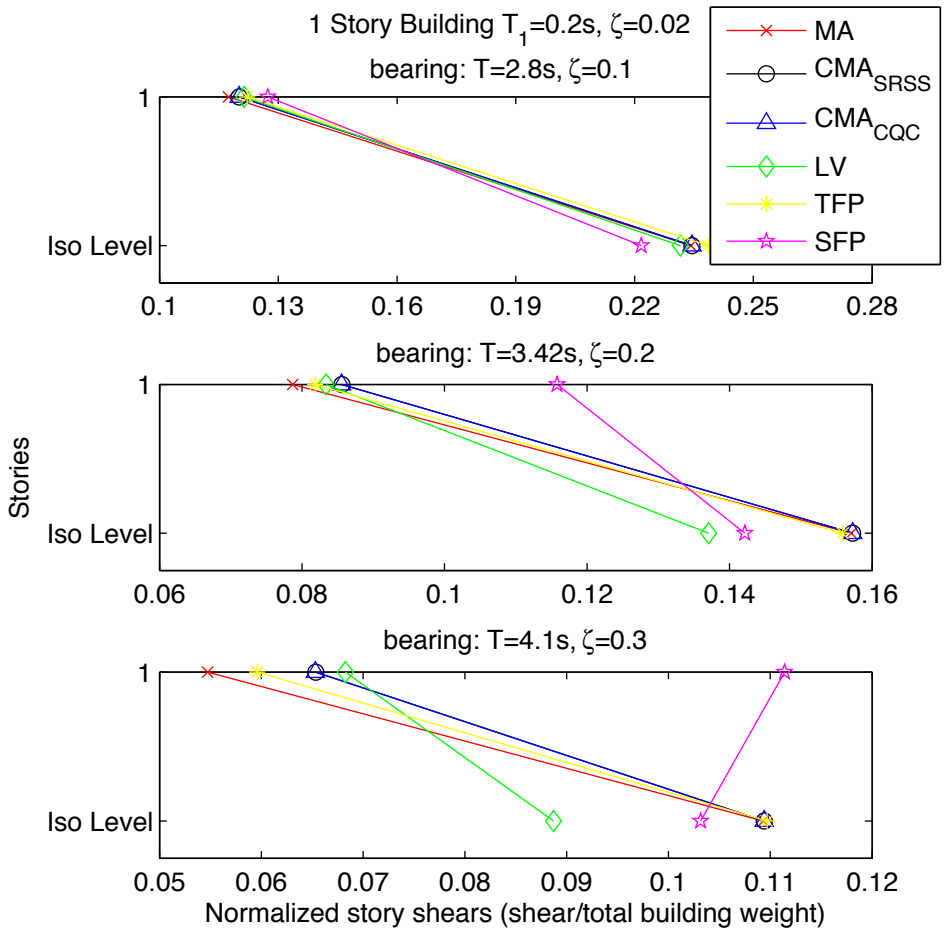

Figure 6.6 Maximum story shear forces normalized by building weight for a one-story isolated building from modal response spectrum analyses and time-history analyses

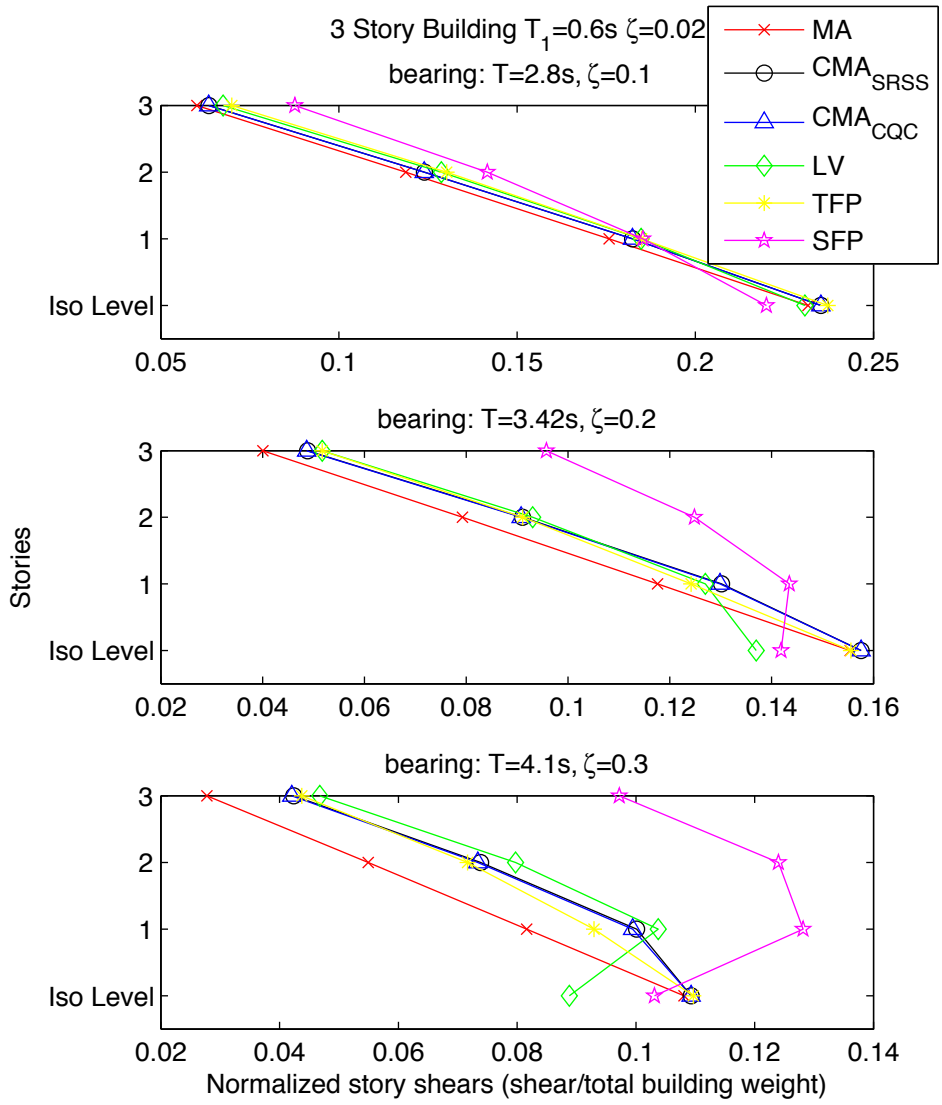

Figure 6.7 Maximum story shear forces normalized by building weight for a three-story isolated building from modal response spectrum analyses and time-history analyses

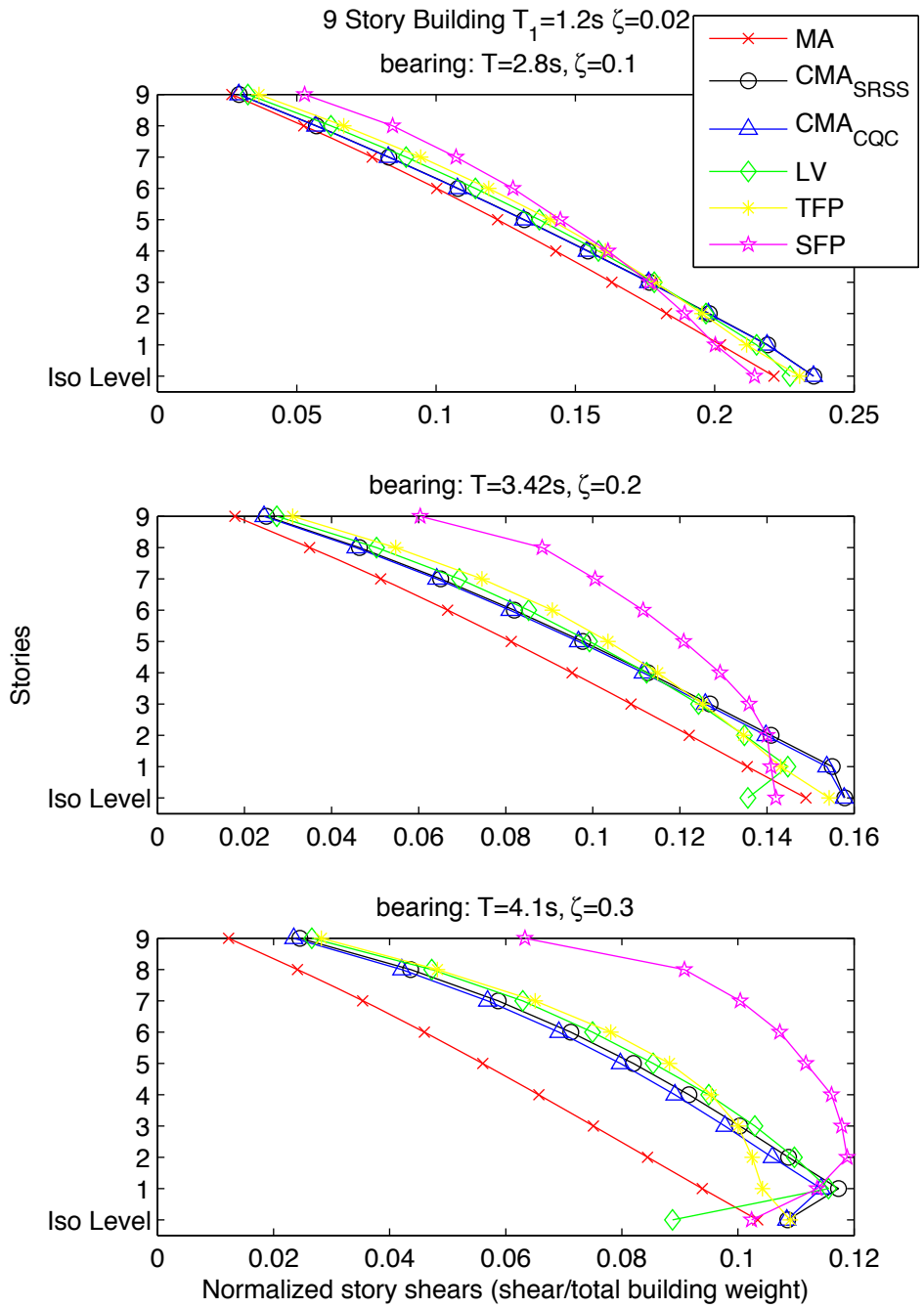

Figure 6.8 Maximum story shear forces normalized by building weight for a nine-story isolated building from modal response spectrum analyses and time-history analyses

6.3.2 Floor acceleration spectra

The first floor (directly above the isolation level) and roof level response spectra with 5% damping are given for the three building heights in Figure 6.9 through Figure 6.11. For frequencies higher than 2 Hz, the range for most equipment, the GMA method with CQC combinations does a remarkable job of predicting floor level accelerations for the LV system. The TFP system sees a small amplification from these values. Interestingly, the amplification is smaller for the larger damping systems, matching closely to the LV system for 30% damping in the range of the fixed-based building frequencies. Amplification at higher frequencies may be due to high initial stiffness in the friction systems. From a design standpoint the prediction from GMA could still be used to estimate the floor response spectra for a TFP isolated structure, perhaps with a safety factor.

At high periods near the isolation period, GMA still exhibits effects from tuning, particularly with the 10% damping isolation systems. Thus, floor accelerations at these periods are over-estimated using GMA but the method is useful for showing the general trend in amplification of accelerations in this period range for isolations systems with low damping. As with the displacements and forces, the floor acceleration spectra cannot be well predicted for the SFP system. The accelerations are considerably larger in the short period/ high frequency range and smaller in the long period/ low frequency range.

The ability of GMA to estimate the behavior of buildings supported by LV and TFP isolators has great potential to facilitate in the design of isolated buildings and could be used to optimize isolator parameters to achieve better structural performance. This study has already shown that gradual yielding behavior (as seen in the TFP bearing as opposed to the SFP bearing) decreases shear forces in the superstructure as well as floor accelerations. This suggests that the friction coefficients of the TFP bearing should be well spaced. In future studies, GMA estimations of building responses should be validated against full-scale numerical building analyses.

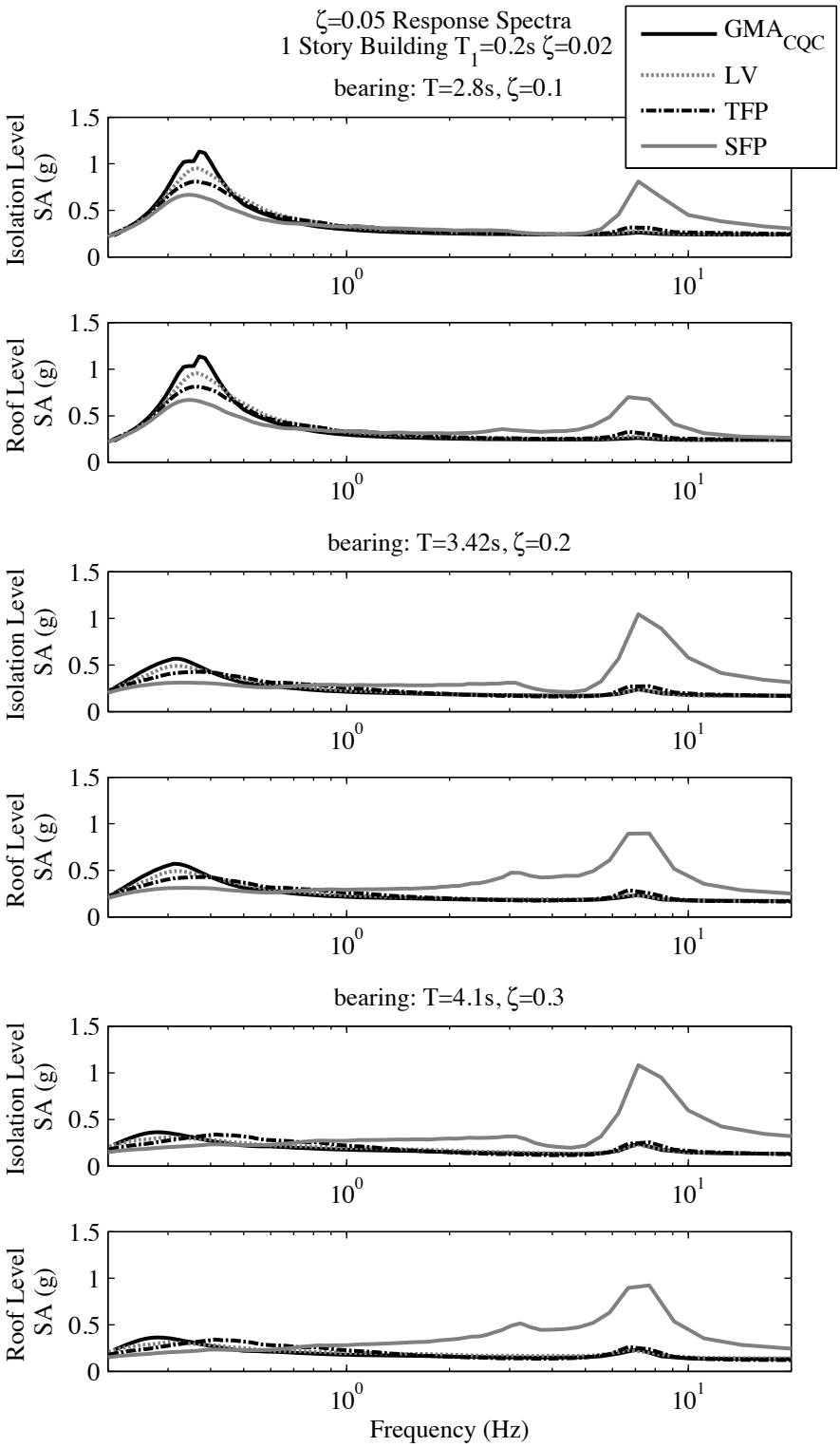

Figure 6.9 Floor response spectra for a one-story isolated building from generalized modal response spectrum analysis with CQC combination and time-history analyses

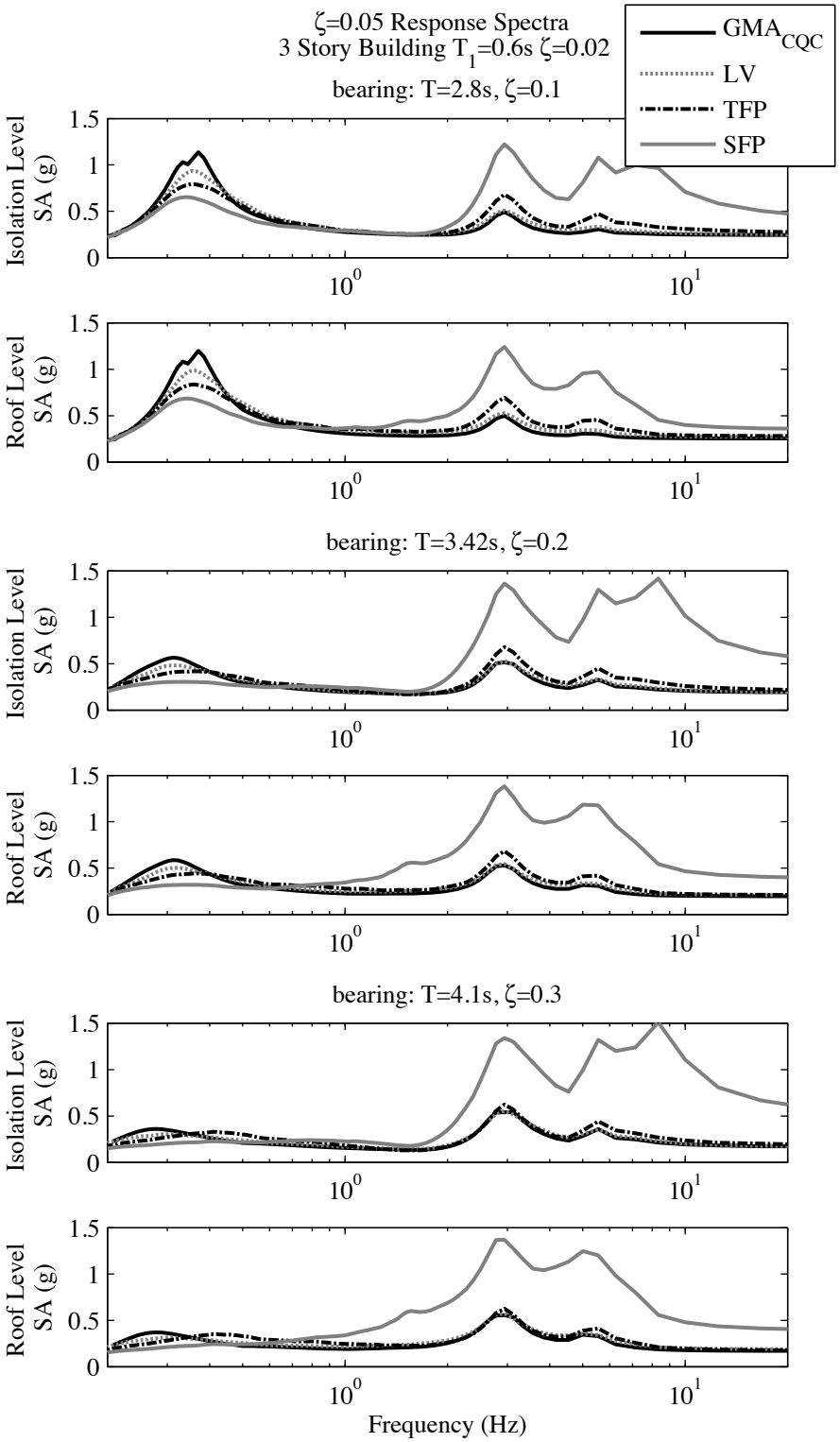

Figure 6.10 Floor response spectra for a three-story isolated building from generalized modal response spectrum analysis with CQC combination and time-history analyses

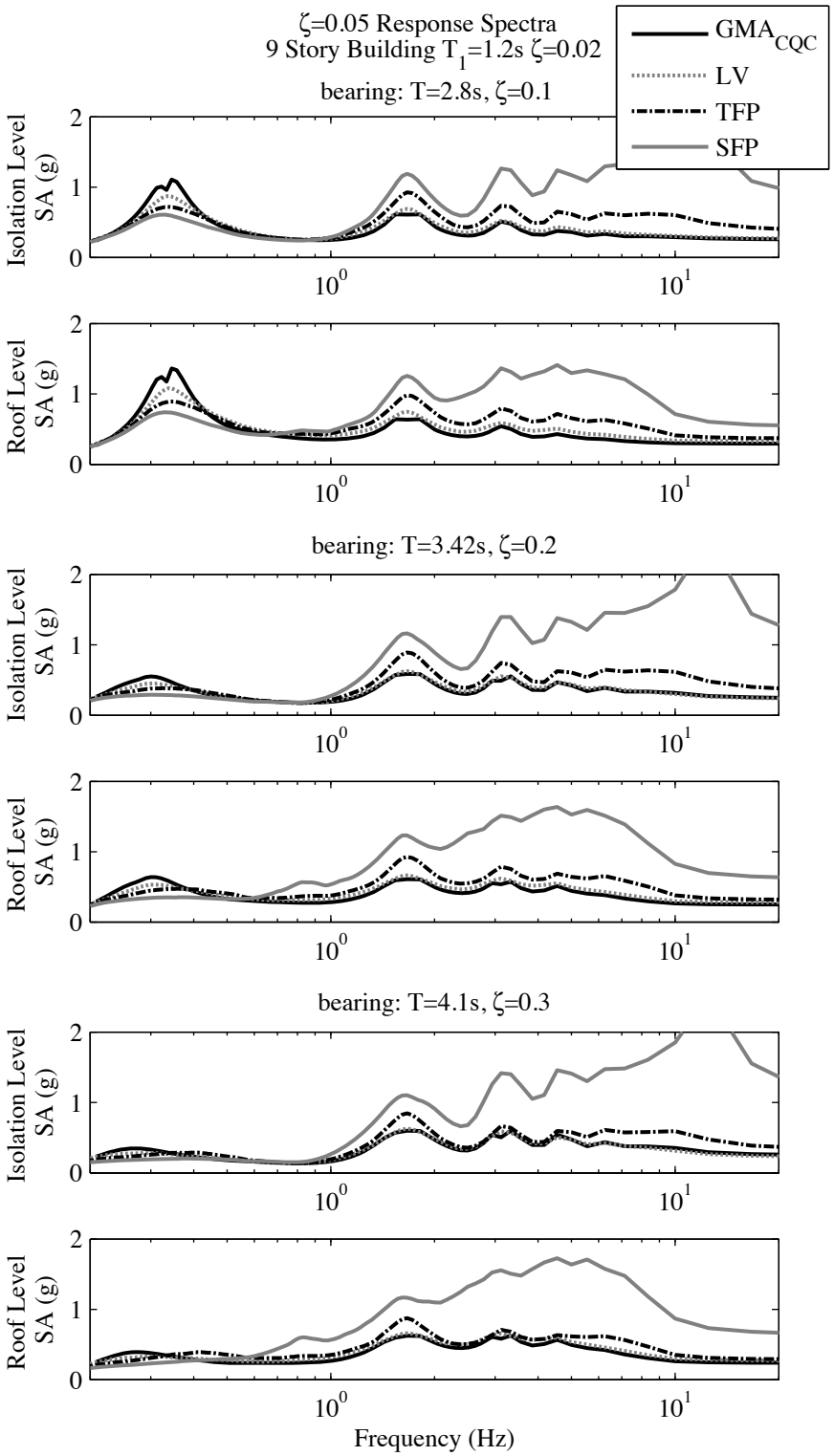

Figure 6.11 Floor response spectra for a nine-story isolated building from generalized modal response spectrum analysis with CQC combination and time-history analyses

7 Conclusions and Recommendations

This dissertation investigates advanced modeling techniques for the triple friction pendulum (TFP) seismic isolation bearing in support of performance-based design (PBD). Two types of approaches were explored. In one approach, the complex inelastic behavior of the TFP bearing was realistically modeled based on the kinematic and compatibility relationships of the bearing components. This model can be used to explore and validate the use of TFP technology in novel applications, examine the effects of nonstandard bearing properties, or confirm the achievement of project-specific performance objectives. In the other approach, a simplified modal analysis method (the generalized model response spectrum method) was identified and validated. This simplified method can be used to aid in the selection of appropriate isolator characteristics able to achieve targeted engineering response criteria for a given level of seismic hazard as well as to reduce the need for nonlinear time history analyses for a broader range of isolated buildings than permitted now.

7.1 Conclusions

7.1.1 Bidirectional characterization and modeling of TFP bearings

The TFP bearing is a complex sliding bearing with four stacked spherical sliding surfaces. Numerical modeling was conducted for two end-condition scenarios. The first, which represents end conditions for standard applications of isolation bearings, restricts the global rotation of the bearing about the horizontal axes. The second releases the rotational restraints allowing the top and bottom supports of the bearing to both rotate and translate. With both end conditions, the bearing may rotate about the vertical axis, however, there is no restraining force associated with this motion. Unlike previous models, the advanced models presented herein are based directly upon the kinematics and compatibility of the sliding surfaces. This has two advantages: (a) there are no constraints on the geometric or friction characteristics for which the model is valid and (b) all local slider displacements are known at any given time. Since all local displacements and velocities are known, the model can be modified to have velocity, pressure or temperature dependent frictional properties that are characterized specifically for each sliding surface. Another advantage to tracking the local slider displacements is that the change in bearing height can be calculated at any time.

Displacement-controlled and unrestrained tests were run using the shake table at the University of California, Berkeley. The experiments used a rigid block supported on four scale model TFP bearings. The superstructure model in the experimental setup was kept deliberately simple to focus on only the TFP bearing behavior and not the interaction

of the isolation system with the superstructure. For the displacement-controlled tests, struts were used to brace the rigid block above the isolators to rigid reaction blocks positioned off of the shake table. The table was then used as a bearing-test machine and the bearings were cycled through horizontal sine, circle, square and figure eight motions as well as offset sine and offset circle motions in order to reach larger displacements. The data gathered from the displacement-controlled tests were used to validate the bidirectional behavior of the TFP model. First, the TFP model needed to be calibrated using the friction coefficients found experimentally with sine wave test data. Once the model was calibrated, bearing hystereses, force paths and change in bearing height were compared, and it was shown that the advanced model was able to capture the bearing behavior.

From these studies of TFP bearing, the following conclusions can be made:

1. In the unrestrained tests, it was observed that the model tended to predict displacements somewhat larger than observed in the tests, yet, the shape of the orbits as well as the range of transmitted forces were accurate. In addition, the floor response spectra generated from the numerical simulations compared well to the spectra generated from acceleration data recorded during the experiments.
2. From the experimental studies, it was shown that the bidirectional behavior of the TFP can be approximated from unidirectional input, and that vertical excitations that cause no uplift do not have a significant effect on the horizontal response.
3. It was shown through both experimental and numerical studies that initial slider offsets or small initial bearing offsets affect only the ultimate behavior of the TFP bearing, and therefore should not be of concern for the majority of TFP bearing applications.
4. An advantage of friction pendulum systems is that its behavior is not sensitive to torsion. Because the horizontal stiffness of the friction pendulum bearings is axial load dependent, when the center of mass is shifted over a friction pendulum system, the center of rigidity is shifted by the same amount, resulting in zero eccentricity. Unrestrained rigid block tests showed that there were no significant changes in system behavior when the supported mass was shifted relative to the center of bearings.
5. When a TFP bearing is placed on a flexible column, the stiffness and strength of the bearing decreases with the increase in flexibility of the column. In addition, some of all of the ultimate stages of behavior are surpressed. However, earthquake simulations of the system showed that column flexibility does not have a large effect on the global response. Still, it is of utmost importance that the column is designed to accommodate the displacements and rotations due to the shear forces and large P-Δ moments transmitted through the bearing.

7.1.2 Generalized modal analysis methods

As well as exploring innovative uses of TFP bearings, the TFP model can be used to validate simplified methods for approximating dynamic responses in buildings with typical use of isolations systems. This dissertation used time history analyses carried out with the TFP model to validate a quick method to approximate responses of buildings

with typical base-isolation design in which there are rigid diaphragms above and below the isolation layer. Building responses examined included displacements, shear forces and floor response spectra. Buildings of three different heights, each with its own respective predominant period, were used in the comparisons. Each building was isolated with three isolation systems having different pairs of equivalent period and damping, amounting to a total of nine configurations. Both classical modal response spectrum analysis (CMA) and generalized modal response spectrum analyses (GMA) were used to predict story drifts and the resulting story shears for the nine configurations. For comparison, eighty time history analyses were run for the configurations, using linear bearings with linear viscous damping, single friction pendulum (SFP) bearings and TFP bearings.

Based on these studies, it can be concluded:

1. GMA outperformed the CMA for approximating building response and that approximations from CMA became worse with increasing damping in the isolation layer.
2. GMA very accurately predicted the responses for the buildings isolated on linear viscous systems as well as on TFP systems. However, the responses in the building isolated by SFP bearings were significantly higher than in the other two systems and could not be well predicted by either type of modal response spectrum analysis.
3. In addition to the displacements and shear forces, it was found that the GMA was able to approximate floor response spectra for the linear viscous and TFP bearing isolated buildings.
4. Design using without nonlinear time history analysis is permitted for only a small range of combinations of bearing and building properties in the design code in the United States. GMA approximations proved accurate over a much larger range of these properties. Thus, GMA has the potential to be used as a design tool for a broad range of isolated buildings, decreasing the need for costly nonlinear time history analyses.
5. GMA could be used as a tool in optimizing bearing design to reduce displacements, story drifts and floor accelerations.

7.2 Recommendations for Future Research

There are still many behavioral characteristics of the TFP bearing that remain to be investigated including:

1. The effect of nonuniform pressure distributions on the sliding surfaces.
2. The effect of rotation about the vertical axis of the bearing or rotation of the sliders about their respective vertical axes.
3. A more detailed investigation into vertical accelerations transmitted through the bearing and the effect of fluctuating axial loads on bearing behavior.
4. The effect of differential vertical displacements of TFP bearings supporting statically indeterminate superstructures.
5. Behavior of the bearing and its inner components during uplift.

To study these characteristic effects, a more advanced test setup that can track

displacement and rotation of all individual bearing components during complex motion is needed.

To take advantage of the adaptive characteristics of the TFP bearings in PDB, more detailed studies are needed to identify optimal characteristics and combinations of TFP bearings and structural systems considering desired engineering demand parameters.

A potential application of the advanced TFP model is in research that examines the ultimate behavior of isolated buildings. Recent large earthquakes showed that there is an immediate need to investigate the behavior, damage, and ultimate capacity of isolated building structures under extreme loading. It is necessary to introduce a capacity based design approach to the design of isolated buildings. Currently, isolated buildings in the US are required to remain nearly elastic for a design basis earthquake and have a displacement capacity for a maximum considered earthquake. However, there is no methodology to provide guidance on whether superstructure yielding, isolator failure or moat impact should occur first. A major question is: is it better to let a structure yield in order to reduce isolator displacements and limit damage to the isolation level or to design the superstructure to remain elastic beyond the ultimate force of the isolator? The TFP bearing and the crystallized rubber bearing offer a third option. Both bearings exhibit hardening behavior as they reach ultimate displacement. This hardening may be utilized for two purposes: first, to reduce the velocity of the building at impact and secondly to allow controlled yielding in the building immediately before impact. If damage can be controlled during extreme loading, some isolated buildings may be allowed to impact or yield in maximum considered events while still providing enhanced performance compared to fixed-base counterparts during service and design level events. Within a performance-based earthquake engineering framework, further research is needed to make informed decisions regarding the ultimate behavior design of isolated buildings.

References

American Society of Civil Engineers (2005). *Minimum Design Loads for Buildings and Other Structures.* Standard ASCE/ SEI 7-05, Reston, VA.

Anderson, E.L. (2003). *Performance-Based Design of Seismically Isolated Bridges.* Doctoral Dissertation, University of California, Berkeley.

Aschheim, M. and Black, E.F. (2000). "Yield point spectra for seismic design." *Earthquake Spectra*; **16**(2): 317-335.

Aslani, H. and Miranda, E. (2005). *Probabilistic Earthquake Loss Estimation and Loss Diasaggregation in Buildings,* Report No. BLUME 157, John A. Blume Engineering Center, Stanford University, Stanford, CA.

Baker, J.W., Lin, T., Shahi, S.K. and Jayaram, N. (2011). *New Ground Motion Selection Procedures and Selected Motions for the PEER Transportation Research Program,* Report No. PEER 11/03, Pacific Earthquake Engineering Research Center, University of California, Berkeley, CA.

Brookshire, D.S., Chang, S.E., Cochrane, H., Olson, R.A., Rose, A., and Steenson, J. (1997). "Direct and indirect economic losses from earthquake damage," *Earthquake Spectra,* **14**(4): 683-701.

Chopra, A.K. (2007). *Dynamics of Structures: Theory and Applications to Earthquake Engineering.* 3rd Ed. New Jersey: Prentice Hall.

Constantinou, M.C., Mokha, A. and Reinhorn, A.M. (1990). "Teflon bearings in base isolation. II: Modeling," *Journal of Structural Engineering,* ASCE, 116 (2), 455-474.

Contantinou, M.C., Tsopelas, P., Kasalanati, A. and Wolkk, E.D. (1999). *Property Modification Factors for Seismic Isolation Bearings.* Report No. MCEER 99-12, Multidisciplinary Center for Earthquake Engineering Research, Buffalo, New York.

Der Kiureghian, A. (1981). "A response spectrum method for random vibration analysis of MDF structures." *Earthquake Engineering and Structural Dynamics,* **9**: 419-435.

Fadi, F. and Constantinou, M.C. (2010). "Evaluation of simplified methods of analysis for structures with triple friction pendulum isolators." *Earthquake Engineering and Structural Dynamics,* **39**(1): 5-22.

Fenz, D.M. and Constantinou, M.C. (2007a). "Spherical sliding isolation bearings with adaptive behavior: Theory." *Earthquake Engineering and Structural Dynamics*, **37**(2): 163-183.

Fenz, D.M. and Constantinou, M.C. (2007b). "Spherical sliding isolation bearings with adaptive behavior: Experimental verification." *Earthquake Engineering and Structural Dynamics*, **37**(2): 185-205.

Fenz, D.M. and Constantinou, M.C. (2008a). "Modeling triple friction pendulum bearings for response-history analysis." *Earthquake Spectra*; **24**(4): 1011-1028.

Fenz, D.M. and Constantinou, M.C. (2008b). *Development, Implementation, and Verification of Dynamic Analysis Models for Multi-Spherical Sliding Bearings.* Report No. MCEER 08-18, Multidisciplinary Center for Earthquake Engineering Research, Buffalo, New York.

Harris, H.G., and Sabnis, G.M. (1999). *Structural Modeling and Experimental Techniques.* 2nd Ed. New York: CRC Press.

Higashino, M. and Okamoto, S. (eds) (2006). *Response Control and Seismic Isolation of Buildings.* New York: Taylor & Francis.

Igusa, T. and Der Kiureghian, A. (1985). "Generalization of floor spectra including oscillator-structure interaction." *Earthquake Engineering and Structural Dynamics*, **13**: 661-676.

Igusa, T., Der Kiureghian, A. and Sackman, J.L. (1984). "Modal decomposition method for stationary response of non-classically damped systems." *Earthquake Engineering and Structural Dynamics*, **12**: 121-136.

Iwan, W.D. and Gates, N.C. (1979). "Estimating earthquake response of simple hysteretic structures." *Journal of the Engineering Mechanics Division*, **105**(3): 391-405.

Jangis, R.S. and Kelly, J.M. (2000). "Torsional displacements in base-isolated buildings." *Earthquake Spectra*; **16**(2): 443-454.

Kelly, J.M. (1999). "The role of damping in seismic isolation." *Earthquake Engineering and Structural Dynamics* **28**, 3-20.

Kelly, J.M. and Konstantinidis, D. (2011). *Mechanics of Rubber Bearings for Seismic and Vibration Isolation.* New York: John Wiley & Sons.

Kikuchi, M., Black, C.J. and Aiken, I.D. (2008). "On the response of yielding seismically isolated structures." *Earthquake Engineering and Structural Dynamics* **37**, 659-679.

Konstantinidis, D., Kelly, J.M. and Makris, N. (2008). *Experimental Investigations on the Seismic Response of Bridge Bearings.* Report EERC 08-02. Earthquake Engineering Research Center, Berkeley, CA.

Mayes, R.L. (2002). "Impediments to the implementation of seismic isolation," *Proceedings of the ATC-17-2 Seminar on Response Modification Technologies for Performance-Based Seismic Design*, May 30–31, 2002, Los Angeles, CA.

Mitrani-Reiser, J. (2007). *An Ounce of Prevention: Probabilistic Loss Estimation of Performance-Based Earthquake Engineering.* Report No. EERL 2007-01, Earthquake engineering Research Laboratory, California Institute of Technology, Pasadena, CA.

Mokha, A., Constantinou, M.C. and Reinhorn, A.M. (1991). "Further results on frictional properties of teflon bearings under triaxial load," *Journal of Structural Engineering*, ASCE, 199 (1), 240-261.

Morgan, T.A. and Mahin, S.A. (2008). "The optimization of multi-stage friction pendulum isolators for loss mitigation considering a range of seismic hazard." *Proceedings of the 14th World Conference on Earthquake Engineering*. Beijing, China.

Morgan, T.A. (2008). *The Use of Innovative Base Isolation Systems to Achieve Complex Seismic Performance Objectives.* Doctoral Dissertation, University of California, Berkeley.

Morgan, T.A. and Mahin, S.A. (2010). "Achieving reliable seismic performance enhancement using multi-stage friction pendulum isolators." *Earthquake Engineering and Structural Dynamics*; **39**(13): 1443-1461.

Mosqueda, G., Whittaker A.S. and Fenves, G.L. (2004a). "Characterization and modeling of friction pendulum bearings subject to multiple components of excitation," *Journal of Structural Engineering*; **130**(3): 433:442.

Mosqueda, G., Whittaker A.S., Fenves, G.L. and Mahin, S.A. (2004b). *Experimental and Analytical Studies of the Friction Pendulum System for the Seismic Protection of simple Bridges.* Report EERC 04-01. Earthquake Engineering Research Center, Berkeley, CA.

Naeim, F. and Kelly, J.M. (1999). *Design of Seismic Isolated Structures: From Theory to Practice.* New York: John Wiley & Sons.

Pan, P., Zamfirescu, D., Nakashima, M., Nakayasu, N. and Kashiwa, H. (2005). "Base-isolation design practice in Japan: Introduction to the post-Kobe approach," *Journal of Earthquake Engineering*, **9**(1), 147:171.

Pan, T.C. and Kelly, J.M. (1983). “Seismic response of torsionally coupled base isolated structures.” *Earthquake Engineering and Structural Dynamics*, **11**: 749-770.

Politopoulos, I. (2008). “A review of adverse effects of damping in seismic isolation.” *Earthquake Engineering and Structural Dynamics*; **37**: 447-465.

Politopoulos, I. and Pham, H.K. (2009). “Sensitivity of seismically isolated structures.” *Earthquake Engineering and Structural Dynamics*; **38**: 989-1007.

Rabinowicz, E. (1995). *Friction and Wear of Materials.* New York: John Wiley & Sons.

Ryan, K.L. and Polanco, J. (2008). “Problems with Rayleigh damping in base-isolated buildings”, Technical Note, *Journal of Structural Engineering*, **134**(11): 1780-1784.

SAC Steel Project.
<http://nisee.berkeley.edu/data/strong_motion/sacsteel/ground_motions.html>

Scheller, J. and Constantinou, MC. (1999). *Response History Analysis of Structures with Seismic Isolation and Energy Dissipation Systems: Verification Examples for Program SAP2000.* Report No. MCEER 99-02. Multidisciplinary Center for Earthquake Engineering Research, Buffalo, New York.

Simo, J. and Hughes T. (2000). *Computational Inelasticity (Interdisciplinary Applied Mathematics)*, New York: Springer.

Tsai, C.S., Lin, Y.C. and Su, H.C. (2010). “Characterization and modeling of multiple friction pendulum isolation system with numerous sliding interfaces.” *Earthquake Engineering and Structural Dynamics*, **39**(11): 1463-1491.

Tsai, H.C. and Kelly, J.M. (1988). “Non-classical damping in dynamic analysis of base-isolated structures with internal equipment.” *Earthquake Engineering and Structural Dynamics*, **16**: 29-43.

Tsai, H.C. and Kelly, J.M. (1989). “Dynamic parameter identification for non-linear isolation systems in response spectrum analysis.” *Earthquake Engineering and Structural Dynamics*, **18**: 1119-1132.

Veletsos, A.S. and Ventura, C.E. (1986). “Modal analysis of non-classically damped linear systems.” *Earthquake Engineering and Structural Dynamics*; **14**: 217-243.

Yang, T.Y., Konstantinidis, D. and Kelly, J.M. (2010). “The influence of isolator hysteresis on equipment performance in seismic isolated buildings.” *Earthquake Spectra* **26**, 275-293.

Yang, T.Y., Moehle, J., Stojadinociv, B., Der Kiureghian, A. (2006). "An application of PEER performance-based earthquake engineering methodology." *Proceedings of the 8th U.S. National Conference on Earthquake Engineering*, April 18–22, 2006, San Francisco, CA.

Zayas, V.A., Low, S.S., Mahin, S.A. (1987). *The FPS Earthquake Resisting System.* Report No. EERC 87-01. Earthquake Engineering Research Center, Berkeley, CA.

Zayas, V.A., Low, S.S., Bozzo, L. Mahin, S.A. (1989). *Feasibility and Performance Studies on Improving the Earthquake Resistance of New and Existing Buildings Using the Friction Pendulum System.* Report No. EERC 89-09. Earthquake Engineering Research Center, Berkeley, CA.

Appendix A Table Motions

Controlled-Displacement Motions

Motions not run at a peak velocity of 6 in/s (with the exception of the sine wave motions with growing velocity) are noted.

Test	*Log Number*	*Signal*	*Max Disp (in)* [*X, Y, Z*]
1	20081028 151554	Sine Wave (3 in/s)	[0,2.5,0]
2	20081028 152126	Sine Wave (3 in/s)	[0,5,0]
3	20081028 160603	Sine Wave (3 in/s)	[0,5,0]
4	20081029 160641	Figure Eight (bearing run-in)	[5,5,0]
5	20081029 161045	Figure Eight (bearing run-in)	[5,5,0]
6	20081029 164537	Figure Eight (bearing run-in)	[5,5,0]
7	20081029 170434	Sine Wave (3 in/s)	[0,5,0]
8	20081029 170830	Sine Wave	[0,5,0]
9	20081029 171300	Sine Wave (9 in/s)	[0,5,0]
10	20081029 171944	Circle	[5,5,0]
11	20081029 172337	Square	[5,5,0]
12	20081029 173428	Figure Eight	[5,5,0]
13	20081029 173914	Sine Wave with growing velocity	[0,0.2,0]
14	20081029 174107	Sine Wave with growing velocity	[0,1,0]
15	20081029 174352	Sine Wave with growing velocity	[0,3.5,0]
16	20081030 113353	Sine Wave with growing velocity	[0,0.5,0]
Rigid Block Offset 2.5 inches in negative *Y* Direction			
17	20081103 170846	Sine Wave	[0,4.5,0]
18	20081103 171805	Sine Wave	[0,4.75,0]
19	20081103 172620	Sine Wave	[0,5,0]
20	20081103 173755	Figure Eight (bearing run-in)	[5,5,0]
21	20081103 174142	Figure Eight (bearing run-in)	[5,5,0]
22	20081103 174702	Sine Wave	[0,5,0]
23	20081103 175145	Circle	[5,5,0]

Unrestrained Motions

Test	*Log Number*	*Signal*	*Recent-ered*	*Length Scale*	*Amp. Factor*	*Max Disp. (in)* [*X, Y, Z*]
24	20081104 155634	Sine Wave, T=0.4s	Yes	-	-	[0,0.5,0]
25	20081104 160138	Sine Wave, T=0.4s	No	-	-	[0,2,0]
26	20081104 161749	Sine Wave, T=1.0s	Yes	-	-	[0,2,0]
27	20081104 162026	Sine Wave, T=1.0s	No	-	-	[0,3.5,0]
28	20081104 164629	Sine Wave, T=1.4s	Yes	-	-	[0,2,0]
29	20081104 164930	Sine Wave, T=1.4s	No	-	-	[0,3.5,0]
30	20081104 165811	Sine Wave, T=1.0s	No	-	-	[0,5,0]
31	20081104 170519	Kobe, JMA	Yes	2	25%	[1.73,1.63.0]
32	20081104 171105	Northridge, Newhall	Yes	2	50%	[1.81,2,32,0]
33	20081104 171923	Tabas	No	2	25%	[2.11,2.06,0]
34	20081104 172455	Northridge, Sylmar	No	2	50%	[2.61,0.83,0]
35	20081104 173012	Kobe, JMA	No	2	50%	[3.47,3.27,0]
36	20081104 173925	Northridge, Newhall	Yes	2	100%	[3.63,3.27]
37	20081104 174501	Tabas	Yes	2	50%	[4.21,0,0]
38	20081104 174922	Tabas	No	2	50%	[4.21,4.12,0]
39	20081104 175603	Tabas	No	2	50%	[4.21,4.12,0.9]
40	20081104 180408	Tabas	Yes	2	50%	[4.21,4.12,1.13]
41	20081104 181201	Tabas	Yes	2	50%	[4.21,0,1.13]
42	20081104 181846	Northridge, Sylmar	Yes	2	44%	[4.59,1.45,0]
43	20081104 182422	Kobe, JMA	Yes	2	65%	[4.51,4.25,0]
44	20081104 182749	Kobe, JMA	No	2	65%	[4.51,0,0]
45	20081104 182922	Kobe, JMA	No	2	65%	[0,4.25,0]
46	20081105 152732	Kobe, JMA	Yes	3	85%	[4.01,3.63,0]
47	20081105 153315	Kobe, JMA	Yes	3	100%	[4.72,4.27,0]
48	20081105 153942	Tabas	Yes	3	68%	[4.72,4.27,1]
49	20081105 154755	Tabas	Yes	3	65%	[4.48,4.65,1]
50	20081105 160700	Northridge, Sylmar	Yes	3	70%	[4.95,1.53,0]
51	20081105 161243	Kobe, JMA	Yes	4	100%	[3.57,3.17,0]
52	20081105 161811	Kobe, JMA	Yes	4	120%	[4.28,3.81,0]

53	20081105	163024	Tabas	Yes	4	80%	[4.14,4.82,0.87]
54	20081105	163700	Northridge, Sylmar	Yes	4	90%	[4.76,1.46,0]
55	20081105	164838	Northridge, Sylmar	Yes	5	100%	[4.23,1.29,0]
56	20081105	165301	Northridge, Sylmar	Yes	5	115%	[4.87,1.49,0]
57	20081105	165832	Northridge, Sylmar	Yes	5	118%	[5,1.53,0]
58	20081105	172848	Sine Wave, T=1.0s	Yes	-	-	[0,5,0]

Appendix B Instrumentation

Instrumentation List

Channel	*Label*	*Transducer*	*Response Quantity*	*Orientation*	*Location*
1	date	-	date	-	-
2	time	-	time	-	-
3	H1O	LVDT	displacement	X	simulator platform
4	H2O	LVDT	displacement	Y	simulator platform
5	H3O	LVDT	displacement	X	simulator platform
6	H4O	LVDT	displacement	Y	simulator platform
7	V1O	LVDT	displacement	Z	simulator platform
8	V2O	LVDT	displacement	Z	simulator platform
9	V3O	LVDT	displacement	Z	simulator platform
10	V4O	LVDT	displacement	Z	simulator platform
11	H1-2	ACC	acceleration	X	simulator platform
12	H3-4	ACC	acceleration	Y	simulator platform
13	H4-1	ACC	acceleration	X	simulator platform
14	H2-3	ACC	acceleration	Y	simulator platform
15	V1ACC	ACC	acceleration	Z	simulator platform
16	V2ACC	ACC	acceleration	Z	simulator platform
17	V3ACC	ACC	acceleration	Z	simulator platform
18	V4ACC	ACC	acceleration	Z	simulator platform
19	TblAcc9	ACC	acceleration	X	simulator platform - top
20	TblAc10	ACC	acceleration	Y	simulator platform - top
21	TblAc11	ACC	acceleration	Z	simulator platform - top
22	LC11	load cell	shear	X	bearing 1 SE
23	LC12	load cell	shear	Y	bearing 1 SE
24	LC13	load cell	moment	X	bearing 1 SE
25	LC14	load cell	moment	Y	bearing 1 SE
26	LC15	load cell	axial force	Z	bearing 1 SE
27	LC21	load cell	shear	X	bearing 2 NE
28	LC22	load cell	shear	Y	bearing 2 NE
29	LC23	load cell	moment	X	bearing 2 NE
30	LC24	load cell	moment	Y	bearing 2 NE
31	LC25	load cell	axial force	Z	bearing 2 NE
32	LC33	load cell	shear	Y	bearing 3 NW
33	LC34	load cell	moment	X	bearing 3 NW

34	LC35	load cell	moment	Y	bearing 3 NW
35	LC41	load cell	axial force	Z	bearing 3 NW
36	LC42	load cell	shear	X	bearing 4 SW
37	LC43	load cell	shear	Y	bearing 4 SW
38	LC44	load cell	moment	X	bearing 4 SW
39	LC45	load cell	moment	Y	bearing 4 SW
40	LC31	load cell	axial force	Z	bearing 4 SW
41	TPdis11	DCDT	displacement	X	bearing 1 SE - bottom
42	TPdis12	DCDT	displacement	Y	bearing 1 SE - bottom
43	TPdis21	DCDT	displacement	X	bearing 2 NE - bottom
44	TPdis22	DCDT	displacement	Y	bearing 2 NE - bottom
45	TPdis31	DCDT	displacement	X	bearing 3 NW - bottom
46	TPdis32	DCDT	displacement	Y	bearing 3 NW - bottom
47	TPdis41	DCDT	displacement	X	bearing 4 SW - bottom
48	TPdis42	DCDT	displacement	Y	bearing 4 SW - bottom
49	TPacc11	ACC	acceleration	X	bearing 1 SE - bottom
50	TPacc12	ACC	acceleration	Y	bearing 1 SE - bottom
51	TPacc13	ACC	acceleration	Z	bearing 1 SE - bottom
52	TPacc14	ACC	acceleration	Z	bearing 1 SE - top
53	TPacc21	ACC	acceleration	X	bearing 2 NE - bottom
54	TPacc22	ACC	acceleration	Y	bearing 2 NE - bottom
55	TPacc23	ACC	acceleration	Z	bearing 2 NE - bottom
56	TPacc24	ACC	acceleration	Z	bearing 2 NE - top
57	TPacc31	ACC	acceleration	X	bearing 3 NW - bottom
58	TPacc32	ACC	acceleration	Y	bearing 3 NW - bottom
59	TPacc33	ACC	acceleration	Z	bearing 3 NW - bottom
60	TPacc34	ACC	acceleration	Z	bearing 3 NW - top
61	TPacc41	ACC	acceleration	X	bearing 4 SW -

					bottom
62	TPacc42	ACC	acceleration	Y	bearing 4 SW - bottom
63	TPacc43	ACC	acceleration	Z	bearing 4 SW - bottom
64	TPacc44	ACC	acceleration	Z	bearing 4 SW - top
65	FramDX1	POT	displacement	X	steel frame
66	FramDY1	POT	displacement	Y	steel frame
67	FramDX2	POT	displacement	X	steel frame
68	FramDY2	POT	displacement	Y	steel frame
69	FramDZ1	POT	displacement	Z	steel frame
70	FramDZ2	POT	displacement	Z	steel frame
71	FramDZ3	POT	displacement	Z	steel frame
72	FramZD4	POT	displacement	Z	steel frame
73	FramAX1	ACC	acceleration	X	steel frame
74	FramAY1	ACC	acceleration	Y	steel frame
75	FramAX2	ACC	acceleration	X	steel frame
76	FramAY2	ACC	acceleration	Y	steel frame
77	BlckAX1	ACC	acceleration	X	top of rigid mass
78	BlckAY1	ACC	acceleration	Y	top of rigid mass
79	BlckAX2	ACC	acceleration	X	top of rigid mass
80	BlckAY2	ACC	acceleration	Y	top of rigid mass
81	BlckDX1	POT	displacement	X	top of rigid mass
82	BlckDY1	POT	displacement	Y	top of rigid mass
83	BlckDX2	POT	displacement	X	top of rigid mass
84	BlckDY2	POT	displacement	Y	top of rigid mass
85	SturtD1	LinearPot	displacement	Y	strut 1 SE
86	StrutD2	LinearPot	displacement	Y	strut 2 NE-E
87	StrutD3	LinearPot	displacement	X	strut 3 N-NE
88	StrutD4	LinearPot	displacement	X	strut 4 NW
89	PltAc12	ACC	acceleration	X	simulator platform - top
90	PltAc13	ACC	acceleration	Y	simulator platform - top
91	PltAc14	ACC	acceleration	Z	simulator platform - top
92	LC32	load cell	shear	X	bearing 3 NW